Nayan Nagesh Nayak

Master of Technology in Industrial Biotechnology
Erasmus Mundus Master in Membrane Engineering

Design and Functionalization of Alumina Monoliths for Protein Purification by Chromatography

Dissertation to obtain the Doctoral Degree in
Membrane Engineering

Advisor:	Carla Alexandra Moreira Portugal, Senior Researcher, Faculdade de Ciências e Tecnologia da Universidade NOVA de Lisboa, Portugal
Co- advisors:	João Paulo Serejo Goulão Crespo, Full Professor, Faculdade de Ciências e Tecnologia da Universidade NOVA de Lisboa, Portugal
	Martine Masbernat-Meireles, Senior Scientist, Laboratoire de Génie Chimique, Université Paul Sabatier, France
	Lidietta Giorno, Senior Researcher, ITM – CNR, Universita della Calabria, Italy
	Efrem Curcio, Associate Professor, DIATIC, Universita della Calabria, Italy

Examination Committee:

Chairperson:	Dr. Paulo Manuel Assis Loureiro Limão-Vieira, Full Professor, Faculdade de Ciências e Tecnologia da Universidade NOVA de Lisboa, Portugal
Rapporteurs:	Dr. Cristiana Boi, Associate Professor, University of Bologna. Italy
	Dr. Ana Margarida Nunes da Mata Pires de Azevedo, Assistant Professor, Instituto Superior Técnico - Universidade de Lisboa, Portugal
Members:	Dr. Ana Cecília Afonso Roque, Associate Professor, Faculdade de Ciências e Tecnologia da Universidade NOVA de Lisboa, Portugal
	Dr. Andrei Kavaleuski, Principal Researcher, Universidade de Aveiro, Portugal
	Dr. Carla Alexandra Moreira Portugal, Senior Researcher, Faculdade de Ciências e Tecnologia da Universidade NOVA de Lisboa, Portugal

FACULDADE DE CIÊNCIAS E TECNOLOGIA
UNIVERSIDADE NOVA DE LISBOA

July, 2019

Design and functionalizaton of alumina monoliths for protein purification by chromatography

Dedicated to the Earth; this thesis would not have been possible without her....

Acknowledgements

It seems like yesterday that I began my research career with a group of wonderful and resourceful people here at UNL. This chapter of my life has helped me meet new people, gain valuable experience, see things from different perspectives but more importantly has made a major contribution towards my self-development for which I am ever grateful. One must consider oneself very lucky to have had the opportunity to work in such a multi-cultural environment and grow simultaneously in terms of wisdom and knowledge.

I have to begin by thanking the people who are responsible for me being here – my parents and theirs (my grandparents), my brother and sister-in-law - these wonderful people have stood by my side at each step of my life, to show me the right path, guide me at each turn and lift me up when I fell. Although words are never enough to match their love and support, I thank them for everything.

Life is a journey through a series of crests and troughs. Some troughs are easier to cross but others need the right guidance and support to get through. In this matter, the right mentor is crucial – I would not have reached my destination had it not been for the steadfast support from Dr. Carla Portugal and Prof. João Crespo. In the toughest of times they did not give up on me and encouraged me with gentle motivation when I needed it the most. They provided me with very valuable guidance and had the patience to work with me – which is a very difficult thing. Without them, there would have been no light at the end of the tunnel.

I would have no thesis had it not been for my work at Universidade de Aveiro. The guidance of Dr. Andrei Kovalevsky and Dr. Nuno Vitorino from the lab of Prof Jorge Frade at CICECO. This work formed the basis of my thesis. I express my deepest thanks for letting me work in their lab for the short but truly impactful period.

I would like to express my gratitude to Prof. Vitor Alves of Instituto Superior de Agronomia, Lisboa – the work done with him about the rheological parameters was seminal for my thesis. I also sincerely thank Dr. Rosa Huertas for her help and guidance throughout the work we did on functionalization – her ideas and enthusiasm were inspiring.

I owe my gratitude to Dr. Martine Meirieles-Masbernat of UPS Toulouse, FR., for guiding me through the mobility in Toulouse. I am also grateful to Dr. Christophe Tenailleau for all his help with the X-ray tomography in Toulouse. I would also like to thank all the administrative and laboratory staff of UPS for their help during my stay there. Special mention to my colleague from

EM3E and during the doctorate – Lucia Benavente – without whom I would have been lost in France.

I am grateful to Dr. Lidietta Giorno for accepting me into her lab at ITM – CNR, Universita della Calabria, IT. Her whole team – Francesca Militano, Fabio Bazaraelli, Rosalinda Mazzei and Teresa Poerio – were instrumental in all the interesting work that we carried out with monolith-protein interactions. I would like to thank them for all their help. Additionally, I would like to thank especially Dr. Giovanni Chiapetta for all his help to make my stay in Italy as smooth and comfortable as possible.

I am particularly grateful for the assistance given by Prof. Isabel Coelhoso, starting from the day she picked me up from the airport to helping me and my wife find a house, appreciating the samosas we cooked, her valuable guidance and for every other help that she provided.

I would like to offer my special thanks to Dr. Zarco (Svetlozar Velizarov) for sharing with me his wisdom and experience and for his lively spirit at Indian dinners. It was a pleasure working with you.

I would like to express my appreciation to all the wonderful people at IBET – specially Dr. Vanessa Pereira and Dr. Sandra Sanches for their help during my work. If you have met her you know that you cannot thank Dr. Teresa Crespo enough for keeping things lively, be it at work or at Indian dinners. Ofcourse, she has gone out of her way to help me when I needed to complete crucial tasks. On that note, I would like to thank the team at the analytical services in ITQB for all their help with FTIR analysis.

Donna Maria-José Carapinha and Donna Palminha deserve special thanks for all their help – be it with booking meeting rooms, printing things or even with arcane lab equipments – they are always there with a smile and never say no to anything.

Ultimately, the whole point of doing anything in life is to feed oneself and so I would like to express my deepest thanks to Nuno from the cafeteria in the Quimica building for all the pao de leites and meia de leites. Ofcourse, there is not enough words that can be said without salivating about the mensa in Calabria that never failed to provide me with delicious food – it was one of the highlights of my stay there.

Special thanks should be given to Nuno Costa for all the experiments he helped me through the analytical services of Requimte.

I would like to thank all my friends and colleagues from EM3E and EUDIME for making this such a multicultural and special journey. I would like to especially mention Dr. Laks with whom I began this journey in Europe and who has been secretly influencing all my decisions (yella gothu sirra).

One of my best friends Vikas Yelemane – who has been my guide through all things chromatography and a companion in all things philosophical. My friends Mariella Polino (Cleanino) and Paloma Ortiz – never have I seen such an oxymoronic friendship between (wo)man and bird. Special thanks to all my friends – Carla Martins, Ana Rute Ferreira, Magdalena Malankowska, Papa Sergio Santaro (bless us all), Javier Aragon (Ossas), Pritam Das, Ramato Tufa, Rakesh and his wife Neha, Sudheesh to name a few.

A big shout out to Mohammed Tariq, Hurmana Tariq, Syed Usman Taqui (our adopted son), Suchintan Mondal and little Mishaal – you guys have been our family here. The times we have spent together, the amazing dinners we have eaten, the games we have played and the occassions (beach baaki raha!) we have celebrated have made me realize how important these little joys are! I am very grateful to you all for being a big part of my life.

My wife Divya Nayak, my two little munchkin doggies Lua and Jake – whatever would I do without you three! Starting the day with a weird sounding cry from Jake to Lua's begging for free massages to my wife's PJs or question of "When will you finish writing your thesis?", this trio is what gets me through the day. Thank you for being the crazy bunch you are!

I would like to thank Education, Audiovisual and Culture Executive Agency of the European Commission for providing me with the Erasmus Mundus Scholarship to pursue both my masters and doctorate. I would also like to thank Fundação para a Ciência e a Tecnologia for the funding of my project. I would like to sincerely thank all the administration and non-administrative staff of all the universities – Universidade Nova de Lisboa, Universidade de Aveiro, Universite Paul Sabatier Toulouse and Universidad della Calabria (ITM CNR) for all their help and support through out my work and stay.

Thank you!

"I may not have gone where I intended to go, but I think I have ended up where I needed to be"

- Douglas Adams, The Long Dark Tea-Time of the Soul

Abstract

This thesis is about the development of multimodal porous cellular alumina structures (monoliths) by an emulsion-gel casting technique using eco-friendly and inexpensive lipids such as corn oil, castor oil, margarine and their mixtures as the dispersed phase. The monoliths obtained showed good mechanical stability (in terms of compressive strength) despite being porous (up to 60%). The formation of the porous networks was interpreted based on combined droplet coalescence, flocculation and Ostwald ripening effects. The presence of such effects along the emulsion storage time led to changes in their viscoelastic and morphological properties, which were found to correlate with structural descriptors of the monoliths after sintering (e.g. average pore sizes and porosity). Furthermore, the fact that these monoliths had hierarchically distributed pores supposes that there would be paths or channels for fluids to flow through them. Experimental and computational studies were performed to understand the behaviour of fluid flow through the monolith. As per literature, several modelling approaches have been applied to describe experimentally observed flow behaviour in such materials. Morphology plays a key role in determining their hydrodynamic and mass transfer properties. Therefore, a direct computational fluid dynamics (CFD) modelling approach was applied to simulate flow behaviour in these columns. The morphological structure of a fabricated alumina monolith was first reconstructed using 3D X-ray tomography data and, subsequently, OpenFOAM, an open-source CFD tool, was used to simulate the essential parameters for monoliths' performance characterisation and optimisation, i.e. velocity and pressure fields, fluid streamlines, shear stress and residence time distribution (RTD). Moreover, the tortuosity of the monolith was estimated by a novel method, using the computed streamlines, and its value (~1.1) was found to be in the same range of the results obtained by known experimental, analytical and numerical equations. Besides, it was observed that fluid transport was dominated by flow heterogeneities and advection, while the shear stress at pore mouths was significantly higher than in other regions. The proposed modelling approach, with expected high potential for designing target materials, was successfully validated by an experimentally obtained residence time distribution (RTD). However, alumina itself is a relatively non-reactive material. Therefore, to explore a potential application for the produced monolith a simple, single stage sol-gel synthesis method was used to functionalize the monoliths with (3-Aminopropyl)triethoxysilane (APTES) in an aqueous environment. The nature of the attachment of APTES to the alumina and its distribution through the monolith column was evaluated using characterization methods involving FTIR-

ATR, SEM-EDS and XPS measurements. Furthermore, the reaction conditions in terms of catalyst used (acid or base) and temperature were adjusted and, separately, a factorial experimental design was applied to elicit the interdependent influence of humidity, number of APTES coating layers and precursor concentration on the silanization of alumina. The reaction was found to be optimum at basic pH and a temperature of 80˚C. Optimally functionalized monoliths with highest amine density of 166 µmol/g of the column were obtained with a single coat using 2M APTES solution, and at 100% humidity. Finally, experiments were carried out to understand the protein interactions with the produced amine functionalized alumina monolithic columns. Bovine Serum Albumin (BSA) was used as the model protein. Studies were carried out at varied BSA concentrations (0.5 to 10 $mg.mL^{-1}$) to understand the interaction behaviour between the protein and the column. It was found that at lower concentrations there appeared to be stronger binding. At higher BSA concentrations, due to the formation of aggregates, the interaction appears to be a multi-layered physical adsorption. Dynamic light scattering measurements further confirmed the presence of protein aggregation phenomena at higher protein concentrations due to the contact of the protein solution with the column. From these inferences, appropriate strategies were used to bind Protein G to the column - a maximum of 1.43 mg Protein G/g of monolith (29% by mass of column) was bound. Finally, a binding-elution experiment using bovine immunoglobulin G was conducted and it was found that 73.4% (IgG/Protein G) could bind to the column and 86% of the bound IgG could be eluted using an appropriate buffer. This proved the potential of the amine functionalized monolith for further application as an Affinity Chromatography medium.

Keywords: α-alumina monoliths, Emulsion-gel casting, X-ray tomography, Computational fluid dynamics, APTES functionalization, Binding kinetics, Dynamic light scattering, Protein A/G

Resumo

O trabalho descrito nesta tese centra-se no desenvolvimento de estruturas porosas multimodais de alumina (monólitos) através da técnica de *emulsion-gel casting* usando como fase dispersa lípidos baratos e ambientalmente sustentáveis, tais como o óleo de milho, óleo de rícino, margarina e suas misturas. Apesar de porosos (com porosidades até 60%) os monólitos obtidos demonstraram possuir boa estabilidade mecânica (no que respeita à força de compressão). A formação e as caracteríticas morfológicas destas estruturas porosas foram interpretadas com base no efeito combinado da coalescência de gota, floculação e maturação Ostwald (*Ostwald rippening*). Observou-se que a presença destes efeitos durante o período de armazenamento da emulsão conduziu a alterações nas suas propriedades viscoelásticas e morfológias, as quais mostraram possuir correlação com descriptores estruturais dos monólitos sinterizados (isto é, tamanho de poro médio e porosidade). Para além disto, a presença de uma distribuição hierárquica de poros, faz prever a existência de canais e espaçamentos nos monólitos disponíveis para o escoamento de fluídos. Foram realizados estudos experimentais e de modulação computacional de modo a compreender o comportamento dos fluído através destes monólitos. O escoamento de fluídos observado experimentalmente foi descrito por diferentes abordagens.

A estrutura morfológica dos monólitos desempenha uma papel crucial na determinação das propriedades hidrodinâmicas e de transferência de massa. Por esta razão, foram usadas técnicas de modulação computacional de dinâmica de fluídos, C*omputational Fluid Dynamics (CFD*) para simular o escoamento de fluídos através das estruturas porosas. Primeiramente, foi usada a técnica de tomografia de raios-x tridimensional (3D x-ray tomography) para reconstruir a estrutura morfológica do monólito de alumina. Seguidamente, as imagens obtidas foram usadas para simular pârametros essenciais para a caracterização e optimização do desempenho dos monólitos, nomeadamente a velocidade, os campos de pressão, as linhas de fluxo, a tensão de corte e a distribuição de tempos de residência (Residence Time Distribution, RTD) utilizando a ferramenta para modulação CFD, OpenFOAM disponível para utilização livre. As linhas de fluxo obtidas por simulação computacional permitiram estimar a tortuosidade dos monólitos utilizando métodos inovadores, resultando em valores de tortuosidade, de ~1.1, dentro do intervalo de valores determinados através de equações numéricas, analíticas e empíricas bem conhecidas. Além disso, observou-se que o transporte de fluídos é dominado por heterogeneidades de fluxo e advecção, enquanto que a tensão de corte à entrada dos poros é significativamente maior do que

em outras regiões da estrutura porosa. Os valores da distribuição de tempos de residência modulados foram comparados com os obtidos experimentalmente. A proximidade entre ambos permitiu validar a abordagem de modulação utilizada e mostrou o seu potêncial para o desenho deste tipo de materiais porosos.

A alumina é um material pouco reativo. Por esta razão, e de modo usar estas estruturas porosas em processos de separação baseados na afinidade química, os monólitos foram funcionalizados com (3-aminopropil) trietoxisilano (APTES) em fase aquosa, por métodos simples de síntese sol-gel de passo único. A natureza da ligação do APTES à alumina e sua distribuição através da coluna de monólito foi avaliada usando técnicas de caracterização, tais como FTIR-ATR, SEM-EDS e XPS. Além disso, as condições de reação em termos do catalizador usado (ácido ou base) e temperatura foram ajustadas e a influência interdependente da humidade, número de camadas de APTES e concentração do percursor na silinização da alumina foram estudadas aplicando a metodologia de desenho factorial de experiências. A reação foi considerada ótima em pH básico e à temperatura de 80˚C. Monólitos com maior densidade de amina, 166 µmol/g coluna, foram obtidos após revestimento com uma única camada de APTES, usando uma solução de 2M de APTES e humidade de 100%. Por fim, foram realizadas experiências para testar a interação de diferentes proteínas modelo: BSA, Proteína G e Proteína A, com o monólito funcionalizado com o objectivo de inferir acerca da adequabilidade da utilização destes para processos de purificação de imunoglobulina (IgG) baseada em afinidade química.

Palavras-chave: Monólitos de alumina alfa, fundição em emulsão-gel, tomografia de raios X, dinâmica de fluidos computacional, funcionalização de APTES, cinética de ligação, espalhamento de luz dinâmico, proteína A/G

Resumé

Cette thèse porte sur le développement des structures multimodales d'alumine cellulaire poreuse (monolithes) par une technique de coulée en gel d'émulsion utilisant des lipides écologiques et peu coûteux, tels que l'huile de maïs, l'huile de ricin, la margarine et leurs mélanges en phase dispersée. Les monolithes obtenus ont montré une bonne stabilité mécanique (en termes de résistance à la compression) malgré leur porosité (jusqu'à 60%). La formation des réseaux poreux a été interprétée sur la base des effets combinés de la coalescence des gouttelettes, de la floculation et de la maturation d'Ostwald.

La présence de tels effets tout au long de la durée de stockage de l'émulsion a entraîné des modifications de leurs propriétés viscoélastiques et morphologiques, qui se sont révélés être en corrélation avec les descripteurs structurels des monolithes après frittage (par exemple, la taille moyenne des pores et la porosité).

De plus, le fait que ces monolithes aient des pores répartis hiérarchiquement suppose qu'il y aurait des chemins ou des canaux permettant aux fluides de les traverser. Des études expérimentales et computationnelles ont été réalisées pour comprendre le comportement de l'écoulement de fluide à travers le monolithe. Conformément à la littérature, plusieurs approches de modélisation ont été appliquées pour décrire le comportement d'écoulement observé de manière expérimentale dans de tels matériaux.

La morphologie joue un rôle clé dans la détermination de leurs propriétés hydrodynamiques et de transfert de masse. Par conséquence une approche de modélisation CFD (« Computational Fluid Dynamics ») directe a été appliquée pour simuler le comportement de l'écoulement dans ces colonnes.

La structure morphologique d'un monolithe d'alumine fabriqué a d'abord été reconstruite à l'aide de données de tomographie 3D à rayons X. OpenFOAM, un outil open source CFD, a ensuite été utilisé pour simuler les paramètres essentiels de la caractérisation et de l'optimisation des performances du monolithe, à savoir : vélocité et champs de pression, lignes de courant de fluides, contrainte de cisaillement et distribution des temps de séjour (« Residence Time Distribution » - RTD).

De plus, la tortuosité du monolithe a été estimée par une nouvelle méthode - en utilisant les lignes de courant calculées, et sa valeur (~ 1,1) - qui se situe dans la même gamme de résultats que celle obtenue par des équations expérimentales, analytiques et numériques connues. En outre, il a été observé que le transport des fluides était dominé par les hétérogénéités d'écoulement et l'advection, tandis que la contrainte de cisaillement au niveau des bouches des pores était significativement plus élevée que dans d'autres régions.

L'approche de modélisation proposée, avec un potentiel élevé attendu pour la conception de matériaux cibles, a été validée avec succès par une distribution de temps de séjour (RTD) obtenue de manière expérimentale. Cependant, l'alumine elle-même est un matériau relativement non réactif.

Par conséquent, afin d'explorer une application potentielle pour le monolithe produit, une simple méthode de synthèse sol-gel en une étape a été utilisée pour fonctionnaliser les monolithes avec du (3-aminopropyl) triéthoxysilane (APTES) dans un environnement aqueux.

La nature de la fixation des APTES sur l'alumine et de sa distribution dans la colonne de monolithes a été évaluée à l'aide de méthodes de caractérisation faisant appel à des mesures FTIR-ATR, SEM-EDS et XPS.

En outre, les conditions de réaction en termes de catalyseur utilisé (acide ou base) et de température ont été ajustées et, séparément, un plan d'expérience factoriel a été appliqué pour déterminer l'influence interdépendante de l'humidité, du nombre de couches de revêtement APTES et de la concentration de précurseurs sur la silanisation de l'alumine.

La réaction s'est révélée optimale à pH basique et à une température de 80 ° C. Des monolithes fonctionnalisés de manière optimale, avec une densité d'aminé la plus élevée de la colonne -166 µmol / g- ont été obtenus avec une seule couche constituée d'une solution APTES 2M, à 100% d'humidité.

Enfin, des expériences ont été menées pour tester l'interaction entre le monolithe d'alumine fonctionnalisé et différentes protéines modèles: BSA, Protéine G et Protéine A, visant à inférer l'aptitude à utiliser ces monolithes pour la purification d'immunoglobuline (IgG) par affinité.

Mots-clés: monolithes d'alpha-alumine, coulée en émulsion-gel, tomographie à rayons X, dynamique numérique des fluides, fonctionnalisation APTES, cinétique de liaison, diffusion dynamique de la lumière, protéine A / G

Sommario

Questa tesi tratta dello sviluppo di strutture porose multimodali di allumina (monoliti) tramite la tecnica di *emulsion-gel casting* e l'utilizzo, come fase dispersa, di lipidi economici ed *eco-friendly* quali l'olio di mais, l'olio di ricino, la margarina e miscele di questi. I monoliti ottenuti hanno mostrato buona stabilità meccanica (in termini di resistenza a compressione) nonostante la porosità (fino al 60%).

La formazione dei pori è stata giustificata dalla concomitanza degli effetti di coalescenza delle gocce, flocculazione e maturazione di Ostwald. La presenza di questi effetti durante il tempo di residenza dell'emulsione ha condotto a variazioni nella viscoelasticità e nelle proprietà morfologiche, che sono state correlate con le caratteristiche strutturali dei monoliti (porosità e dimensione media dei pori) dopo il processo di *sintering.* Inoltre, il fatto che questi monoliti contengano pori distribuiti gerarchicamente fa supporre la presenza di canali per il passaggio di fluidi al loro interno. Studi sperimentali e computazionali sono stati condotti per capire il comportamento dei flusso di fluidi all'interno del monolita. Facendo capo alla letteratura, diversi approcci di modellazione sono stati applicati per descrivere il comportamento sperimentale del flusso in questi materiali. La morfologia gioca un ruolo chiave nel determinare le proprietà idrodinamiche e il trasferimento della massa. Quindi, un approccio di fluidodinamica computazionale diretto (CFD) è stato applicato per simulare il comportamento del flusso nelle colonne di allumina. Inizialmente, la struttura morfologica dei monoliti è stata ricostruita usando i dati provenienti dalla tomografia 3D a raggi X. Successivamente, OpenFOAM, uno strumento CFD *open-source,* è stato usato per simulare i parametri essenziali per la caratterizzazione e l'ottimizzazione della *performance* dei monoliti, quali la velocità vettoriale e la pressione e il percorso del flusso atraverso la colonna, lo sforzo di taglio e la distribuzione del tempo di residenza (RTD).

In aggiunta, la tortuosità del monolita è stata estimata con un nuovo metodo, usando computed streamlines, e il valore trovato (~1.1) rientra nel range dei risultati ottenuti dalle equazioni analitiche, sperimentali e numeriche conosciute.

Oltretutto, è stato osservato che il trasporto di fluidi è stato dominato dalla eterogeneità del flusso e dall'advezione, mentre lo sforzo di taglio alle bocche del poro risulta significativamente più alto rispetto ad

altre zone. L'approccio di modellazione proposto, con elevate aspettative nel progettare materiali *target*, è stato validato con successo dal valore di distribuzione di tempi di residenza (RTD) ottenuto sperimentalmente. Tuttavia, l'allumina di per se è un materiale relativamente non-reattivo. Quindi, per esplorare una potenziale applicazione per il monolita prodotto, un semplice singolo step del metodo di *sol-gel synthesis* è stato usato per funzionalizzare i monoliti con (3-aminopropil)trietossisilano (APTES) in un ambiente acquoso. La natura dei legame di APTES con l'allumina e la sua distribuzione nella colonna di monolita è stata caratterizzata usando le seguenti tecniche: FTIR-ATR, SEM-EDS e XPS. Inoltre, le condizioni di reazione in termini di catalizzatore usato (acido o base) e temperatura sono state adeguate e, separatamente, la progettazione di un esperimento fattoriale è stato applicato per capire l'influenza interdipendente dell'umidità, del numero di strati di copertura di APTES e la concentrazione del precursore sul processo di silanizzazione dell'allumina.

La reazione è ottimale a pH basico e alla temperature di 80°C. Monoliti ottimali funzionalizzati con la più alta densità di ammine (166 µmol/grammi di colonna) sono state ottenute con una singola copertura con una soluzione di APTES 2M e al 100% di umidità. Alla fine, è stata testata l'interazione tra i monoliti di allumina funzionalizzati con diverse protein modello: BSA, Protein G and Protein A con l'obiettivo di verificare l'idoneità di questi monoliti per la purificazione per affinità di immunoglobuline (IgG).

Parole chiave: monoliti di allumina alfa, fusione di emulsione-gel, tomografia a raggi X, fluidodinamica computazionale, funzionalizzazione APTES, cinetica di legame, diffusione dinamica della luce, Proteina A/G

Contents

List of Figures

List of Tables

List of acronyms

Abbreviations

AC Atomic concentration

AM Additive manufacturing

AMC Affinity monolith chromatography

APTES (3-aminopropyl)triethoxysilane

ATF Alternating tangential flow filtration

BCA Bicinchoninic acid assay

BSA Bovine serum albumin

CEC Capillary electrochromatography

CFD Computational fluid dynamics

DLS Dynamic light scattering

EDMA Ethylene dimethacrylate

EDX Energy dispersive X-ray spectrum

FTIR Fourier-transform infrared spectroscopy

GAMG Geometric-algebraic multi-grid

GMA Glycidyl methacrylate

HPLC High-performance liquid chromatography

IgG Immunoglobulin G

MCSGP Multicolumn countercurrent solvent gradient purification

MOF Metal-organic frameworks

NMR Nuclear magnetic resonance spectroscopy

PBiCG Preconditioned biconjugate gradient

PBS Phosphate buffered saline

PCC Periodic counter current chromatography

PDI Polydispersity index.

pI Isoelectric point

PSD Pore size distribution

RTD Residence time distribution

SDS Sodium dodecyl sulphate

SEM Scanning electron microscopy

SIMPLE Semi-implicit method for pressure-linked equations

SMBC Simulated moving bed chromatography

TEOS Triethylmethoxysilane

XPS X-ray photoelectron spectroscopy

Variables

b_T, k_T Tempkin constants

C_e equilibrium concentration of solute ($mg.ml^{-1}$)

C_t tracer concentration ($mol.m^{-3}$)

D_p pore diameter (µm)

$d_{3,2}$ Sauter mean droplet diameter (µm)

E(t) residence time distribution (s^{-1})

E(Θ) dimensionless residence time distribution (-)

G' storage modulus (Pa)

G" loss modulus (Pa)

G_N^0 plateau modulus (Pa)

K_a Langmuir constant

K_F, n_F Freundlich constants

k_1, k_2 rate constants

L streamline length (m)

N dimensionless constant related to the power law index (-)

n_F heterogeneity factor (-)

P pressure (Pa)

Q_m maximum adsorption capacity ($mg.g^{-1}$ of monolith)

q_t absorption capacity at given time 't'

R universal gas constant ($J.K^{-1}.mol^{-1}$)

R_L separation factor (-)

T absolute solution temperature (K)

t time (s)

$\bar{t}$ mean residence time (s)

U velocity vector ($m.s^{-1}$)

u linear flow velocity ($m.s^{-1}$)

Greek symbols

η_a apparent viscosity (Pa.s)

η_0 zero shear rate viscosity (Pa.s)

λ relaxation time constant (s)

φ volume fraction of the dispersed phase (-)

σ interfacial tension ($J.m^{-2}$)

δ loss angle (-)

$\dot{\gamma}$ shear rate (s^{-1})

ε porosity (-)

Θ dimensionless time (-)

μ dynamic viscosity ($m^2.s^{-1}$)

ν kinematic viscosity ($m^2.s^{-1}$)

ρ density ($kg.m^{-3}$)

τ tortuosity (-)

$\boldsymbol{\chi^2}$ chi-square parameter

$\mathbf{R^2}$ correlation coefficient

CHAPTER 1

Introduction

Design and Functionalization of Alumina Monoliths for Protein Purification by Chromatography

1.1. State-of-the-art

1.1.1. Biopharmaceutical industry through the years

Biotechnology is the discipline that deals with the application of scientific and engineering principles to process the materials by biological agents/matrixes for providing goods and services [1]. The end products of biotechnology broadly range from enzymes used in dairy, food and detergents to biopharmaceutical compounds. Previously, biotechnology research was mostly focused for economic gains in food and enzyme industries. However, the gamechanger event took place in 1980 when the U.S. Food and Drug Administration (FDA) approved the first-ever therapeutic recombinant molecule human insulin (HUMULIN-R) which was produced by using recombinant DNA technology [2]. This historic innovation by Lilly & Co., witnessed a shift in paradigm for the remarkable development of a challenging, yet flourishing field of biopharmaceuticals.

The biopharmaceutical industrial sector is entangled in the product development, scale-up and marketing of medical drugs that are produced by using the nuances of biotechnology. These products include proteins (immunoglobulins, fusion proteins, soluble receptors, cytokines, and other polypeptide products for their application in diagnostics and therapeutics), nucleic acids (RNA, DNA or antisense oligonucleotides), and bacteria and viruses (where the process of attenuation results in the reduction of virulence). These biopharmaceutical products are subsequently utilized for *in vivo* diagnostic or therapeutic purpose and their production uses routes other than direct extraction from native (non-engineered) biological sources [3].

Biopharmaceuticals are one of the exemplary accomplishments of modern science. An unprecedented development in biologics has been witnessed ever since the completion of the human genome sequencing, that has found its applications in the field of diagnostics and therapeutics. These therapeutic matrixes/biomolecules are complex in structure and offer precision in their mechanism of action along with reduced side effects. Moreover, biologics is one of the rapidly growing segments of the biopharmaceutical industry, having over 200 products that range from simple biomolecules such as peptides to complex virus-like bioparticles. This accounts up to 79% of total pharmaceutical sales in quite a few top-tier product portfolios of multinational pharmaceutical companies [4]. There has been an annual 15% linear increase in the launch of novel biological entities owing to the exponential triumph of biologics innovations in clinical stages. Several astounding biologics patents are seen to have started expiring from 2015. Thus, there is

a flood of approvals being sought for bio-similar by regulatory agencies. Biosimilars enable multiple players to carry-out careful strategies of conducting research, manufacture, and to market a successful product. This ensures the reduction of product cost coupled with increase of the overall revenue in this biopharmaceutical sector. As of 2010, a study conducted by IMS health reports that biopharmaceuticals have recorded a market value of USD 138 billion [5] and are expected to flourish in the business to reach a value over USD 320 billion by 2020 [6].

1.1.2. Downstream processing

Bioprocessing is the technology that encompasses biologics production, separation, and purification. This discipline comprises upstream and downstream bioprocesses. The former bioprocesses of upstream includes the manufacturing of a target product on a large scale, while the latter bioprocesses of downstream focusses on the separation and polishing of the desired targeted product. Recently, the upstream bioprocesses have attained efficiency in producing very high quantities of therapeutic molecules, which was deemed as an impossible feat just a few decades ago. With the continued increase of culture yields, the production bottleneck for achieving high-value end-products has been shifted towards downstream processing. From the economic perspective, downstream processing accounts to about 80% of the total manufacturing costs [7]. The upsurge to trigger the continuous development of new and efficient (bio) separation processes is witnessed due to the ever-increasing global competition faced in the biotech markets, and the additional pressure from the regulatory agencies to maintain the low costs of sales [8].

Bio-manufacturing and processing face several difficult challenges while comparing to their chemical counterparts. In bio-production, process efficiency is affected by a large number of multi-variable factors. While dealing with downstream processing, it is evidently possible to have the fermentation broth containing a complex mixture of product, by-products, suspended cells, and debris, along with many additional and undefined contaminants. Product inconsistency resulted in stringent laws enforced by the regulatory agencies for defining the specific purity requirements of the therapeutic products. The purity requirements of such biotechnological products vary, depending on their targeted applications. For example, therapeutic proteins are known to have a demand for 99.99% purity or sometimes even higher.

Purity requirements also play a pivotal role in determining the number of unit operations that are essential for the overall process. For instance, depending on the nature of the product, most

commonly used therapeutic protein purification schemes are subjected to have from seven to fourteen purification steps. Capital investment for purchasing the designated equipment, the cost of consumables and labor, increases the economic costs with the increase of purification steps. From a process engineering perspective, every unit operation possesses an inevitable economical loss in product recovery. In such acute financial calculations, more steps are incorporated while having more cost per gram of product. Lilly and Fish governed the cost of recombinant proteins in 1984: interestingly, only 14% of the cost was attributed to the fermentation process while downstream processing governed the rest of the cost [9]. In the existing state of technology, 50-80% of the total production cost is attributed to downstream processing [10], which emphasizes the fact that there is a dire need for downstream process optimization to make the manufacturing process economically viable [11].

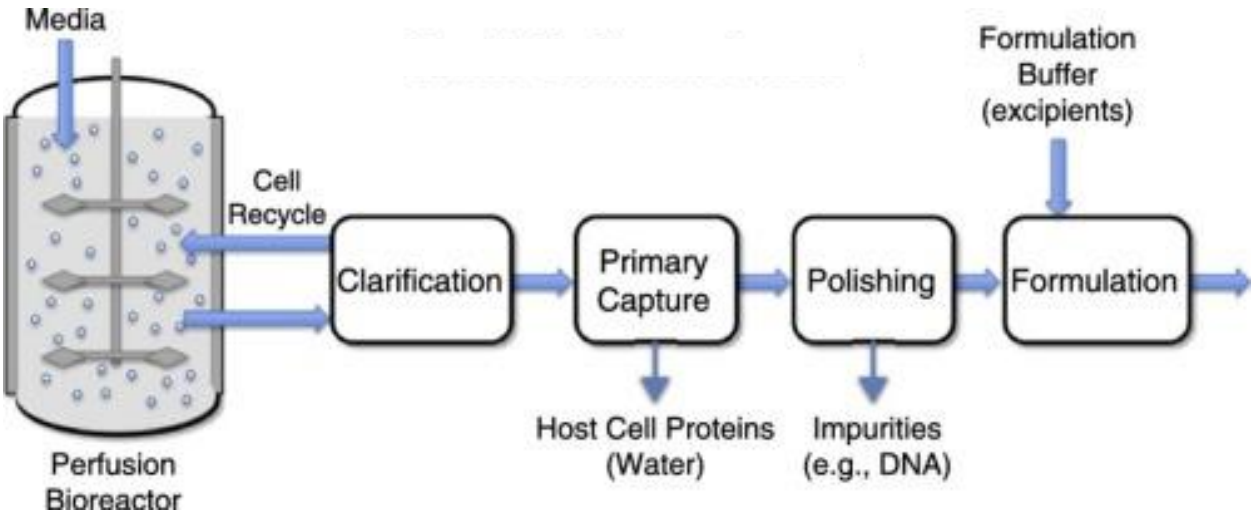

Figure 1.1. Schematic representation of a generic continuous downstream (adapted from [12])

Downstream processing is broadly classified into three stages, namely: initial capture stage, intermediate capture and separation stage, and lastly, the final polishing stage (Figure 1.1). The primary focus of the capture stage is isolating, capturing and stabilizing the target molecule. Proteins and nucleic acids, viruses and endotoxins etc., that generally constitute the bulk impurities are eliminated in the intermediate step. In the final polishing stage, trace amounts of the contaminants and the product-related impurities, which are the remnants of the intermediate steps, are removed. Thus, highest levels of protein purity are achieved in this process.

From the process engineering perspective, industries prefer to achieve the set target purity and bioactivity with the least possible number of unit operations. With the increase in number of unit operations, there is a decrease in product recovery and functionality because no process is a 100% efficient – even with a loss of 5% per stage within 6 steps the overall process efficiency becomes 73%. A general overview highlighting the various steps including the series of unit operations involved in the three stages of downstream processing, is depicted in Figure 1.2 [13]. Furthermore, an optimal balance between the number of unit operations, yield to be obtained, time required, and preservation of activity must be balanced with economy to make any downstream process effective.

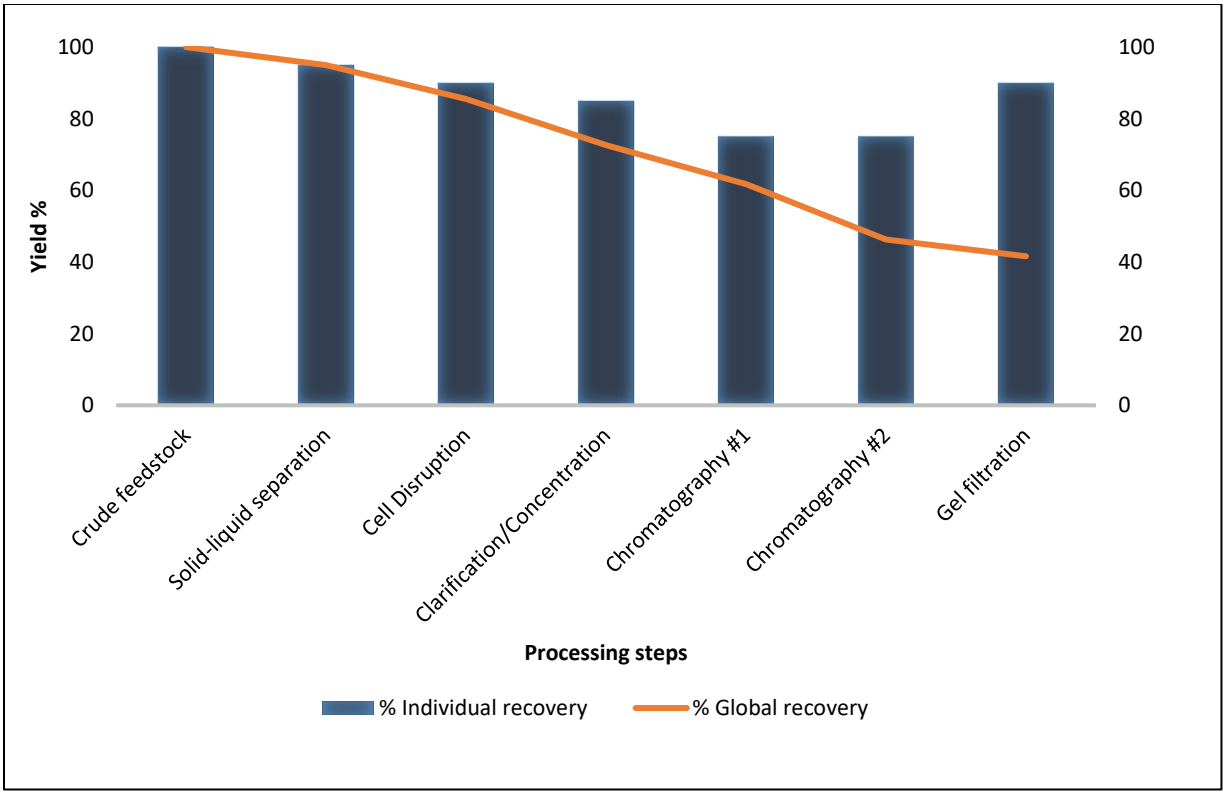

Figure 1.2. Series of downstream processing steps and their yields (adapted from [13])

Considering these challenges, a different and recent approach towards more efficient downstream processing is to move from the present paradigm of batch processing to a more continuous manufacturing – especially in the fine refining stages (polishing) where batch chromatographic processes are commonly applied. In this context, several new processes like Periodic Counter Current Chromatography (PCC), Multicolumn Countercurrent Solvent Gradient

Purification (MCSGP) and the well-known but complex Simulated Moving Bed Chromatography (SMBC) are leading the way to more effective processing [14]. Briefly, all these three processes involve the use of multiple columns in sequence that are switched in position to obtain countercurrent contacting between the product of interest and the separating medium. Although, not a continuous process in the traditional sense, this column switching simulates a continuous process leading to improved production times, lower footprint and wastage, and higher efficiencies. On a related note, Warikoo et al., [15] recently presented results for the capture and initial purification of a monoclonal antibody and a recombinant human enzyme produced using a perfusion bioreactor operated with an alternating tangential flow filtration (ATF) system and directly integrated with a PCC system. The integrated processes ran continuously for 30 days with comparable product quality to traditional batch processes but with much smaller equipment footprint and greater productivity.

1.1.3. General chromatography

Chromatography is widely represented as a technique that incorporates both analytical and preparative tools to separate and identify the desired target molecule from the product mixture, which is either crude or clarified. The underlying principle of chromatography revolves around the target molecule's surface properties that may exhibit various types of interactions by which it can adsorb on an adsorbent surface. Chromatography has been increasingly realized as a major bankable tool for facilitating industrial-scale separations, which are mostly concentrated either at the intermediate or at the polishing stage.

There are two phases in all the chromatographic processes, namely, the static or stationary phase, and a mobile or moving phase. Commonly witnessed separation principles are hydrophobic interaction (hydrophobic and reversed phase), size and shape (gel filtration or size exclusion), biological recognition (affinity), metal chelate and net charge (ion exchange). A summary highlighting the various chromatography principles is presented in Table 1. 1 [16].

Table 1.1. Basic chromatography principles (adapted from [16])

Separation principle	Type of chromatography	Acronym	Nature of mobile phase
Size and shape	Gel filtration or size exclusion	SEC	Aqueous solution with controlled ionic strength and/or pH
Net charge	Ion exchange	IEX	Low salt aqueous solution, elution using increasing salt concentration
Hydrophobic interaction	Hydrophobic interaction	HIC	High salt aqueous solution, elution using decreasing salt concentration
	Reversed phase	RPC	Water-organic solvent mixture, elution with increasing solvent concentration
Biological recognition	Affinity	Affinity	Change in pH, ionic strength, competitive elution
Metal chelate	Metal interaction	MIC	Low salt aqueous solution, elution using competitive desorption

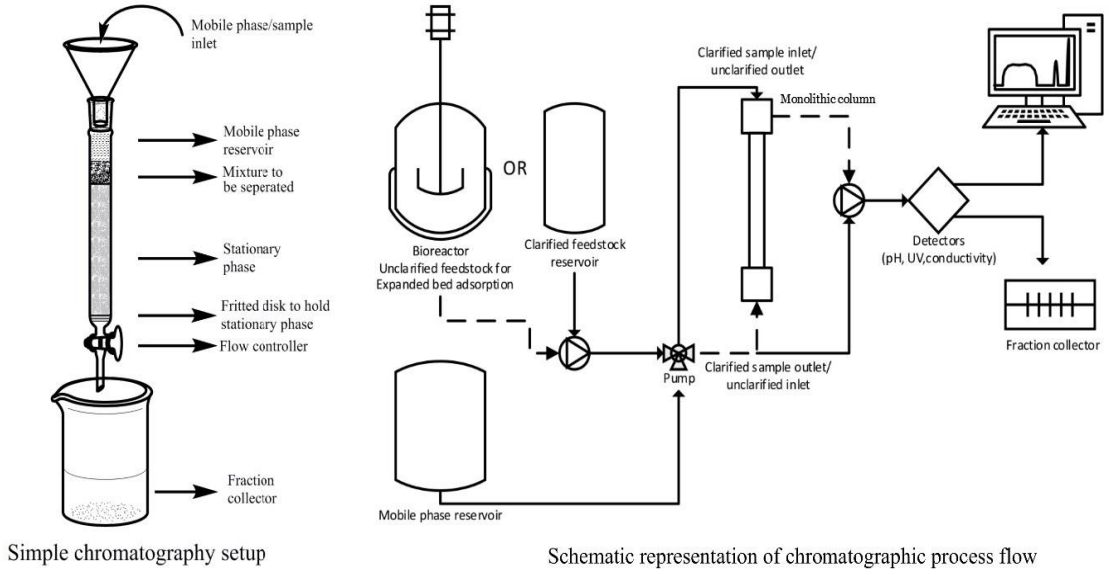

Figure 1.3. Schematic representation of the process flow (adapted from [8])

For designing a purification process with higher efficiency, two things are routinely considered: the order in which the desired separation techniques are arranged and the optimized process conditions for the individual separation techniques. In this way, the required purity is achieved and in every advancing step, the reduction of process volume is achieved. In chromatography, many different interacting principles govern the separation of biomolecules. Thus, the type of

chromatographic technique to be used is decided based on the nature of the desired target molecule and the type of contaminants present.

Figure 1.3 depicts a simple chromatography setup that consists in a packed column incorporating a fraction collector, a stationary phase and a mobile phase. This classical setup is widely used by biochemists on the lab scale, which is mostly employed for small-scale purification. In these scenarios, porosity of the column and the gravitational force drives the mobile phase flow.

Porous materials with controlled parameters, i.e., pore shape, pore size distribution and porosity opens a window of opportunities for myriad applications in electronics [1,2], energy storage [17–21], catalysis [22–24], sensing [25], adsorbent [26–28], biomedical science [29–32], and separation science [33–37] mainly owing to its low density and highly accessible surface area. Many different varieties of porous materials are synthesized from organic substrates (like polymer) [38–40], inorganic substances (like metals and their oxides) [41,42], along with organic–inorganic hybrids (like metal-organic frameworks (MOFs) and polysilsesquioxane) [43–45]. Characteristically, porous media are made up majorly of voids, which can be either of random character (disordered pore systems) or with high regularity (ordered pore systems). The standardized method of classification of porous media is on the basis of the pore diameter (Dp) [46]. Pores diameters, D_p < 2 nm are called micropores, those in the range 2 nm ~ 50 nm are called mesopores and those exceeding 50 nm are called macropores. Based on this definition of pore diameter, porous materials can be classified into microporous materials [47–54], mesoporous materials [41,44,45,53–57], macroporous materials [39,42,43,58–61], and materials that are hierarchically porous (for instance micro-mesoporous [62,63], meso-macroporous [40,64–66], and micro-meso-macroporous materials [67,68]). Zeolites [49,69] are an important ordered microporous material possessing molecular dimensions that are typically sized 0.25 * 1 nm and also enabling for shape-selective catalytic transformations. On the other hand, mesoporous silica is a typical mesoporous material introduced in 1990 by Kuroda et al. [54], where supramolecular templating of micelles was carried out with various surfactants to achieve a highly ordered structure. In recent years, mesoporous materials, based on carbon [55], other metal oxides like alumina and titania [56], and organosilicates [57], have been extensively studied. Traditionally, macroporous materials are synthesized by soft templating using an emulsification technique [58] and by hard templating using latex spheres [59]. Hierarchical structures are critical from the perspective of applications.

Owing to their intrinsic multimodal porous nature with pores in the micro, meso to macro ranges, hierarchically porous materials have been extensively used as catalysts and catalyst supports [70–76]. The presence of micro–mesoporosity in a macroporous solid structure potentially provides size and shape selectivity for reactants, intermediates and/or products. Usually such structures are designed such that the catalytic active sites are located in microporous regions while the macroporous networks minimize diffusion barriers and thus enhance mass transport. Pore modality can also provide for easier separation of products, reactants and intermediates owing to possibility of shape selectivity in such materials. Additionally, it is possible to design structured reactors enabling multiple step reactions. Hierarchically porous solids have largely been used as catalyst supports because they are characterized by large surface areas needed for dispersion/distribution of active components (metals, metal oxides, enzymes or other species) [70–79]. Furthermore, in the case of adsorption processes, hierarchical porosity is a desirable feature because of the high contact surface area, high storage volume, low mass transfer resistances, potential shape selectivity and well controlled porosities over different length scales leading to very high adsorption capacities and separation efficiency. Currently, hierarchically porous materials based on silica, organosilica, metal oxides are commonly used in adsorption [80–83] and separation processes [84–86].

The major manufacturing cost in biological processes is usually represented by the downstream processing of complex and large molecules. Thus, it represents the fundamental step from industrial perspective. Taking protein production as an example, their economical and viable production depends not only from innovative strategies especially in reaction steps but also exploring newer and viable methods for their downstream processing. Chromatographic processes constitute one of the majorly incorporated high-performance downstream processes for either separation or purification purposes. Among the various chromatographic processes for separations, affinity chromatography is a standout in terms of a powerful technique to purify enzymes and various other biochemical materials [67,68,87].

In conventional affinity chromatography, bead packed beds are traditionally used as supports. However, off late membranes and monoliths have been increasingly used as stationary phases for chromatography. Their fast mass transfer is mainly based on convection, which leads to reduced diffusion, which is usually observed in resins [88,89]. For instance, in comparison to conventional random packed beds, monoliths offer reduced pressure drop and mass transfer resistance. Both properties are considered vital for evaluating the chromatography performance,

speed of the process and its scale-up [90–92]. In packed bed chromatography, pressure drop, and mass transfer rates may be the limiting factors. However, monolithic channels witness higher mass transfer rates due to convective transport in their larger pores, while surface interactions on monoliths usually determine the overall reaction rate [93,94]. Nevertheless, both monoliths and membranes suffer from poor flow distribution, which causes inefficient binding, and remains a major challenge for the development of both membrane and monolith devices. Moreover, the comparison of membranes and monoliths for biomolecule separation has been very poorly investigated.

Membrane chromatography was conceived as integration of two unique processes, membrane filtration and liquid chromatography, fusing them into a single-step operation [95–97]. The main advantage of the method are the reduced diffusion times - as molecules and active sites interact in the membrane through - pores, while fluid flows by convection rather than in stagnant fluid inside the resin pores. Thus, it has the potential to operate at high flow rates and low pressure drops, to purify large biomolecules. Lower residence times and pressures tend to reduce the degradation and denaturation of biomolecules, as well as decrease buffer wastage [95–97]. Furthermore, these devices can be made for "single-use", eliminating the need for cleaning and regeneration of the medium, while at the same time reducing the risk of contamination. There are reports of diverse materials being tested as chromatographic supports: inorganic-organic (e.g., an alkoxysilane coated on glass fiber and alumina membranes [98]) and organic materials (i.e., cellulose and its derivatives, nylon, polyethersulfone, polypropylene, polyvinylidene, etc. [98,99]) However, most membrane chromatography devices, are fabricated from regenerated cellulose [98].

There are several reports of devices with axial, radial and tangential flow that have been developed. Axial flow devices containing stacked membrane disks are commonly used at the laboratory scale and are commercialized for different membrane volumes. Due to ease of scale-up, Radial flow membrane chromatography, first reported in the late 1980s [100], and is preferred for large-scale applications. Several varieties of radial flow membrane chromatography devices have been commercialized with large bed volumes up to 1–5 L. Tangential flow devices are known for low - membrane fouling [101] and could be an alternative for industrial applications. Madadkar et al. [102], recently presented a novel configuration using stacked membrane sheets with a lateral feed, to obtain a more uniform flow distribution and, therefore, higher resolution of the elution peaks. However, most studies have concluded that despite the better binding

characteristics observed in membrane chromatography the overall performance was lower because of non-ideal flow distribution in the membrane device - mainly due to crossflows between membrane layers and voids within the membrane housing. Additionally, slow binding kinetics near saturation were observed for the membrane systems which is speculated to be due to the steric interaction between bound ligands and available binding sites which reduced their (binding sites') accessibility.

1.1.4. Monoliths in chromatography

Monolithic supports are made up of porous materials comprising a single adjoining unit. During 1990s, Hjerten et al. [103], Svec and Frechet [104], and Tanaka et al. [105] are credited to develop such materials. Numerous kinds of inorganic (e.g., zirconia, silica [106], carbon [107], and titania [108]) and organic (e.g., poly(styrene–divinylbenzene), polymethacrylate and polyacrylamide [109]) monoliths can be synthesized, but the only commercially available ones are poly(styrene–divinylbenzene), polymethacrylate, and silica-based monolithic columns. The organic monoliths have garnered interest in conventional HPLC which are beneficial for separating macromolecules, like antibodies or proteins [110,111], or when using capillary electrochromatography (CEC) for a broader range of separations [112].

Since 2000, Merck and Phenomenex have marketed silica-based monolithic supports under the trademarks Chromolith and Onyx, respectively. These are most notably used in HPLC. Silica-based monoliths display a bimodal structure and are often characterized by average 2-µm macropores and 13-nm mesopores and tend to have efficiencies comparable to that of porous silica particles (3– 3.5 µm) [113]. Tallarek et al. showed enhanced permeabilities of monolithic silica columns, which were similar to that of a column packed with 11-µm particles [114]. Moreover, the size of meso and macropores can be monitored individually by incorporating a sol-gel synthesis process for tuning chromatographic efficiency and permeability. Silica monoliths at a commercial level, which could be termed as second-generation monoliths, could tap this feature for its benefit [115].

The lower exhibition of backpressure, and sufficient rate of mass transfer makes it viable to operate at higher flow rates (3 to 10 times larger) while using a conventional column length, thereby exhibiting ultra-fast separations, which could be as less as few seconds for separation of various metabolites and substrates [116]. On the other hand, higher resolutions can be achieved in lesser and practical analysis time by incorporating longer monoliths, operating at a satisfactory

flow rate. For instance, a 11.4-meter column was constructed by Tanaka et al. that coupled several monolith columns [117]. For an analysis time spanning over 16 hours, 1 000 000 theoretical plates were achieved in this type of arrangement. However, even though monoliths offer remarkable properties, there are not commonly utilized, and reports suggest that silica-based monolithic columns are routinely used by less than 1% of chromatographers [118]. Possible reasons for this limited use comprises the column geometry and chemistry (internal diameters of the columns are seen with either 2, 3, and 4.6-mm but the limiting factor is the maximum length which is only around 100 mm), reduced number of suppliers due to patent exclusivity, restricted resistance offered by the supports with regard to pH and, even prominently, backpressure (longer columns (>10 cm could have ΔP_{max}~200 bar) [118].

1.1.5. Protein purification using affinity monolithic chromatography

Although most past reports with affinity chromatography have made use of particle-based supports, there has been increasing interest in carrying out affinity-based separations with monolithic supports. Purification of monoclonal antibodies is a very typical case where monolithic chromatography could play a major role. For purifying monoclonal antibodies (mAb) from a harvested cell culture fluid, the standard process is typically protein A affinity and ion exchange chromatography, as the two chromatography steps. The former chromatographic step is used to separate proteins from impurities. The principle involved is the reversible interactions of the Fc portion of a molecule with the protein A ligand that is immobilized on a chromatography matrix [119]. The mAb binds with the column and the impurities flows through the chromatographic matrix. Subsequently, the additional impurities are removed from the column by washing it [120]. The reduction in pH is used as the mechanism for eluting the product from the matrix.

Subsequently, the mAb is usually either flowed through an anion-exchange or bound to a cation-exchange chromatography resin to remove additional leached ligand, like for example, Protein A, potential viruses, host-cell proteins, media derived impurities, DNA and aggregated species [121]. Routinely, hydrophobic interaction or additional polishing ion-exchange chromatography steps are carried out as subsequent steps in the mAb purification process [122]. Jensen first observed the binding of protein A to myriad varieties of human and rabbit serum antibodies [123], and later ascribed the binding of bacterial antigen (antigen A) with its natural antibody specificity. Subsequently, this particular antigen was wrongly confused as a bacterial polysaccharide [124] and later, it was appropriately discerned as a bacterial cell wall protein [125]. This protein was

coined for the first time in 1964 as protein A which differentiates itself from other proteins and polysaccharides [126].

Subsequently the theory that proposed the natural antibody specificity for a given bacterial antigen was refuted. Protein A was later depicted to having binding with Fc portions of antibodies and moreover to antibodies that lacked bacterial antigen specificity [127]. Additionally, studies reported that protein A bound more firmly to Fc fragments of antibodies in comparison to the Fab regions or light chains. Subsequently, in the field of affinity purification of antibodies, efforts were made to immobilize protein A on a solid support and was later patented [128,129]. In 1978, commercialization of the initial protein A resin took place [130]. Protein A was shown to bind itself with a wide array of antibody isotypes that are derived from several species [131]. In 1986, Orthoclone which was coined as the first therapeutic antibody was approved and in the purification process, it incorporated protein A chromatography as a capture step [132]. Subsequently, 86% of FDA submissions witnessed Protein A as the mAb capture step [133]. Prior to this, protein A resins had flow rate, capacity and lifetime, and were also costly from economic point of view.

There have been several studies reported that suggests protein A chromatography to be replaced with alternative purification methods. The frequently discussed alternative is ion exchange chromatography for a mAb capture strategy [133–136]. Antibody or impurity precipitation or crystallization are the other suggested techniques [122,132,137–139]. Protein A has also been suggested to be replaced with alternative protein or synthetic molecule affinity resins [140,141]. However, the performance and availability of protein A resins seem to have significantly increased since 1978. More rigid yet highly porous newer beads allow for high mAb capacities, fast flow rates and low pressure drops [142]. For better performance, optimization of the sizes of beads has been carried out. Plenty of base bead chemistries that include controlled pore glass, cross linked agarose, cross linked cellulose, polystyrene-divinylbenzene, polymethacrylate, polyvinylether and ceramic have been developed for the improvement of protein A performance [142–147].

Protein A resins have tapped the advantages from the removal of animal derived production materials [148]. Improving the way in which protein A ligands bind on beads, e.g. via a single or multi-point linkage, led to an increase in the process capacity and also aided in the improvement of ligand accessibility [142]. Modifications to the various protein A domains and the amino acids in those domains resulted in the betterment of protein A lifetime, mAb Fc specificity, capacity, caustic stability and elution pH [149–151]. Owing to these developments, there has been an

overall upgrade in the quantity of mAb that is produced per unit volume of protein A resin per unit time (productivity).

Since 1978, the productivity and binding capacity of Protein A have increased 4.3 and 5.5% a year respectively. Contrastingly, the operational flow rate of protein A increased significantly from 1978 until 2001 and then remained constant or declined because any new modifications or improvements resulted in mere marginal benefits. There was an evident increase in the productivity of protein A resin and also the mAb bioreactor titer (14% growth) which enabled an economical supply of material for clinical trials. From the economical viewpoint, product sales steers the need for technology improvement. The sales of protein A resin, as indicated by sales of protein A ligand (21% growth), is more or less related closely to the sales of mAbs (20% growth). There was a steep rise of sales around the year 2000 for both the products when mAb therapeutics were approved and consequently, the demand increased in the markets. Protein A membrane adsorbers and monoliths have witnessed a higher productivity in comparison to the traditional packed columns because of their high operational flow rates and short bed heights. Although the current devices are not presently feasible for manufacturing at larger scale, it may serve as a model for enhanced protein A productivity.

1.2. Motivation and Outline

1.2.1. Motivation

Separation processes are the key to the economics of any production – they provide a platform for the exploration of a chemical engineer's ingenuity. Among the most challenging fields in separation processes is that of biopharmaceuticals, especially protein purification. Traditionally, bulk protein purification has been carried out with processes such as precipitation, aggregation and settling, phase separation, size exclusion and electrochemical processes. However, to obtain ultrafine quality proteins and peptides mainly chromatography is used. Chromatography involves the separation of substances based on their level of interaction with the two phases (stationary and mobile) involved in the process. Usually the stationary phase is in the form of column of packed organic or inorganic beads, which are functionalized or derivatized. The feed fluid, which contains the components to be separated, must flow between the packed beads and through them. This presents a challenge in terms of mass transfer limitations and, consequently, high

pressure drops. An exception to this is membrane chromatography where the feed fluid passes by convection through the membrane pores. However, it suffers from non-ideal flow distribution in the membrane device mainly because of cross-flow between the membrane layers and void spaces.

In this context, monoliths have a macroporous structure, extensive binding area and have lower mass transfer resistance and pressure drop than conventional random packed beds [89]. Both properties are critically important in chromatography performance, speed and scale-up [91–93]. Furthermore, while in packed bed chromatography mass transfer rates and pressure drop may be limiting, in monoliths surface interactions determine the overall reaction rate [90,94]. Considering all these, the development of porous monolithic columns has received considerable attention in recent years, especially for application as a chromatographic medium for separating proteins. Monolithic stationary phases have a much higher permeability due to the high porosity (50-70%) and a large, modifiable skeleton [8] leading to them being very effective. Additionally, monoliths usually have a hierarchical porous structure with an intertwined network of channels of 2–8 μm diameter allowing convective transport [153,154], while at the same time enabling effective interaction between the components of the flowing liquid and surface-attached ligands in the column.

Reports suggest that there are various routinely used techniques to fabricate cellular ceramics that include that usage of sacrificial phase, partial sintering, replication, foaming and gel casting [155–157]. Depending on the technique incorporated, a direct relation is seen with the morphological properties of the material obtained such as pore size, shape, distribution, tortuosity, interconnectivity, permeability and mechanical strength. Thus, it is essential to channelize efforts to produce hierarchically porous materials that are contiguous and having well-defined end-to-end interconnectivity that could play a critical role in separation processes. From this perspective, gel-casting has made a standpoint of being an effective technique for accomplishing the desired objectives [158–160].

Molded structures with near-finished shape can be prepared by gel casting that are similar to the ones prepared by polymer manufacturing. Besides this advantage, scale-up is not an issue as the molds are used to make the process easier. Moreover, many different shapes with varied porosities can be porosities by playing around with the additives and molds incorporated to have highly porous structures to imperviously dense materials [153,161]. Once the emulsion is formed, it can be placed easily into the molds as the appearance is like putty. After achieving the desired

shaped, the material is heated at elevated temperatures in the oven to burn out the dispersed phase and to consolidate the ceramic material obtaining a finished product. Therefore, applying this method scalable monolithic columns can be quickly and efficiently produced.

Although, inorganic monoliths have several advantages from the mass transfer perspective, they are inherently inert as they are usually composed of earth minerals. There are several techniques available to functionalize such materials, ranging from physical methods like vapor deposition or sputtering, to chemical modification methods like chemical etching or silanization [162–168]. Silanization is a versatile method, mainly because of a wide variety of available silane agents which can proffer different functional groups to the surface as required. This means there is a tremendous scope to develop materials for a variety of purposes from catalysis to protein separation. It is well documented that proteins interact with aldehyde, amine or epoxy groups most effectively [166,169–172]. Therefore, there are several possibilities from the perspective of silane agents which can be used to functionalize a column for protein separation. Amino silanes are among the most economical and easily available. They also tend to form strong bonds with proteins and therefore are quite popular. However, there are also certain problems associated with the use of amine agents ie., they tend to affect material integrity and cause etching [164]. Therefore, it is important to achieve a balance between available amine groups and column integrity.

There are several factors which influence silanization. The effect of humidity is well documented as it supplies the necessary OH groups for the formation of silanol complexes [169,171,172][13,19–20] and is therefore critical to the process. Further, factors such as precursor concentration and number of silanization coats influence the density and availability of functional groups. The reaction temperature plays a major role in the preservation of structural integrity by reducing etching [164,176]. It is therefore imperative that these factors are optimized to obtain ideal conditions, and thus effective media for separation/purification.

From the standpoint of application, the monolith morphology plays a key role in determining fluid flow hydrodynamics and mass transfer properties [177]. The microporous structure governs the fluid flow dynamics and associated fluid dispersion [178], whereas the intra-skeleton mesoporous structure determines the mass transfer resistance and diffusion mechanisms (bulk and/or surface diffusion; Knudsen diffusion, etc.) [178]. The heterogeneity of the microporous space, variable thickness of the skeleton wall and/or border layer trans-column eddy dispersion effects lead to flow velocity bias at various scales and a consequent fluid dispersion [179,180]. Therefore, the

separation process efficiency is related with the width of the residence time distribution (RTD) curve, which is influenced by the mobile phase velocity and the monolith morphology [178]. A narrow residence time distribution and a small band broadening are desirable, since this means small hydrodynamic dispersion and fast mass transfer into and out of the porous media [178].

To visualize and gain better knowledge about the internal structure of a monolith, most of the reported studies involve the use of scanning electron microscopy (SEM) [181–186] or confocal laser scanning microscopy (CLSM) [187–191,191–194], wherein dyes are used to stain the samples and obtain images through the depth of the sample. In such a way, a number of 2D image slices are obtained, which are used to construct a 3D virtual structure of the monolith and to perform a quantitative morphological image analysis. Such reconstructed structures were also used for simulation of flow profiles and dispersion within monoliths by the Lattice-Boltzmann method (LBM), allowing to correlate their morphological properties, by calculating the Darcy permeability, fluid velocities dispersion/distribution, pressure gradient and plate height [183,189,190,192,195]. Recently, a commercial computational fluid dynamics (CFD) tool, Starccm+, was used to calculate velocity fields, streamlines, pressure drop and permeability in a polymethacrylate-based monolith reconstructed from 898 image slices, of 50 nm each, acquired by SEM [185]. The images resolution was 1024 x 1024 pixels (pixel size 98 nm) and the reconstructed cubic block had an edge length of 45 µm. The choice of the column region to perform simulations is puzzling since the monolith may present internal differences between regions which are created during the manufacturing process [196].

X-ray tomography (where the actual 3D object is reconstructed from 2D images acquired at different angles of the sample [197]) has been used so far to access the morphology of packed bed chromatography columns, analyse their porosity, tortuosity and identify axial and radial morphologic heterogeneity [198]. In a similar way, X-ray tomography was used to reconstruct the arrangement of slurry electrodes and visualise percolation pathways [199] and to obtain accurate representations of a spacer filament shape, used later to perform CFD simulations [197]. CFD simulations using X-ray tomography images were found to be close to experimentally obtained results, indicating that the images obtained are suitable to approximate real feed-side spacer geometries [197].

Monoliths comprising co-polymers of ethylene dimethacrylate (EDMA) and Glycidyl methacrylate (GMA) are the most commonly available commercial monoliths [170–172] used for antibody purification. These monoliths are popular because they are easy to synthesize and modify.

Correspondingly, they can be fabricated to have a variety of pore sizes, surface areas and shapes. This property makes them particularly beneficial to adapt these supports with proteins that are known to be larger binding agents [153,154,200]. However, their main disadvantage as a support is that they have a smaller surface area when compared to the traditional particulate supports or monoliths. Thus, the volume of binding agent to immobilize on a support is limited [152–154,174,176,200,201].

Agarose is another contender which offers several advantages including low non-specific binding among biological matrices, higher stability for a broad pH range, ease of modification to immobilize several binding agents and intrinsically large pore size. Thus, for several years, agarose has been routinely incorporated as a support in traditional affinity chromatography [89,91,94]. Nevertheless, its major drawback to be utilized in those applications involving HPLC is that it is fragile and displays lower mechanical stability [89,94]. However, agarose can be crosslinked or blended with different polymers to harden it and thus, allowing itself to be incorporated in relatively high-performance separations [94].

However, compared to inorganic monoliths comprising materials like silica, zirconia, and others, organic monoliths have a low surface area (in tens of $m^2.g^{-1}$) due to the lack of mesopores. This hampers their application for the separation of small molecules like peptides [202]. They are also less stable in harsher environments like extreme pH or high temperature as compared to inorganic monoliths.

Adding to these are the necessary considerations of sustainability and environmental impact, which are gaining importance each passing day. Presently, the need to have efficient systems for purifying active molecules like therapeutic proteins and peptides seems to outweigh the need for proper assessment and development of a strategy to ensure a reduced effect on the environment when using said methods. However, with ever growing concerns regarding their immediate impact, especially synthetics like polymers and how we dispose of them, it is quite probable that equipment used for separations will soon come under the scanner.

In this thesis, I aim to demonstrate the development of monolithic columns for affinity chromatography. I have developed a simplified modified silanization method to produce amine functionalized alumina monoliths using (3-Aminopropyl)triethoxysilane as the silane agent at relatively moderate conditions. The functionalized monoliths have been characterized by specific analytical techniques, including FTIR, SEM-EDX, XPS and ninhydrin assay to determine the type

of bond, binding strength, distribution and quantity of available amine groups throughout the monolith. Further, we have optimized the silanization parameters like temperature, pH, humidity (Relative Humidity, RH), initial precursor concentration and number of coatings to obtain monoliths with most favorable characteristics considering their future application for IgG purification. In this regard, we have carried out proof of concept studies using these monoliths and assessed the effectiveness of binding Protein A and Protein G to these columns.

1.2.2. Outline

Chapter 1 - Introduction

- Literature: State-of-the-Art
- Motivation & outline

Chapter 2 - Development: Emulsion-Gel Casting of Alumina Monoliths

- Expanded on the emulsion-gel casting process
- Developed novel relationships between rheological parameters and monolith morphology

Chapter 3 - Functionalization: Amine Modification of Monoliths

- Developed novel single-step coating process using APTES
- Optimized reaction parameters of coating process

Chapter 4 - Modelling: Fluid Dynamic Simulation Studies

- Studied Computational Fluid Dynamics approach to simulate fluid flows
- Calculated and validated tortuosity and Residence Time Distribution

Chapter 5 - Application: Protein Attachment Studies

- Tested applications of developed functionalized monoliths for protein separation

Chapter 6 - Conclusion: Outlook and Future Perspectives

- The End? or a Beginning....

Work Summary

Chapter 1: Introduces the topic of discussion with current state-of-the-art relating to bio separations, monolithic chromatography columns and protein separation by affinity chromatography. This is followed by highlighting the motivation of the work and the outline of the thesis.

Chapter 2: This chapter details the process of producing monolithic columns with α-alumina, using emulsion gel casting. The rheology of the emulsion-gel is related to the final morphology of the monolithic column.

Chapter 3: In this chapter, attempts are made to digitally re-construct the column using data from X-ray µ-tomography and explore the fluid dynamics that take place within this column. Moreover, this chapter deciphers the convective nature of the flow, finds the probable tortuous path of the fluid through the column and experimentally validates the computational observations by conducting a simple tracer experiment. This work was carried out during the Erasmus Mundus Mobility in Université Paul Sabatiér, Toulouse. FR.

Chapter 4: In this chapter, we discuss strategies for functionalizing the monolithic column to further the objective of attaching Protein A to the column. The processes behind selecting APTES as the silane agent is described. Furthermore, the steps followed to functionalize the column and optimize the functionalization in terms of % humidity, number of coats and precursor concentration is highlighted. Finally, the proof of concept experiment using Protein A and IgG is exhibited.

Chapter 5: This chapter discusses the possible mechanism of attachment of proteins to the column. The attachment of BSA at different concentrations to the column is studied in terms of kinetics. Based on these results, mathematical models of isotherms were used to understand the attachment mechanism better. Finally, Protein G was attached to the amine functionalized monolith, then adsorption-elution of Immunoglobulin G with respect to the column was tested. This work was carried out during the Erasmus Mundus Mobility in ITM-CNR, Universita della Calabria. IT

Chapter 6: Finally, chapter 6 concludes the findings and point out paths for future researchers to explore in the area of monolithic chromatography.

References

[1] Robert Bud. <italic>The Uses of Life: A History of Biotechnology</italic>. New York: Cambridge University Press. 1993. Pp. xvii, 299. $49.95, Am. Hist. Rev. (1994). doi:10.1086/ahr/99.5.1642-a.

[2] S.. Junod, Celebrating a milestone anniversary, FDA U.S Food Drug Adm. (2007).

[3] K. Cornely, Biopharmaceuticals: Biochemistry and biotechnology, 2nd edition: Walsh, Gary, John Wiley & Sons, Biochem. Mol. Biol. Educ. (2007). doi:10.1002/bmb.2004.494032029997.

[4] R. Otto, A. Santagostino, U. Schrader, Rapid growth in biopharma : Challenges and opportunities, McKinsey Q. (2014).

[5] International Federation of Pharmaceutical Manufacturers, The Pharmaceutical Industry and Global Health Facts and Figures 2017, Int. Fed. Pharmacutical Manuf. Asoc. (2017).

[6] D. Gupta, G.N. Prashanth, S. Lodha, A CMO perspective on quality challenges for biopharmaceuticals, Bioprocess Int. (2013).

[7] G. Walsh, Biopharmaceutical benchmarks 2010, Nat. Biotechnol. 28 (2010) 917. https://doi.org/10.1038/nbt0910-917.

[8] M.N. Gupta, B. Mattiasson, Novel technologies in downstream processing, in: Chem. Ind., Chemistry & Industry, London, 1994: pp. 673–675.

[9] P.B. Kakarla, Radical Optimization of Expanded Bed Chromatography by the Implementation of an Interaction Energy Predictive Framework, 2016. http://nbn-resolving.org/urn:nbn:de:gbv:579-opus-1006588.

[10] M. Petro, D. Berek, Polymers immobilized on silica gels as stationary phases for liquid chromatography, Chromatographia. (1993). doi:10.1007/BF02275796.

[11] G. Schomburg, Polymer coating of surfaces in column liquid chromatography and capillary electrophoresis, Trends Anal. Chem. (1991). doi:10.1016/0165-9936(91)85119-C.

[12] A. Zydney, Perspectives on integrated continuous bioprocessing - opportunities and challenges, 2015. doi:10.1016/j.coche.2015.07.005.

[13] S.S. Maitra, A.K. Verma, End of small volume high value myth in biotechnology - Process design for a mega-plant producing γ-interferon for mega profit, J. Inst. Eng. Chem. Eng. Div. (2003).

[14] A.L. Zydney, Continuous downstream processing for high value biological products: A Review, Biotechnol. Bioeng. 113 (2016) 465–475. doi:10.1002/bit.25695.

[15] V. Warikoo, R. Godawat, K. Brower, S. Jain, D. Cummings, E. Simons, T. Johnson, J. Walther, M. Yu, B. Wright, J. Mclarty, K.P. Karey, C. Hwang, W. Zhou, F. Riske, K. Konstantinov, Integrated continuous production of recombinant therapeutic proteins, Biotechnol. Bioeng. (2012). doi:10.1002/bit.24584.

[16] X. Xu, J. Hirpara, K. Epting, M. Jin, S. Ghose, S. Rieble, Z.J. Li, Clarification and capture of high-concentration refold pools for E. coli-based therapeutics using expanded bed adsorption

chromatography, Biotechnol. Prog. (2014). doi:10.1002/btpr.1833.

[17] N. Koshida, H. Koyama, Visible electroluminescence from porous silicon, Appl. Phys. Lett. (1992). doi:10.1063/1.106652.

[18] B.B. Lakshmi, C.J. Patrissi, C.R. Martin, Sol-Gel Template Synthesis of Semiconductor Oxide Micro- and Nanostructures, Chem. Mater. (1997). doi:10.1021/cm970268y.

[19] S.Y. Huang, G. Schlichthörl, A.J. Nozik, M. Grätzel, A.J. Frank, Charge Recombination in Dye-Sensitized Nanocrystalline TiO2 Solar Cells, J. Phys. Chem. B. 101 (1997) 2576–2582. doi:10.1021/jp962377q.

[20] J.S. Yi, T. Van Nguyen, Multicomponent Transport in Porous Electrodes of Proton Exchange Membrane Fuel Cells Using the, J. Electrochem. Soc. (1999).

[21] H.C. Shin, M. Liu, Three-dimensional porous copper-tin alloy electrodes for rechargeable lithium batteries, Adv. Funct. Mater. (2005). doi:10.1002/adfm.200305165.

[22] A.G. Pandolfo, A.F. Hollenkamp, Carbon Properties and Their Role in Supercapacitors, 2006. doi:10.1016/j.jpowsour.2006.02.065.

[23] C.D. Chang, A.J. Silvestri, The Conversion of Methanol and other O-compounds over Zeolite Catalysts, J. Catal. (1977).

[24] J.S. Yu, S. Kang, S.B. Yoon, G. Chai, Fabrication of ordered uniform porous carbon networks and their application to a catalyst supporter, J. Am. Chem. Soc. (2002). doi:10.1021/ja0203972.

[25] M.A. Harmer, W.E. Farneth, Q. Sun, High Surface Area Nafion Resin/Silica Nanocomposites: A New Class of Solid Acid Catalyst, J. Am. Chem. Soc. 118 (1996) 7708–7715. doi:10.1021/ja9541950.

[26] V.S.Y. Lin, K. Motesharei, K.P.S. Dancil, M.J. Sailor, M.R. Ghadiri, A porous silicon-based optical interferometric biosensor, Science (80-.). (1997). doi:10.1126/science.278.5339.840.

[27] A.C. Dillon, K.M. Jones, T.A. Bekkedahl, C.H. Kiang, D.S. Bethune, M.J. Heben, Storage of hydrogen in single-walled carbon nanotubes, Nature. (1997). doi:10.1038/386377a0.

[28] S. Noro, S. Kitagawa, M. Kondo, K. Seki, A New, Methane Adsorbent, Porous Coordination Polymer [{CuSiF6(4,4′-bipyridine)2}n], Angew. Chemie Int. Ed. 39 (2000) 2081–2084. doi:10.1002/1521-3773(20000616)39:12<2081::AID-ANIE2081>3.0.CO;2-A.

[29] M. Eddaoudi, J. Kim, N. Rosi, D. Vodak, J. Wachter, M. O'Keeffe, O.M. Yaghi, Systematic design of pore size and functionality in isoreticular MOFs and their application in methane storage, Science (80-.). (2002). doi:10.1126/science.1067208.

[30] L.L. Hench, Bioceramics: From Concept to Clinic, J. Am. Ceram. Soc. 74 (1991) 1487–1510. doi:10.1111/j.1151-2916.1991.tb07132.x.

[31] M.E. Davis, Ordered porous materials for emerging applications, Nature. (2002). doi:10.1038/nature00785.

[32] S.J. Hollister, Porous scaffold design for tissue engineering., Nat. Mater. (2005). doi:10.1038/nmat1421.

[33] O.L. Hollis, Separation of Gaseous Mixtures Using Porous Polyaromatic Polymer Beads,

Anal. Chem. (1966). doi:10.1021/ac60234a038.

[34] I. Gusev, X. Huang, C. Horváth, Capillary columns with in situ formed porous monolithic packing for micro high-performance liquid chromatography and capillary electrochromatography, J. Chromatogr. A. (1999). doi:10.1016/S0021-9673(99)00697-4.

[35] N. Tanaka, H. Kobayashi, N. Ishizuka, H. Minakuchi, K. Nakanishi, K. Hosoya, T. Ikegami, Monolithic silica columns for high-efficiency chromatographic separations, J. Chromatogr. A. (2002). doi:10.1016/S0021-9673(01)01582-5.

[36] J.R. Li, R.J. Kuppler, H.C. Zhou, Selective gas adsorption and separation in metal-organic frameworks, Chem. Soc. Rev. (2009). doi:10.1039/b802426j.

[37] F. Svec, J.M.J. Fréchet, New designs of macroporous polymers and supports: From separation to biocatalysis, Science (80-.). (1996). doi:10.1126/science.273.5272.205.

[38] A. Thomas, F. Goettmann, M. Antonietti, Hard templates for soft materials: Creating nanostructured organic material, Chem. Mater. (2008). doi:10.1021/cm702126j.

[39] Y. Wan, Y. Shi, D. Zhao, Supramolecular aggregates as templates: Ordered mesoporous polymers and carbons, Chem. Mater. (2008). doi:10.1021/cm7024125.

[40] O.D. Velev, E.W. Kaler, Structured porous materials via colloidal crystal templating: from inorganic oxides to metals, Adv. Mater. (2000). doi:10.1002/(SICI)1521-4095(200004)12:7<531::AID-ADMA531>3.0.CO;2-S.

[41] B.T. Holland, C.F. Blanford, A. Stein, Synthesis of macroporous minerals with highly ordered three-dimensional arrays of spheroidal voids, Science (80-.). (1998). doi:10.1126/science.281.5376.538.

[42] A. Stein, B.J. Melde, R.C. Schroden, Hybrid inorganic-organic mesoporous silicates-nanoscopic reactors coming of age, Adv. Mater. (2000). doi:10.1002/1521-4095(200010)12:19<1403::AID-ADMA1403>3.0.CO;2-X.

[43] S. Fujita, S. Inagaki, Self-organization of organosilica solids with molecular-scale and mesoscale periodicities, Chem. Mater. (2008). doi:10.1021/cm702271v.

[44] J.L.C. Rowsell, O.M. Yaghi, Metal-organic frameworks: A new class of porous materials, Microporous Mesoporous Mater. (2004). doi:10.1016/j.micromeso.2004.03.034.

[45] S. Kitagawa, R. Kitaura, S.I. Noro, Functional porous coordination polymers, Angew. Chemie - Int. Ed. (2004). doi:10.1002/anie.200300610.

[46] K. Sing, D. Everett, R. Haul, L. Moscou, R. Pierotti, J. Rouquérol, T. Siemieniewska, Reporting Physisorption Data for Gas/Solid Systems With Special Reference to the Determination of Surface Area and Porositye, Pure Appl. Chem. 57 (1985) 603–619. doi:10.1351/pac198557040603.

[47] D.W. Breck, W.G. Eversole, R.M. Milton, T.B. Reed, T.L. Thomas, Crystalline Zeolites. I. The Properties of a New Synthetic Zeolite, Type A, J. Am. Chem. Soc. 78 (1956) 5963–5972. doi:10.1021/ja01604a001.

[48] G.T. Kokotailo, S.L. Lawton, D.H. Olson, W.M. Meier, Structure of synthetic zeolite ZSM-5, Nature. (1978). doi:10.1038/272437a0.

[49] T. Kyotani, Control of pore structure in carbon, Carbon N. Y. (2000). doi:10.1016/S0008-6223(99)00142-6.

[50] C.N.R. Rao, A.K. Cheetham, A. Thirumurugan, Hybrid inorganic-organic materials: A new family in condensed matter physics, J. Phys. Condens. Matter. (2008). doi:10.1088/0953-8984/20/8/083202.

[51] T.J. Barton, L.M. Bull, W.G. Klemperer, D.A. Loy, B. McEnaney, M. Misono, P.A. Monson, G. Pez, G.W. Schere, J.C. Vartuli, O.M. Yaghi, Tailored porous materials, Chem. Mater. (1999). doi:10.1021/cm9805929.

[52] T. Yanagisawa, T. Shimizu, K. Kuroda, C. Kato, The preparation of alkyltrimethylammonium-kanemite complexes and their conversion to microporous materials, Bull. Chem. Soc. Jpn. (1990). doi:10.1246/bcsj.63.988.

[53] R. Ryoo, S.H. Joo, S. Jun, Synthesis of Highly Ordered Carbon Molecular Sieves via Template-Mediated Structural Transformation, J. Phys. Chem. B. (1999). doi:10.1021/jp991673a.

[54] U. Ciesla, F. Schüth, Ordered mesoporous materials, Microporous Mesoporous Mater. (1999). doi:10.1016/S1387-1811(98)00249-2.

[55] N.K. Raman, M.T. Anderson, C.J. Brinker, Template-based approaches to the preparation of amorphous, nanoporous silicas, Chem. Mater. (1996). doi:10.1021/cm960138+.

[56] B.T. Holland, C.F. Blanford, T. Do, A. Stein, Synthesis of highly ordered, three-dimensional, macroporous structures of amorphous or crystalline inorganic oxides, phosphates, and hybrid composites, Chem. Mater. (1999). doi:10.1021/cm980666g.

[57] A. Imhof, D.J. Pine, Ordered macroporous materials by emulsion templating, Nature. (1997). doi:10.1038/40105.

[58] F. Cheng, Z. Tao, J. Liang, J. Chen, Template-directed materials for rechargeable lithium-ion batteries, Chem. Mater. (2008). doi:10.1021/cm702091q.

[59] H. Zhang, A.I. Cooper, Synthesis and applications of emulsion-templated porous materials, Soft Matter. (2005). doi:10.1039/b502551f.

[60] Y. Ma, W. Tong, H. Zhou, S.L. Suib, A review of zeolite-like porous materials, Microporous Mesoporous Mater. (2000). doi:10.1016/S1387-1811(99)00199-7.

[61] J. Pérez-Ramírez, C.H. Christensen, K. Egeblad, C.H. Christensen, J.C. Groen, Hierarchical zeolites: Enhanced utilisation of microporous crystals in catalysis by advances in materials design, Chem. Soc. Rev. (2008). doi:10.1039/b809030k.

[62] S. Polarz, M. Antonietti, Porous materials via nanocasting procedures: Innovative materials and learning about soft-matter organization, Chem. Commun. (2002). doi:10.1039/b205708p.

[63] Z.Y. Yuan, B.L. Su, Insights into hierarchically meso-macroporous structured materials, in: J. Mater. Chem., 2006. doi:10.1039/b512304f.

[64] A. Stein, F. Li, N.R. Denny, Morphological control in colloidal crystal templating of inverse opals, hierarchical structures and shaped particles, Chem. Mater. (2008). doi:10.1021/cm702107n.

[65] J. Lee, J. Kim, T. Hyeon, Recent progress in the synthesis of porous carbon materials, Adv. Mater. (2006). doi:10.1002/adma.200501576.

[66] X.S. Zhao, F. Su, Q. Yan, W. Guo, X.Y. Bao, L. Lv, Z. Zhou, Templating methods for preparation of porous structures, in: J. Mater. Chem., 2006. doi:10.1039/b513060c.

[67] B.L. Yang, M. Goto, S. Goto, Enzyme purification by affinity chromatography combined with batchwise adsorption and columnwise elution, J. Chem. Eng. JAPAN. (1989). doi:10.1252/jcej.22.532.

[68] B.-L. Yang, S. Goto, Complete Separation of Albumin and Hemoglobin by Metal Chelate Affinity Chromatography, Sep. Sci. Technol. 26 (1991) 637–645. doi:10.1080/01496399108049905.

[69] J.L. Figueiredo, M.F.R. Pereira, M.M.A. Freitas, J.J.M. Órfão, Modification of the surface chemistry of activated carbons, Carbon N. Y. (1999). doi:10.1016/S0008-6223(98)00333-9.

[70] W. Zhong, H. Liu, C. Bai, S. Liao, Y. Li, Base-Free Oxidation of Alcohols to Esters at Room Temperature and Atmospheric Conditions using Nanoscale Co-Based Catalysts, ACS Catal. 5 (2015) 1850–1856. doi:10.1021/cs502101c.

[71] Q. Sun, N. Wang, D. Xi, M. Yang, J. Yu, Organosilane surfactant-directed synthesis of hierarchical porous SAPO-34 catalysts with excellent MTO performance, Chem. Commun. 50 (2014) 6502–6505. doi:10.1039/C4CC02050B.

[72] J. Liu, G. Jiang, Y. Liu, J. Di, Y. Wang, Z. Zhao, Q. Sun, C. Xu, J. Gao, A. Duan, J. Liu, Y. Wei, Y. Zhao, L. Jiang, Hierarchical Macro-meso-microporous ZSM-5 Zeolite Hollow Fibers With Highly Efficient Catalytic Cracking Capability, Sci. Rep. 4 (2014) 7276. https://doi.org/10.1038/srep07276.

[73] G. Collins, M. Blömker, M. Osiak, J.D. Holmes, M. Bredol, C. O'Dwyer, Three-Dimensionally Ordered Hierarchically Porous Tin Dioxide Inverse Opals and Immobilization of Palladium Nanoparticles for Catalytic Applications, Chem. Mater. 25 (2013) 4312–4320. doi:10.1021/cm402458v.

[74] Q. Sun, Z. Dai, X. Meng, F.-S. Xiao, Porous polymer catalysts with hierarchical structures, Chem. Soc. Rev. 44 (2015) 6018–6034. doi:10.1039/C5CS00198F.

[75] C.M.A. Parlett, K. Wilson, A.F. Lee, Hierarchical porous materials: catalytic applications, Chem. Soc. Rev. 42 (2013) 3876–3893. doi:10.1039/C2CS35378D.

[76] Y. Wei, T.E. Parmentier, K.P. de Jong, J. Zečević, Tailoring and visualizing the pore architecture of hierarchical zeolites, Chem. Soc. Rev. 44 (2015) 7234–7261. doi:10.1039/C5CS00155B.

[77] M. Franco Finol, J. Rooke, S. Siffert, R. Cousin, P. Carniti, A. Gervasini, J.M. Giraudon, B.L. Su, J.F. Lamonier, Hierarchically porous Nb-TiO2 nanomaterials for the catalytic transformation of 2-propanol and n-butanol, New J. Chem. (2014). doi:10.1039/c3nj01132a.

[78] T. Barakat, J.C. Rooke, R. Cousin, J.-F. Lamonier, J.-M. Giraudon, B.-L. Su, S. Siffert, Investigation of the elimination of VOC mixtures over a Pd-loaded V-doped TiO2 support, New J. Chem. 38 (2014) 2066–2074. doi:10.1039/C3NJ01190A.

[79] J.C. Rooke, T. Barakat, J. Brunet, Y. Li, M.F. Finol, J.F. Lamonier, J.M. Giraudon, R.

Cousin, S. Siffert, B.L. Su, Hierarchically nanostructured porous group V b metal oxides from alkoxide precursors and their role in the catalytic remediation of VOCs, Appl. Catal. B Environ. (2015). doi:10.1016/j.apcatb.2014.06.056.

[80] L. Meng, X. Zhang, Y. Tang, K. Su, J. Kong, Hierarchically porous silicon–carbon–nitrogen hybrid materials towards highly efficient and selective adsorption of organic dyes, Sci. Rep. 5 (2015) 7910. https://doi.org/10.1038/srep07910.

[81] S. Chakraborty, Y.J. Colón, R.Q. Snurr, S.T. Nguyen, Hierarchically porous organic polymers: highly enhanced gas uptake and transport through templated synthesis, Chem. Sci. 6 (2015) 384–389. doi:10.1039/C4SC02502D.

[82] G. Srinivas, V. Krungleviciute, Z.-X. Guo, T. Yildirim, Exceptional CO2 capture in a hierarchically porous carbon with simultaneous high surface area and pore volume, Energy Environ. Sci. 7 (2014) 335–342. doi:10.1039/C3EE42918K.

[83] J. Wei, D. Zhou, Z. Sun, Y. Deng, Y. Xia, D. Zhao, A Controllable Synthesis of Rich Nitrogen-Doped Ordered Mesoporous Carbon for CO2 Capture and Supercapacitors, Adv. Funct. Mater. 23 (2013) 2322–2328. doi:10.1002/adfm.201202764.

[84] T.-Y. Ma, H. Li, A.-N. Tang, Z.-Y. Yuan, Ordered, Mesoporous Metal Phosphonate Materials with Microporous Crystalline Walls for Selective Separation Techniques, Small. 7 (2011) 1827–1837. doi:10.1002/smll.201100389.

[85] J. Konishi, K. Fujita, S. Oiwa, K. Nakanishi, K. Hirao, Crystalline ZrO2 Monoliths with Well-Defined Macropores and Mesostructured Skeletons Prepared by Combining the Alkoxy-Derived Sol–Gel Process Accompanied by Phase Separation and the Solvothermal Process, Chem. Mater. 20 (2008) 2165–2173. doi:10.1021/cm703351d.

[86] S. Mitchell, N.-L. Michels, K. Kunze, J. Pérez-Ramírez, Visualization of hierarchically structured zeolite bodies from macro to nano length scales, Nat. Chem. 4 (2012) 825. https://doi.org/10.1038/nchem.1403.

[87] B.L. Yang, S. Goto, Consecutive reaction system combined with batchwise adsorption and columnwise elution, J. Chem. Eng. Japan. (1992). doi:10.1252/jcej.25.229.

[88] C. Teepakorn, K. Fiaty, C. Charcosset, Comparison of Membrane Chromatography and Monolith Chromatography for Lactoferrin and Bovine Serum Albumin Separation, Processes. (2016). doi:10.3390/pr4030031.

[89] L.G. Berruex, R. Freitag, T.B. Tennikova, Comparison of antibody binding to immobilized group specific affinity ligands in high performance monolith affinity chromatography, J. Pharm. Biomed. Anal. (2000). doi:10.1016/S0731-7085(00)00414-3.

[90] D. Josic, A. Buchacher, A. Jungbauer, Monoliths as stationary phases for separation of proteins and polynucleotides and enzymatic conversion, J. Chromatogr. B Biomed. Sci. Appl. (2001). doi:10.1016/S0378-4347(00)00499-0.

[91] D. Josić, A. Buchacher, Application of monoliths as supports for affinity chromatography and fast enzymatic conversion, J. Biochem. Biophys. Methods. (2001). doi:10.1016/S0165-022X(01)00195-6.

[92] P.E. Gustavsson, P.O. Larsson, Continuous superporous agarose beds in radial flow columns, J. Chromatogr. A. (2001). doi:10.1016/S0021-9673(01)01027-5.

[93] Q. Luo, X. Mao, L. Kong, X. Huang, H. Zou, High-performance affinity chromatography for characterization of human immunoglobulin G digestion with papain, J. Chromatogr. B Anal. Technol. Biomed. Life Sci. (2002). doi:10.1016/S1570-0232(02)00105-8.

[94] Z. Pan, H. Zou, W. Mo, X. Huang, R. Wu, Protein A immobilized monolithic capillary column for affinity chromatography, Anal. Chim. Acta. (2002). doi:10.1016/S0003-2670(02)00511-1.

[95] R. Ghosh, Protein separation using membrane chromatography: Opportunities and challenges, J. Chromatogr. A. (2002). doi:10.1016/S0021-9673(02)00057-2.

[96] C. Charcosset, 5 - Membrane chromatography, in: C.B.T.-M.P. in B. and P. Charcosset (Ed.), Elsevier, Amsterdam, 2012: pp. 169–212. doi:https://doi.org/10.1016/B978-0-444-56334-7.00005-8.

[97] J. Thoemmes, M.-R. Kula, Membrane chromatography - an integrative concept in the downstream processing of proteins, Biotechnol. Prog. 11 (1995) 357–367. doi:10.1021/bp00034a001.

[98] C.-S. Chang, H.-S. Ni, S.-Y. Suen, W.-C. Tseng, H.-C. Chiu, C.P. Chou, Preparation of inorganic–organic anion-exchange membranes and their application in plasmid DNA and RNA separation, J. Memb. Sci. 311 (2008) 336–348. doi:https://doi.org/10.1016/j.memsci.2007.12.034.

[99] A. Jungbauer, R. Hahn, Polymethacrylate monoliths for preparative and industrial separation of biomolecular assemblies, J. Chromatogr. A. (2008). doi:10.1016/j.chroma.2007.12.087.

[100] S.H. Huang, S. Roy, K.C. Hou, G.T. Tsao, Scaling-Up of Affinity Chromatography By Radial-Flow Cartridges, Biotechnol. Prog. (1988). doi:10.1002/btpr.5420040306.

[101] V. Orr, J. Scharer, M. Moo-Young, C.H. Honeyman, D. Fenner, L. Crossley, S.Y. Suen, C.P. Chou, Simultaneous clarification of Escherichia coli culture and purification of extracellularly produced penicillin G acylase using tangential flow filtration and anion-exchange membrane chromatography (TFF-AEMC), J. Chromatogr. B Anal. Technol. Biomed. Life Sci. (2012). doi:10.1016/j.jchromb.2012.05.039.

[102] P. Madadkar, Q. Wu, R. Ghosh, A laterally-fed membrane chromatography module, J. Memb. Sci. (2015). doi:10.1016/j.memsci.2015.03.056.

[103] S. Hjertén, J.-L. Liao, R. Zhang, High-performance liquid chromatography on continuous polymer beds, J. Chromatogr. A. (1989). doi:10.1016/s0021-9673(00)91309-8.

[104] F. Svec, J.M.J. Frechet, Continuous rods of macroporous polymer as high-performance liquid chromatography separation media, Anal. Chem. 64 (1992) 820–822. doi:10.1021/ac00031a022.

[105] H. Minakuchi, K. Nakanishi, N. Soga, N. Ishizuka, N. Tanaka, Octadecylsilylated Porous Silica Rods as Separation Media for Reversed-Phase Liquid Chromatography, Anal. Chem. 68 (1996) 3498–3501. doi:10.1021/ac960281m.

[106] J. Randon, S. Huguet, A. Piram, G. Puy, C. Demesmay, J.L. Rocca, Synthesis of zirconia monoliths for chromatographic separations, J Chromatogr A. (2006). doi:10.1016/j.chroma.2005.12.044.

[107] C. Liang, S. Dai, G. Guiochon, A Graphitized-Carbon Monolithic Column, Anal. Chem. 75 (2003) 4904–4912. doi:10.1021/ac030146r.

[108] J. Randon, J.F. Guerrin, J.L. Rocca, Synthesis of titania monoliths for chromatographic separations, J. Chromatogr. A. (2008). doi:10.1016/j.chroma.2008.10.108.

[109] F. Svec, Organic polymer monoliths as stationary phases for capillary HPLC, J. Sep. Sci. (2004). doi:10.1002/jssc.200401825.

[110] R. Bakry, C.W. Huck, G.K. Bonn, Recent applications of organic monoliths in capillary liquid chromatographic separation of biomolecules, J. Chromatogr. Sci. (2009). doi:10.1093/chromsci/47.6.418.

[111] J. Krenkova, F. Svec, Less common applications of monoliths: IV. Recent developments in immobilized enzyme reactors for proteomics and biotechnology, J. Sep. Sci. (2009). doi:10.1002/jssc.200800641.

[112] N.W. Smith, Z. Jiang, Developments in the use and fabrication of organic monolithic phases for use with high-performance liquid chromatography and capillary electrochromatography, J. Chromatogr. A. (2008). doi:10.1016/j.chroma.2007.09.027.

[113] K. Cabrera, Applications of silica-based monolithic HPLC columns, J. Sep. Sci. (2004). doi:10.1002/jssc.200401827.

[114] F.C. Leinweber, U. Tallarek, Chromatographic performance of monolithic and particulate stationary phases. Hydrodynamics and adsorption capacity, J. Chromatogr. A. 1006 (2003) 207–228. doi:10.1016/s0021-9673(03)00391-1.

[115] A.M. Van Nederkassel, A. Aerts, A. Dierick, D.L. Massart, Y. Vander Heyden, Fast separations on monolithic silica columns: Method transfer, robustness and column ageing for some case studies, J. Pharm. Biomed. Anal. (2003). doi:10.1016/S0731-7085(03)00131-6.

[116] K. Miyamoto, T. Hara, H. Kobayashi, H. Morisaka, D. Tokuda, K. Horie, K. Koduki, S. Makino, O. Núñez, C. Yang, T. Kawabe, T. Ikegami, H. Takubo, Y. Ishihama, N. Tanaka, High-Efficiency Liquid Chromatographic Separation Utilizing Long Monolithic Silica Capillary Columns, Anal. Chem. 80 (2008) 8741–8750. doi:10.1021/ac801042c.

[117] R. Majors, Highlights of HPLC 2008: Part I, LCGC North Am. (2008) 676–691.

[118] R.W. Brice, X. Zhang, L.A. Colón, Fused-core, sub-2 μm packings, and monolithic HPLC columns: A comparative evaluation, J. Sep. Sci. (2009). doi:10.1002/jssc.200900091.

[119] A.A. Shukla, B. Hubbard, T. Tressel, S. Guhan, D. Low, Downstream processing of monoclonal antibodies-Application of platform approaches, J. Chromatogr. B Anal. Technol. Biomed. Life Sci. (2007). doi:10.1016/j.jchromb.2006.09.026.

[120] Q. Zhang, A.M. Goetze, H. Cui, J. Wylie, B. Tillotson, A. Hewig, M.P. Hall, G.C. Flynn, Characterization of the co-elution of host cell proteins with monoclonal antibodies during protein A purification, Biotechnol. Prog. (2016). doi:10.1002/btpr.2272.

[121] J.L. Purdie, R.L. Kowle, A.L. Langland, C.N. Patel, A. Ouyang, D.J. Olson, Cell culture media impact on drug product solution stability, Biotechnol. Prog. (2016). doi:10.1002/btpr.2289.

[122] J. Zheng, L. Wang, B. Twarowska, S. Laino, C. Sparks, T. Smith, R. Russell, M. Wang, Caprylic acid-induced impurity precipitation from protein A capture column elution pool to enable

a two-chromatography-step process for monoclonal antibody purification, Biotechnol. Prog. (2015). doi:10.1002/btpr.2154.

[123] K. Jensen, A NORMALLY OCCURRING STAPHYLOCOCCUS ANTIBODY IN HUMAN SERUM, Acta Pathol. Microbiol. Scand. 44 (1958) 421–428. doi:10.1111/j.1699-0463.1958.tb01093.x.

[124] K. Jensen, E. Neter, E.A. Gorzynski, H. Anzai, STUDIES ON TOXIC PRODUCTS OF STAPHYLOCOCCUS1, Acta Pathol. Microbiol. Scand. 53 (1961) 191–200. doi:10.1111/j.1699-0463.1961.tb00400.x.

[125] T. Löfkvist, J. Sjöquist, CHEMICAL AND SEROLOGICAL ANALYSIS OF ANTIGEN PREPARATIONS FROM STAPHYLOCOCCUS AUREUS, Acta Pathol. Microbiol. Scand. 56 (1962) 295–304. doi:10.1111/j.1699-0463.1962.tb04908.x.

[126] A. GROV, B. MYKLESTAD, P.E.R. OEDING, IMMUNOCHEMICAL STUDIES ON ANTIGEN PREPARATIONS FROM STAPHYLOCOCCUS AUREUS, Acta Pathol. Microbiol. Scand. 61 (1964) 588–596. doi:10.1111/apm.1964.61.4.588.

[127] A. Forsgren, J. Sjöquist, “Protein A” from S. aureus. I. Pseudo-immune reaction with human gamma-globulin., J. Immunol. (1966).

[128] H. Hjelm, K. Hjelm, J. Sjöquist, Protein a from Staphylococcus aureus . Its isolation by affinity chromatography and its use as an immunosorbent for isolation of immunoglobulins , FEBS Lett. (1972). doi:10.1016/0014-5793(72)80680-x.

[129] J. Sjoquist, Method of binding immunoglobulin employing a polypeptide from microorganisms, 3,995,018, 1976. https://patentimages.storage.googleapis.com/5c/16/b0/a9cf6320892f75/US3995018.pdf.

[130] P.L. Ey, S.J. Prowse, C.R. Jenkin, Isolation of pure IgG1, IgG2a and IgG2b immunoglobulins from mouse serum using protein A-Sepharose, Mol. Immunol. (1978). doi:10.1016/0161-5890(78)90070-6.

[131] A.C.A. Roque, C.S.O. Silva, M.Â. Taipa, Affinity-based methodologies and ligands for antibody purification: Advances and perspectives, J. Chromatogr. A. 1160 (2007) 44–55. doi:https://doi.org/10.1016/j.chroma.2007.05.109.

[132] B. Lain, Protein a the life of a disruptive technology, Bioprocess Int. (2013).

[133] G.R. Miesegaes, S. Lute, D.M. Strauss, E.K. Read, A. Venkiteshwaran, A. Kreuzman, R. Shah, P. Shamlou, D. Chen, K. Brorson, Monoclonal antibody capture and viral clearance by cation exchange chromatography, Biotechnol. Bioeng. (2012). doi:10.1002/bit.24480.

[134] B. Lain, M.A. Cacciuttolo, G. Zarbis-Papastoitsis, Development of a high-capacity MAb capture step based on cation-exchange chromatography, Bioprocess Int. (2009).

[135] D.K. Follman, R.L. Fahrner, Factorial screening of antibody purification processes using three chromatography steps without protein A, J. Chromatogr. A. (2004). doi:10.1016/j.chroma.2003.10.060.

[136] Y. Tao, A. Ibraheem, L. Conley, D. Cecchini, S. Ghose, Evaluation of high-capacity cation exchange chromatography for direct capture of monoclonal antibodies from high-titer cell culture processes, Biotechnol. Bioeng. (2014). doi:10.1002/bit.25192.

[137] M. Kuczewski, E. Schirmer, B. Lain, G. Zarbis-Papastoitsis, A single-use purification process for the production of a monoclonal antibody produced in a PER.C6 human cell line, Biotechnol. J. (2011). doi:10.1002/biot.201000292.

[138] J.K. Eggersgluess, M. Richter, M. Dieterle, J. Strube, Multi-stage aqueous two-phase extraction for the purification of monoclonal antibodies, Chem. Eng. Technol. (2014). doi:10.1002/ceat.201300604.

[139] E. Trilisky, R. Gillespie, T.D. Osslund, S. Vunnum, Crystallization and liquid-liquid phase separation of monoclonal antibodies and fc-fusion proteins: Screening results, Biotechnol. Prog. (2011). doi:10.1002/btpr.621.

[140] F. Detmers, P. Hermans, J.A. Jiao, J.T. McCue, Novel affinity ligands provide for highly selective primary capture, Bioprocess Int. (2010).

[141] A.R. Newcombe, C. Cresswell, S. Davies, K. Watson, G. Harris, K. O'Donovan, R. Francis, Optimised affinity purification of polyclonal antibodies from hyper immunised ovine serum using a synthetic Protein A adsorbent, MAbsorbent® A2P, J. Chromatogr. B Anal. Technol. Biomed. Life Sci. (2005). doi:10.1016/j.jchromb.2004.10.027.

[142] R.L. Fahrner, D.H. Whitney, M. Vanderlaan, G.S. Blank, Performance comparison of protein A affinity-chromatography sorbents for purifying recombinant monoclonal antibodies., Biotechnol. Appl. Biochem. (1999). doi:10.1111/j.1470-8744.1999.tb00902.x.

[143] P. Füglistaller, Comparison of immunoglobulin binding capacities and ligand leakage using eight different protein A affinity chromatography matrices, J. Immunol. Methods. (1989). doi:10.1016/0022-1759(89)90350-5.

[144] P. Shadle, G. Mills, J. Erickson, R. Scott, T. Smith, ANTIBODY PURIFICATION, 5,429,746, 1995. https://patentimages.storage.googleapis.com/b0/ba/af/8b402ab51a4ca9/US5429746.pdf.

[145] Tosoh Bioscience, TOYOPEARL AF-rProtein A-650F, (n.d.). https://www.separations.eu.tosohbioscience.com/solutions/process-media-products/by-mode/protein-a/toyopearl-af-rprotein-a-650f (accessed June 10, 2019).

[146] I. Koji, H. Kitahashi, T. Sato, K. Bando, KANEKA KanCapA???: A new MAb purification platform, Bioprocess Int. (2013).

[147] Merck Millipore, Eshmuno® A Chromatography Media, (n.d.). file:///C:/Users/Usman/Downloads/DS5553EN00_Eshmuno_A_Datasheet_MM.pdf.

[148] Amerhsam Biosciences, Affinity chromatography - rmp Protein A Sepharose Fast Flow, (n.d.). https://www.gelifesciences.co.jp/catalog/pdf/18114134.pdf (accessed June 10, 2019).

[149] G. Healthcare, L. Sciences, MabSelect SuRe, (n.d.). https://www.bioexpress.com/assetsvc/asset/en_US/id/15233702/contents (accessed June 10, 2019).

[150] S. Ghose, M. Allen, B. Hubbard, C. Brooks, S.M. Cramer, Antibody variable region interactions with protein A: Implications for the development of generic purification processes, Biotechnol. Bioeng. (2005). doi:10.1002/bit.20729.

[151] E. Müller, J. Vajda, Routes to improve binding capacities of affinity resins demonstrated

for Protein A chromatography, J. Chromatogr. B Anal. Technol. Biomed. Life Sci. (2016). doi:10.1016/j.jchromb.2016.01.036.

[152] Z. Walsh, B. Paull, M. Macka, Inorganic monoliths in separation science: A review, Anal. Chim. Acta. (2012). doi:10.1016/j.aca.2012.04.029.

[153] M.F. Sanches, N. Vitorino, J.C.C. Abrantes, J.R. Frade, J.B. Rodrigues Neto, D. Hotza, Effects of processing parameters on cellular ceramics obtained by paraffin emulsified suspensions, Ceram. Int. (2014). doi:10.1016/j.ceramint.2014.01.117.

[154] N. Nayak, N. Vitorino, J.R. Frade, A. V. Kovalevsky, V.D. Alves, J.G. Crespo, C.A.M. Portugal, Design of alumina monoliths by emulsion-gel casting: Understanding the monolith structure from a rheological approach, Mater. Des. (2018). doi:10.1016/j.matdes.2018.07.017.

[155] P. Colombo, Conventional and novel processing methods for cellular ceramics, Philos. Trans. R. Soc. A Math. Phys. Eng. Sci. (2006). doi:10.1098/rsta.2005.1683.

[156] X. Wang, J.H. Li, W.M. Guan, M.J. Fu, L.J. Liu, Emulsion-templated high porosity mullite ceramics with sericite induced textured structures, Mater. Des. (2016). doi:10.1016/j.matdes.2015.10.085.

[157] R. Moreno, B. Ferrari, Effect of the slurry properties on the homogeneity of alumina deposits obtained by aqueous electrophoretic deposition, Mater. Res. Bull. (2000). doi:10.1016/S0025-5408(00)00288-9.

[158] I. Akartuna, A.R. Studart, E. Tervoort, L.J. Gauckler, Macroporous Ceramics from Particle-stabilized Emulsions, Adv. Mater. (2008). doi:10.1002/adma.200801888.

[159] S. Karaman, M.T. Yilmaz, A. Kayacier, M. Dogan, H. Yetim, Steady shear rheological characteristics of model system meat emulsions: Power law and exponential type models to describe effect of corn oil concentration, J. Food Sci. Technol. (2015). doi:10.1007/s13197-014-1434-3.

[160] B. Yuan, H. Wu, X. Sun, G. Wang, H. Li, Fabrication of porous alumina green bodies from suspension emulsions by gelcasting, Mater. Lett. (2012). doi:10.1016/j.matlet.2012.04.112.

[161] M.F. Sanches, N. Vitorino, C. Freitas, J.C.C. Abrantes, J.R. Frade, J.B. Rodrigues Neto, D. Hotza, Cellular ceramics by gelatin gelcasting of emulsified suspensions with sunflower oil, J. Eur. Ceram. Soc. (2015). doi:10.1016/j.jeurceramsoc.2015.03.008.

[162] A.N. Cloud, S. Kumar, M. Kavdia, H.H. Abu-Safe, M.H. Gordon, Protein adsorption on low temperature alpha alumina films for surgical instruments, Thin Solid Films. (2009). doi:10.1016/j.tsf.2008.08.002.

[163] J.A. Howarter, J.P. Youngblood, Optimization of silica silanization by 3-aminopropyltriethoxysilane, Langmuir. (2006). doi:10.1021/la061240g.

[164] R.M. Pasternack, S.R. Amy, Y.J. Chaba, Attachment of 3- Aminopropyl triethoxysilane on Silicon Oxide Surfaces: Dependence on Solution Temperature, Langmuir. 24 (2008) 12963–12971. doi:10.1021/la8024827.

[165] F. Brothier, V. Pichon, Immobilized antibody on a hybrid organic-inorganic monolith: Capillary immunoextraction coupled on-line to nanoLC-UV for the analysis of microcystin-LR, Anal. Chim. Acta. (2013). doi:10.1016/j.aca.2013.07.019.

[166] H. Mansur, R. Oréfice, M. Pereira, Z. Lobato, W. Vasconcelos, L. Machado, FTIR and UV–vis study of chemically engineered biomaterial surfaces for protein immobilization, Spectroscopy. 16 (2002) 351–360. doi:10.1155/2002/183053.

[167] K.C. Popat, G. Mor, C.A. Grimes, T.A. Desai, Surface modification of nanoporous alumina surfaces with poly(ethylene glycol), Langmuir. (2004). doi:10.1021/la049075x.

[168] S.H. Hyun, S.Y. Jo, B.S. Kang, Surface modification of γ-alumina membranes by silane coupling for CO2 separation, J. Memb. Sci. (1996). doi:10.1016/0376-7388(96)00160-3.

[169] R.M. Pasternack, S.R. Amy, Y.J. Chabal, Attachment of 3-(aminopropyl)triethoxysilane on silicon oxide surfaces: Dependence on solution temperature, Langmuir. (2008). doi:10.1021/la8024827.

[170] K.F. Du, S. Bai, X.Y. Dong, Y. Sun, Fabrication of superporous agarose beads for protein adsorption: Effect of CaCO3 granules content, J. Chromatogr. A. (2010). doi:10.1016/j.chroma.2010.07.046.

[171] Y. Wu, T. Buranda, R.L. Metzenberg, L.A. Sklar, G.P. Lopez, Diazo coupling method for covalent attachment of proteins to solid substrates, Bioconjug. Chem. (2006). doi:10.1021/bc050278m.

[172] A. Nanci, J.D. Wuest, L. Peru, P. Brunet, V. Sharma, S. Zalzal, M.D. McKee, Chemical modification of titanium surfaces for covalent attachment of biological molecules, J. Biomed. Mater. Res. (1998). doi:10.1002/(SICI)1097-4636(199805)40:2<324::AID-JBM18>3.0.CO;2-L.

[173] N. Aissaoui, L. Bergaoui, J. Landoulsi, J.F. Lambert, S. Boujday, Silane layers on silicon surfaces: Mechanism of interaction, stability, and influence on protein adsorption, Langmuir. (2012). doi:10.1021/la2036778.

[174] M.E. McGovern, K.M.R. Kallury, M. Thompson, Role of Solvent on the Silanization of Glass with Octadecyltrichlorosilane, Langmuir. 10 (1994) 3607–3614. doi:10.1021/la00022a038.

[175] K.T. Queeney, Y.J. Chabal, M.K. Weldon, K. Raghavachari, Silicon oxidation and ultra-thin oxide formation on silicon studied by infrared absorption spectroscopy, Phys. Status Solidi Appl. Res. (1999). doi:10.1002/(SICI)1521-396X(199909)175:1<77::AID-PSSA77>3.0.CO;2-F.

[176] K.T. Queeney, Y.J. Chabal, K. Raghavachari, Role of interdimer interactions in NH3dissociation on Si(100)-(2 × 1), Phys. Rev. Lett. (2001). doi:10.1103/PhysRevLett.86.1046.

[177] R. Hahn, M. Panzer, E. Hansen, J. Mollerup, A. Jungbauer, Mass transfer properties of monoliths, in: Sep. Sci. Technol., 2002. doi:10.1081/SS-120002736.

[178] T. Müllner, K.K. Unger, U. Tallarek, Characterization of microscopic disorder in reconstructed porous materials and assessment of mass transport-relevant structural descriptors, New J. Chem. (2016). doi:10.1039/c5nj03346b.

[179] F. Gritti, G. Guiochon, Mass transfer kinetic mechanism in monolithic columns and application to the characterization of new research monolithic samples with different average pore sizes, J. Chromatogr. A. (2009). doi:10.1016/j.chroma.2009.04.034.

[180] F. Gritti, G. Guiochon, Perspectives on the evolution of the column efficiency in liquid chromatography, Anal. Chem. (2013). doi:10.1021/ac3033307.

[181] D. Stoeckel, C. Kübel, M.O. Loeh, B.M. Smarsly, U. Tallarek, Morphological Analysis of

Physically Reconstructed Silica Monoliths with Submicrometer Macropores: Effect of Decreasing Domain Size on Structural Homogeneity, Langmuir. (2015). doi:10.1021/la5046018.

[182] T. Müllner, A. Zankel, A. Höltzel, F. Svec, U. Tallarek, Morphological Properties of Methacrylate-Based Polymer Monoliths: From Gel Porosity to Macroscopic Inhomogeneities, Langmuir. (2017). doi:10.1021/acs.langmuir.7b00337.

[183] H. Koku, R.S. Maier, M.R. Schure, A.M. Lenhoff, Modeling of dispersion in a polymeric chromatographic monolith, J. Chromatogr. A. (2012). doi:10.1016/j.chroma.2012.03.005.

[184] T. Müllner, A. Zankel, C. Mayrhofer, H. Reingruber, A. Höltzel, Y. Lv, F. Svec, U. Tallarek, Reconstruction and characterization of a polymer-based monolithic stationary phase using serial block-face scanning electron microscopy, Langmuir. (2012). doi:10.1021/la3038395.

[185] C. Jungreuthmayer, P. Steppert, G. Sekot, A. Zankel, H. Reingruber, J. Zanghellini, A. Jungbauer, The 3D pore structure and fluid dynamics simulation of macroporous monoliths: High permeability due to alternating channel width, J. Chromatogr. A. (2015). doi:10.1016/j.chroma.2015.11.026.

[186] T. Müllner, A. Zankel, F. Svec, U. Tallarek, Finite-size effects in the 3D reconstruction and morphological analysis of porous polymers, Mater. Today. (2014). doi:10.1016/j.mattod.2014.07.003.

[187] K. Hormann, T. Müllner, S. Bruns, A. Höltzel, U. Tallarek, Morphology and separation efficiency of a new generation of analytical silica monoliths, J. Chromatogr. A. (2012). doi:10.1016/j.chroma.2011.12.008.

[188] K. Hormann, U. Tallarek, Analytical silica monoliths with submicron macropores: Current limitations to a direct morphology-column efficiency scaling, J. Chromatogr. A. (2013). doi:10.1016/j.chroma.2013.08.087.

[189] A. Daneyko, D. Hlushkou, S. Khirevich, U. Tallarek, From random sphere packings to regular pillar arrays: Analysis of transverse dispersion, J. Chromatogr. A. (2012). doi:10.1016/j.chroma.2012.08.024.

[190] D. Hlushkou, K. Hormann, A. Höltzel, S. Khirevich, A. Seidel-Morgenstern, U. Tallarek, Comparison of first and second generation analytical silica monoliths by pore-scale simulations of eddy dispersion in the bulk region, J. Chromatogr. A. (2013). doi:10.1016/j.chroma.2013.06.039.

[191] D. Hlushkou, S. Bruns, U. Tallarek, High-performance computing of flow and transport in physically reconstructed silica monoliths, J. Chromatogr. A. (2010). doi:10.1016/j.chroma.2010.04.004.

[192] D. Hlushkou, S. Bruns, A. Seidel-Morgenstern, U. Tallarek, Morphology-transport relationships for silica monoliths: From physical reconstruction to pore-scale simulations, J. Sep. Sci. (2011). doi:10.1002/jssc.201100158.

[193] S. Bruns, T. Hara, B.M. Smarsly, U. Tallarek, Morphological analysis of physically reconstructed capillary hybrid silica monoliths and correlation with separation efficiency, J. Chromatogr. A. (2011). doi:10.1016/j.chroma.2011.05.090.

[194] S. Bruns, T. Müllner, M. Kollmann, J. Schachtner, A. Höltzel, U. Tallarek, Confocal laser scanning microscopy method for quantitative characterization of silica monolith morphology, in:

Anal. Chem., 2010. doi:10.1021/ac100909t.

[195] D. Hlushkou, S. Bruns, A. Höltzel, U. Tallarek, From pore scale to column scale dispersion in capillary silica monoliths, Anal. Chem. (2010). doi:10.1021/ac101393b.

[196] M.T. Hearn, Trends in additive manufacturing of chromatographic and membrane materials, Curr. Opin. Chem. Eng. (2017). doi:10.1016/j.coche.2017.11.003.

[197] V.A. Haaksman, A. Siddiqui, C. Schellenberg, J. Kidwell, J.S. Vrouwenvelder, C. Picioreanu, Characterization of feed channel spacer performance using geometries obtained by X-ray computed tomography, J. Memb. Sci. (2017). doi:10.1016/j.memsci.2016.09.005.

[198] T.F. Johnson, P.R. Levison, P.R. Shearing, D.G. Bracewell, X-ray computed tomography of packed bed chromatography columns for three dimensional imaging and analysis, J. Chromatogr. A. (2017). doi:10.1016/j.chroma.2017.01.013.

[199] K.B. Hatzell, J. Eller, S.L. Morelly, M.H. Tang, N.J. Alvarez, Y. Gogotsi, Direct observation of active material interactions in flowable electrodes using X-ray tomography, Faraday Discuss. (2017). doi:10.1039/c6fd00243a.

[200] N. Vitorino, J.C.C. Abrantes, J.R. Frade, Cellular ceramics processed by paraffin emulsified suspensions with collagen consolidation, Mater. Lett. (2013). doi:10.1016/j.matlet.2013.02.020.

[201] K.T. Queeney, Y.J. Chabal, M.K. Weldon, K. Raghavachari, Silicon oxidation and ultra-thin oxide formation on silicon studied by infrared absorption spectroscopy, Phys. Status Solidi Appl. Res. (1999). doi:10.1002/(SICI)1521-396X(199909)175:1<77::AID-PSSA77>3.0.CO;2-F.

[202] A. Konala, K.K.R. Tetala, Nanomaterial grafted Microfluidic Columns for Biomolecule Separation at Analytical Scale, in: Nanomater. Chromatogr., 2018. doi:10.1016/b978-0-12-812792-6.00011-x.

CHAPTER 2

Design of alumina monoliths by emulsion-gel casting: understanding the monolith structure from a rheological approach

Published as: *N. Nayak, N. Vitorino, J. R. Frade, A. V. Kovalevsky, V. D. Alves, J. G. Crespo, C. A. M. Portugal, Design of alumina monoliths by emulsion-gel casting: Understanding the monolith structure from a rheological approach, Mater. Des. 157 (2018) 119-129.*

Abstract

Multimodal porous cellular alumina structures (monoliths) were prepared by an emulsion-gel casting technique using eco-friendly and inexpensive lipids such as corn oil, castor oil, margarine and their mixtures as the dispersed phase. The monoliths obtained showed a good mechanical stability, exhibiting compressive strengths in the range of 8-50 $N.mm^{-2}$. Mercury intrusion porosimetry analysis showed that the monoliths produced presented porosities ranging from 28% to 60% and average pore sizes within 0.2-3.2 µm. The formation of the porous networks was interpreted based on combined droplet coalescence, flocculation and Ostwald ripening effects. The presence of such effects along the emulsion storage time led to changes in their viscoelastic and morphological properties, which were found to correlate with structural descriptors of monoliths after sintering (e.g. average pore sizes and porosity). These correlations open up the possibility to anticipate the final structure of the monoliths and adjust emulsion-gel conditions to produce customized cellular structures with fine-tuned porosities and pore sizes, envisaging their application in membrane processes or chromatography.

2.1. Introduction

Macroporous ceramics find applications in a wide variety of areas due to a combination of favourable properties like low thermal conductivity, low density, high porosity and high chemical tolerance [1]. Techniques that enable tuning of porosity, pore morphology and distribution are of great interest to obtain suitable materials for cutting edge applications like in fabrication of porous separation media (e.g. membranes, chromatography stationary phases) for high temperature processes, sensors for chemical and biochemical processes, catalyst carriers, electrodes for batteries and fuel cells and scaffolds for tissue engineering [1-4].

There are several popular techniques to produce cellular ceramics including partial sintering, replication, use of sacrificial phase, foaming and gel casting to name a few [3, 5, 6]. The choice of the technique determines the morphological properties of the material obtained i.e., pore shape, size and distribution, interconnectivity, tortuosity, permeability and mechanical strength. From the perspective of separation processes, development of hierarchically porous, contiguous materials with well-defined end-to-end interconnectivity is of the essence. Gel-casting has proven to be an effective technique [7-9] to achieve these objectives.

The advantage of gel casting is that it allows the preparation of moulded structures with near-finished shape akin to that available in polymer manufacturing [10-11]. The use of moulds leads

to ease in scaling up. Depending on the additives and melds used a wide variety of shapes can be produced with diverse porosities, ranging from imperviously dense to highly porous structures. In the present work, we use the technique of emulsion gel-casting to produce cellular structures. In simple terms, the technique involves creating an emulsion with the continuous phase being the ceramic powder material in a suspension and a dispersed phase being a suitable pore forming substance [12]. Suitable additives are also added to influence factors like pore size and the stability of the emulsion [10, 13, 14]. This emulsion is like putty and can be put into moulds. Once the shape is set, it can be fired in an oven which accomplishes two purposes – burning out the dispersed phase and strengthening/consolidation of the ceramic material. Earlier publications report the preparation of microporous cellular materials through emulsion-gel casting using polymers [15, 16], alkanes [17-19] or other organic solutions as the dispersed phases. In either case, during the firing process there are toxic gases released, which can cause serious harm to the environment as discussed in detail elsewhere [20].

In a previous work, a detailed study was conducted on the use of an eco-friendly and less expensive - sunflower oil, as the dispersed phase in emulsion gel-casting process [10]. In the said work by Sanches et. al [10], the effect of several parameters like the dispersed phase to continuous phase ratio, the effect of collagen (used as structural stabilizer) and the effect of burnout conditions on the morphology of the cellular ceramics formed were discussed in detail. Considering these perspectives, the goal of this work was to obtain an in-depth comprehension on the influence of the properties of commercially available lipids, used as dispersed phases, on the final hierarchical pore morphology of the sintered structure. We analysed the rheological properties of the emulsions formed with the different lipids and discuss the morphology of the final structure in terms of pore size, porosity, mechanical strength relating them to the properties of the emulsion like droplet size distribution and viscosity. This study is aimed to provide useful guidelines for design of cellular ceramics of alumina with fine porous structures which can be used in a multitude of applications from making membrane supports to monolithic chromatography applications.

2.2. Materials and methods

2.2.1. Materials

α-alumina (Alcoa Chimie, CT-3000), Dolapix PC 67 (Zschimmer & Schwarz), Gelatin Porcine Skin (Oxoid – LP0008) sodium lauryl sulphate/SDS (Sigma-Aldrich L-6026, stock concentration of 1g.

L^{-1}) and commercially available corn oil, castor oil and margarine (41% lipids and 59% water) were used.

2.2.2. Preparation of α-alumina suspension

α-alumina suspension in water was used as the dispersion medium. The mass of α-alumina needed to prepare a 50% (v/v) α-alumina suspension was calculated using the density of reactive alumina powder which was found to be ~3.98 $g.cm^{-3}$.To ensure the formation of a stable suspension with fluid consistency a carboxylic acid based agent, Dolapix PC 67, was added in the concentration of 1% (v/v). Dolapix PC67 is a de-flocculant consisting in an amphiphilic molecule with the same isoelectric point as alumina, which coats the alumina particles such that it does not aggregate to form lumps. The suspension was stirred at 1000 rpm for 120 minutes to obtain a stable suspension with smooth consistency.

2.2.3. Preparation of α-alumina emulsion

Oil-in-water emulsions were prepared with pre-defined dispersed phase (V_o) to continuous phase (Vs) ratio of 1.5. Different lipids, i.e. corn oil, castor oil and margarine and lipid mixtures, i.e. corn oil + castor oil (1:1 v/v), margarine + corn oil (1:3 and 3:1 v/v) and corn oil + castor oil + margarine (1:1:1 v/v) were used as dispersed phases whereas aqueous 50% α-alumina suspensions were used as the continuous phase.

The α-alumina solution was added to the dispersed phase under mechanical stirring at 1000 rpm using an overhead stirring motor. Sodium dodecyl sulphate (SDS), an anionic surfactant was added in a concentration of 6% (v/v) and used to stabilize the emulsion. Gelatin (gelatin oxoid) [10-12] was added to the dispersed phase heated at 60 °C in a concentration of 5% (w/v relative to the volume of water in the final emulsion) and used as a structural stabilizer.

The emulsion prepared with the consistency of thick foam was then poured into different pre-greased cylindrical moulds with dimensions of 5 cm length and 1.1 cm diameter and incubated at 40°C, for 72h. This procedure results in the evaporation of the excess of water and gel hardening, sufficiently to form a contiguous monolithic *green body* (precursor of the monolithic structure), which could then be easily removed from the mild (de-moulding).

2.2.4. Sintering of α-alumina green bodies

Once the samples were sufficiently hardened, the resulting consolidated *green bodies*, were separated from the mild (de-moulded) and then sintered in 2 stages. In the first stage the oil droplets, gelatin and surfactant were removed by increasing the temperature well beyond the smoke point of the oils used i.e., around 1000 °C, followed by an isothermal plateau to completely remove the carbon residues. This stage was carried out at very small heating rate, i.e., 1 °C.min^{-1} to avoid the *green body* from exploding due to fast burn out of oil resulting in the build-up of gases within which, during escape, might cause cracks or defects in the column [11]. Despite taking these precautions, it was found that columns containing castor oil were quite often hollowed out or cracked after sintering. This was probably because of the gaseous microenvironment within the furnace chamber leading to slower evaporation of the oils entrapped within the samples themselves. In the second stage, the heating was resumed at a rate of 3 °C min^{-1} until 1550 °C with a 2-hour sintering plateau. Finally, the samples were cooled to room temperature at a rate of 5 °C min^{-1} to obtain suitable cellular monoliths.

2.2.5. Characterization of the dispersed phases and emulsions

The apparent viscosity and viscoelastic properties of the emulsions prepared as described above were studied using a controlled stress rheometer (HAAKE MARSIII, Thermo Scientific) equipped with a plate-plate serrated geometry (diameter 30 mm), with a gap of 1 mm. The samples were equilibrated at 20 °C, for 5 min, after which the apparent viscosity was measured using a steady-state flow ramp in the range of shear rate from 10^{-3} to 400 s^{-1}. Mathematical modelling was performed using MS Excel's Solver tool for fitting the data to Equation 1 using the Levenberg-Marqhardt algorithm. Equation 1 results from the simplification of the Carreau model [21] having into account that the second Newtonian plateau (at infinite shear rate) was never reached.

$$\eta_a = \frac{\eta_0}{\left[1+(\lambda\dot{\gamma})^2\right]^N} \qquad \text{(Equation 1)}$$

where η_a is the apparent viscosity (Pa.s), η_0 is the is the zero shear rate viscosity, λ is the relaxation time constant, $\dot{\gamma}$ is the shear rate and *N* is a dimensionless constant related to the power law index (N = (1 - n)/2). The interfacial tension of the emulsions was measured by Wilhelmy plate technique (3S Tensio, GBX) equipment at a temperature of 20 °C with a plate of dimensions 2 cm x 2 cm. Droplet analysis and imaging were performed through optical microscopy (Eclipse Ti-U, Nikon) using objectives of 10x and 50x, equipped with a camera for

image acquisition. Image analysis was carried out using the ImageJ software [22] and the Sauter mean droplet diameters (at 5 different points for each sample) in each emulsion were calculated.

2.2.6. Structural characterization of the monoliths

Scanning electron microscopy (SU1510, Hitachi) was used to inspect the microstructural features of the sintered monoliths after carbonizing the sample with graphite. Mercury intrusion porosimetry (Autopore, IV 9500, Micromeriti CS) was used to characterize the pore size distribution, mean pore diameter and average porosity of the samples. Compressive strength upon rupture (LR30K, Lloyd) was measured to infer about the mechanical resistance of the monoliths using samples with length: width ratio of 2:1 under a cross head with speed of 15 $mm.min^{-1}$ using about 3 samples per series.

2.3. Results and Discussion

Monoliths should ideally consist of structures with hierarchical porous networks and well interconnected pores. The formation of such structures by emulsification gel casting processes requires the use of high dispersed to continuous phase ratios, in order to ensure a good balance between droplet flocculation, coalescence and ripening with consequent formation of a series of interconnected droplets. These interconnected structures are ultimately stabilized by a gelling agent entrapping all the components in place to obtain a contiguous *green body* (the monolith precursor), which, upon sintering with a specific temperature cycle, yields a highly porous monolithic structure. The final structure of the monolith will be then defined by the emulsion behaviour/stability (e.g. droplet coalescence, flocculation, ripening) along the aging period (or storage time, period of time before sintering where the emulsion system is allowed to set), and thus is intimately related to the rheological characteristics of the emulsions. Therefore, the capacity to design monoliths with a fine-tuned morphology depends on the ability to predict their final structure based on the evolution of the rheological and morphological parameters of the emulsion-gel at different stages of the aging process [23].

Rheology of an emulsion is greatly influenced by several factors, including interfacial tension, particle interaction and droplet dimension, which may vary along the emulsion storage time. As a first approach, optical microscopy was used to study the evolution of the morphological characteristics of the emulsions prepared with pure corn oil, castor oil and margarine, and different mixtures of these oils along aging, i.e. from the freshly made emulsion (0 hours) to the *green body* obtained after a storage time of 72 h (Figs 2.1 and 2.2). Changes in the size and distribution of

droplets are perceptible from comparative analysis of the microscopy images of the samples reflecting varying degrees of flocculation and coalescence along emulsion aging. The increase of the droplet sizes was particularly observed in emulsions prepared with corn oil, margarine and margarine + corn oil (3:1) as may be confirmed through the values listed in Table 2. 1.

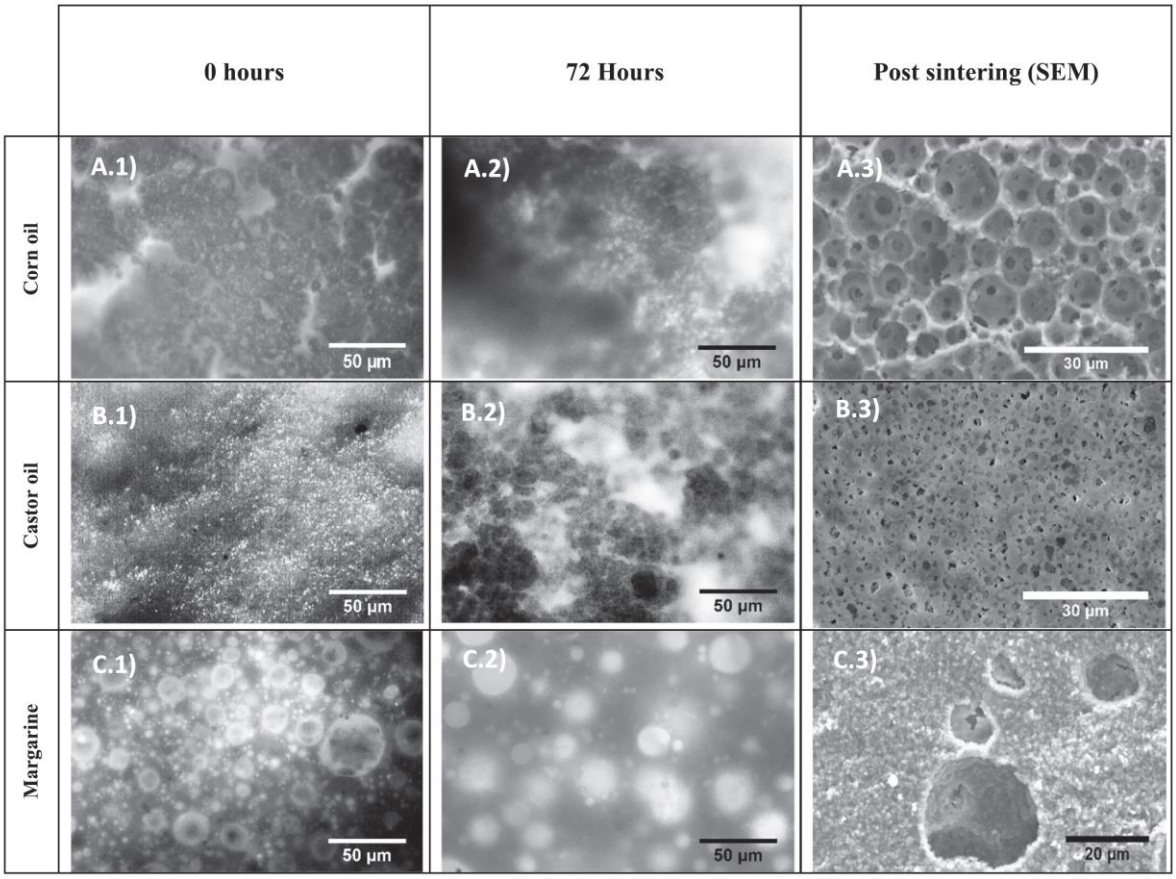

Figure 2.1. Optical microscopy and SEM images of emulsions made with individual oils
Legend: Emulsions made with A.1) Corn oil at 0 hours, A.2) Corn oil at 72 hours, B.1) Castor oil at 0 hours B.2) Castor oil at 72 hours, C.1) Margarine at 0 hours and C.2) Margarine at 72 hours. SEM images of monoliths (i.e., *green bodies* after sintering) obtained using emulsions prepared with A.3) Corn oil, B.3) Castor oil and C.3) Margarine.

Several studies have shown [13, 24, 25] definitive connections between rheological parameters like viscosity and viscoelastic properties with changes in the emulsion stability expressed by droplet coalescence, flocculation, phase inversion and ripening effects [23].

From this perspective, the variability of the rheological properties of the emulsion-gel along the storage time was studied. Viscosity *versus* shear rate profiles were determined for single lipid emulsions prepared with corn oil, castor oil and margarine and emulsions prepared with mixtures of these lipids.

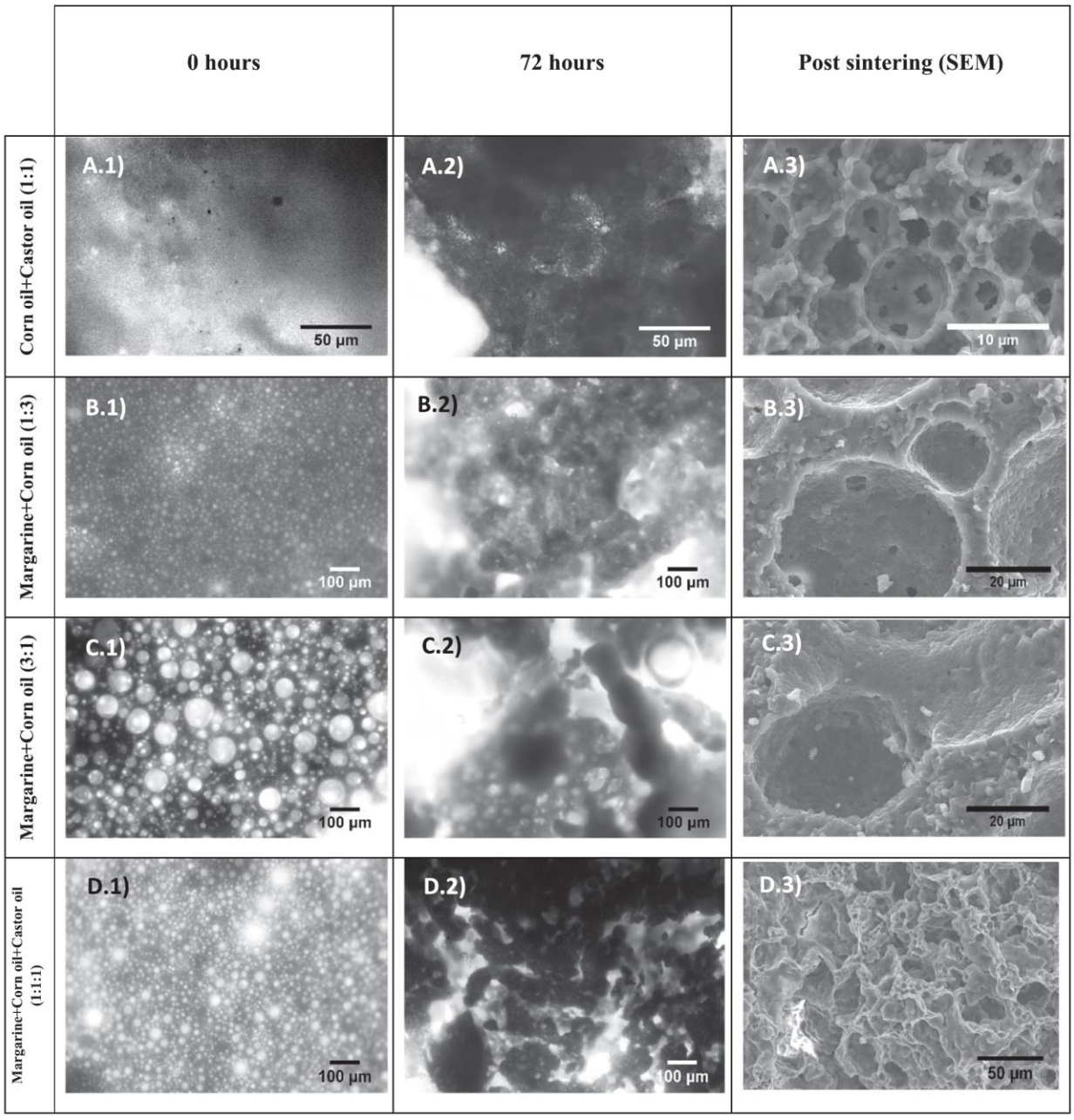

Figure 2.2. Optical microscopy and SEM images of emulsions made with mixture of oils

Legend: Emulsions made with A.1) Corn oil + Castor oil (1:1) at 0 hours, A.2) Corn oil + Castor oil (1:1) at 72 hours, B.1) Margarine + Corn oil (1:3) at 0 hours B.2) Margarine + Corn oil (1:3) at 72 hours, C.1) Margarine + Corn oil (3:1) at 0 hours, C.2) Margarine + Corn oil (3:1) at 72 hours. D.1) Margarine + Corn oil + Castor oil (1:1:1) at 0 hours and Margarine + Corn oil + Castor oil (1:1:1) at 72 hours. SEM images of monoliths (i.e., *green bodies* after sintering) obtained using emulsions prepared with A.3) Corn oil + Castor oil (1:1), B.3) Margarine + Corn oil (1:3), C.3) Margarine + Corn oil (3:1) and D.3) Margarine + Corn oil + Castor oil (1:1:1).

As shown in Fig 2. 3 all the prepared emulsions are non-Newtonian as is apparent from the shape of the viscosity-shear curves, i.e. the emulsion systems depict a shear thinning profile, characterized by the decrease of viscosity at higher shear rates preceded by a Newtonian plateau at lower shear rate values. The non-Newtonian behaviour of the emulsions is observed at both emulsion stages analysed, i.e. immediately after emulsification (0 hours) and after 72 hours of storage.

The plateau region (Newtonian plateau) observed at lower shear rates indicates a limited disruption of the structure of the emulsion at these shear regimes, evidencing the stability of the emulsions. However, as the shear rate increases there is a rapid transition from the Newtonian regime to a shear-thinning behaviour, indicating that both continuous and dispersed phases are flowing, which may lead to significant changes in droplets dimension, particularly at the higher shear rates tested.

To better understand the aging behaviour, data were fit to the simplified Carreau model, as expressed by Equation 1. It was found that the data fit well to this equation ($R^2 > 0.9$), as shown in Fig A1.1 and A1.2 in Appendix. The power law index (or flow index parameter), N, obtained from the fit was <1 for all samples (Table A1. 1 in Appendix.), corroborating the shear thinning behaviour of the emulsions. The relaxation time constant λ (s), which was also obtained from the fitting, is an indicator of the transition from Newtonian to shear-thinning regime whereas its reciprocal, i.e. $1/\lambda$, represents the shear rate at which this transition takes place. Therefore, a decrease of λ, upon storage (as observed for emulsions prepared with single oils, i.e. corn and castor oils) may be ascribed to the loss of structural cohesion of the emulsions and associated to the increase of the droplet size (coalescence effects).

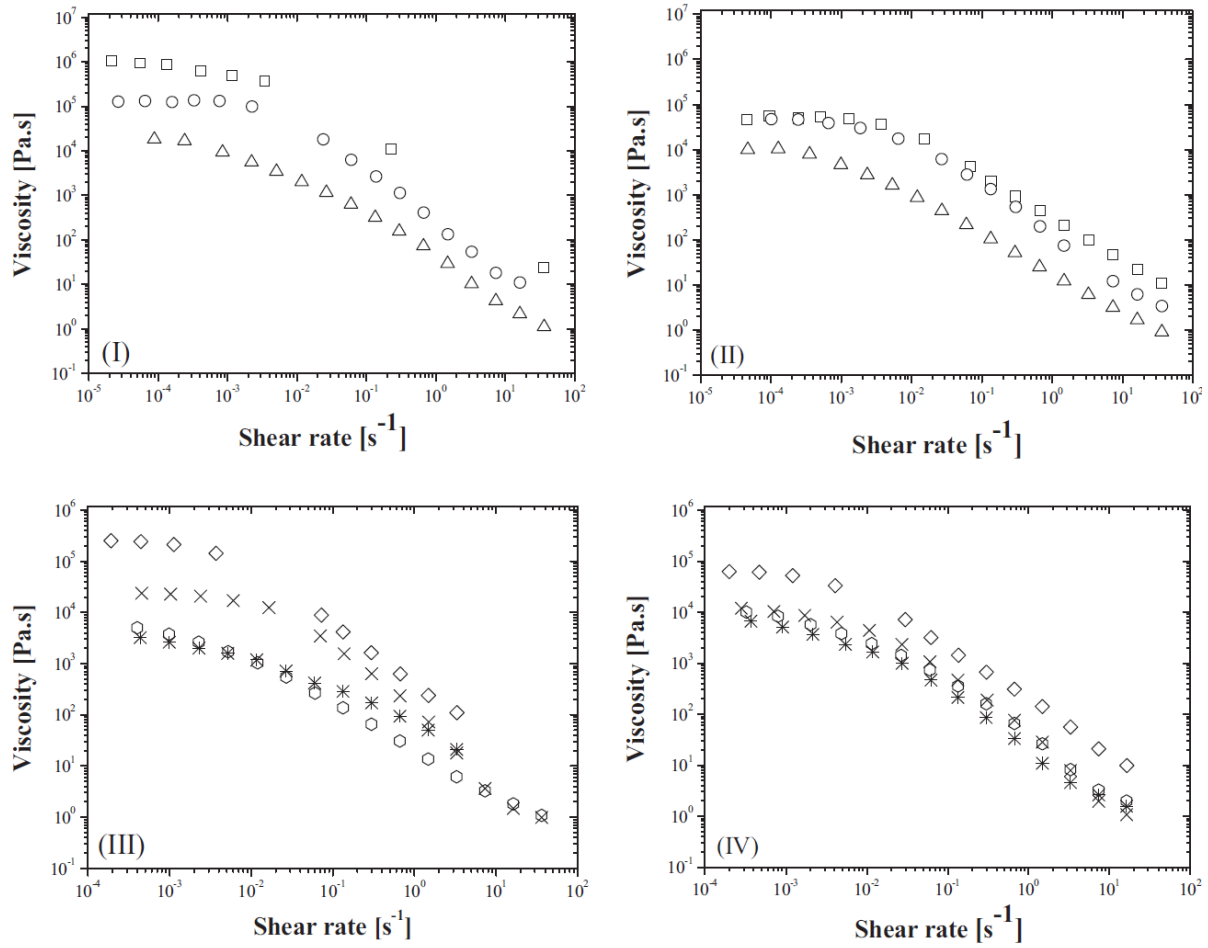

Figure 2.3. Viscosity vs. shear rate profiles for emulsions made with oils
Legend: Emulsions made with I) Corn oil [□] Margarine [△] and Castor oil [○] for 0 hours II) Corn oil [□] Margarine [△] and Castor oil [○] after 72 hours III) Corn oil + Castor oil (1:1) [◊],Margarine + Corn oil (1:3) [×]

The droplet size also influences the apparent viscosity, η_a of the emulsions obtained from the value of viscosity at the Newtonian plateau. Higher droplet sizes are commonly associated to lower viscosities. This relation is clearly observed in Table A1.1 (Appendix), which shows that emulsions with lower droplet sizes, such as that obtained from pure castor and corn oils or the mixture of these two oils, are those that also exhibit higher apparent viscosities. Instead, the emulsions prepared with dispersed phases containing margarine showed lower apparent viscosities and larger droplet sizes.

The presence of droplet coalescence effects may thus be inferred by comparative analysis of the changes of the Newtonian plateau viscosity obtained for freshly prepared emulsions and after storage (72 hours) as shown in Fig 2. 4 and Table A1.1 (in Appendix.). Correlations between droplet coalescence and changes in the viscosity were clear for emulsions made of single oils.

The decrease in the apparent viscosity observed with storage for emulsions made from corn oil and margarine, may be ascribed to the droplet coalescence taking place along with other minor effects [23].

Droplet coalescence, and its relation to changes in the apparent viscosity, was not that clear in the case of emulsions prepared using oil mixtures as the disperse phases. The droplet coalescence observed in emulsion prepared using margarine + corn oil (3:1) was followed by an increase of the apparent viscosity with storage while emulsions prepared with margarine + corn oil (1:3) and margarine + corn oil + castor oil (1:1:1) displayed a decrease of the droplet size after 72h. The absence of droplet coalescence observed in these latter cases seems to indicate a balance in the distribution of the droplets of different oils present in the emulsion minimizing the droplet coalescence.

Table 2.1. Time relaxations, λ (s) and average droplet diameter (d3,2) (μm) of the emulsions used to produce the cellular alumina structures

Dispersed phase	λ [s]	Average droplet diameter ($d_{3,2}$) [μm]
0 hours		
Corn oil	414.22	1.80±0.12
Castor oil	350.16	0.90±0.19
Margarine	2932.42	8.20±0.8
Corn oil + Castor oil (1:1)	194.92	1.30±0.23
Margarine + Corn oil (1:3)	193.2	10.10±1.1
Margarine + Corn oil (3:1)	443.77	12.40±1.2
Marg. + Corn oil + Castor oil (1:1:1)	998.97	11.30±1.8
72 hours		
Corn oil	296.56	3.40±0.21
Castor oil	102.30	1.10±0.16
Margarine	2993.85	14.00±1.2
Corn oil + Castor oil (1:1)	233.52	1.30±0.08
Margarine + Corn oil (1:3)	202.19	8.70±1.5
Margarine + Corn oil (3:1)	248.37	15.20±2.2
Marg. + Corn oil + Castor oil (1:1:1)	233.27	10.30±1.63

These results show that there is no unequivocal relationship between changes of apparent viscosity and droplet size evidencing that besides the droplet dimension, other factors, such as

the presence of surfactants and the effect of alumina particles, could explain the heterogeneity of the behaviours found in the different emulsions systems studied and later on the distinct monolithic structures, as shown in the third column of Fig 2. 1 and Fig 2. 2.

Viscoelastic tests were performed to further understand the effect of droplet distribution on the stability and the final microstructure of the sintered samples. Frequency sweeps were performed to evaluate the viscoelastic properties of emulsions. The storage modulus (G'), loss modulus (G") and the tangent of loss angle (tan δ) were determined. Fig 2. 4 (I, II) and Fig 2. 5 (I, II), show the values of G' and G" at 20 °C for emulsions obtained with the different oils and oil mixtures, at 0 and 72 hours.

Most of the emulsions (except those containing margarine) followed a gel like behaviour with the values of G' about 1 or more orders of magnitude higher than values of G" within the tested frequency range. Such behaviour is commonly seen in highly flocculated or nearly coalesced emulsions [13, 24]. A region of frequency independence for the values of G' can be observed (a plateau region) for most of the tested samples, which has been related to the formation of an elastic structural network which confers a high stability to the emulsion [8, 25]. This characteristic progressively disappears as the content in margarine increases and it is absent for emulsions made with pure margarine.

The reason for such behaviour is that margarine is a pre-existing emulsion, made of 59% water, including surfactants, additives and flavouring agents and has only about 41% of lipids. This drastically alters the volume fraction of the dispersed phase and consequently the distribution of the oil droplets present in the final alumina emulsion-gel. After 72 hours of storage, on applying an oscillatory stress, this emulsion showed a highly viscous behaviour (liquid-like) at lower frequencies, in contrast to all the other samples, with a crossover point of G' and G'' observed at higher frequencies (10 Hz). This behaviour suggests the presence of fluid emulsions composed of a weak network of entangled molecular chains and weak droplet interaction, as a result of intense structural changes, possibly involving droplet coalescence and Ostwald ripening effects with consequent phase separation [23].

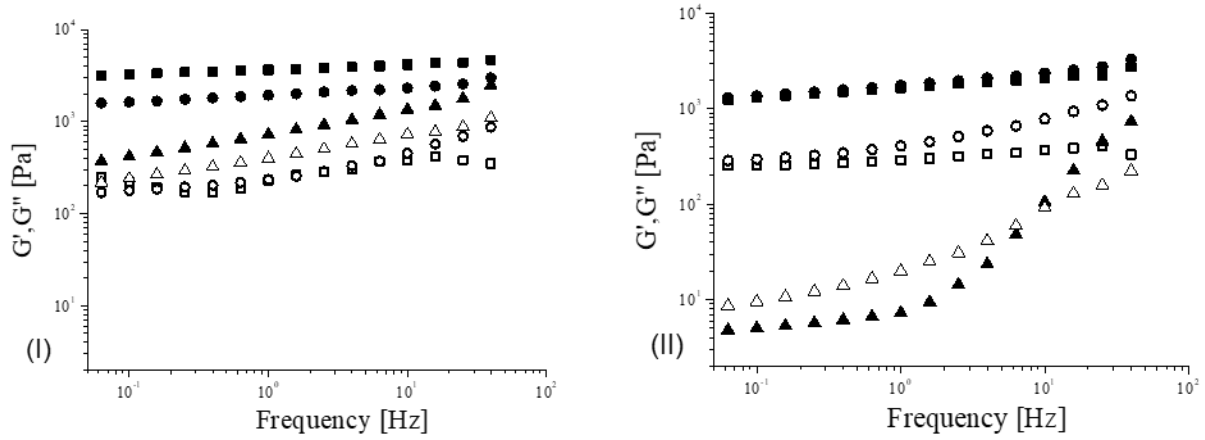

Figure 2.4. Oscillatory viscoelastic profiles for emulsions made with individual oils
Legend: Emulsions made with I) Corn oil (■ - G', □ - G"), Castor oil (● - G', ○ - G") and Margarine (□ - G', △ - G") for 0 hours II) Corn oil (■ - G', □ - G"), Castor oil (● - G', ○ - G") and Margarine (□ - G', △ - G") after 72 hours.

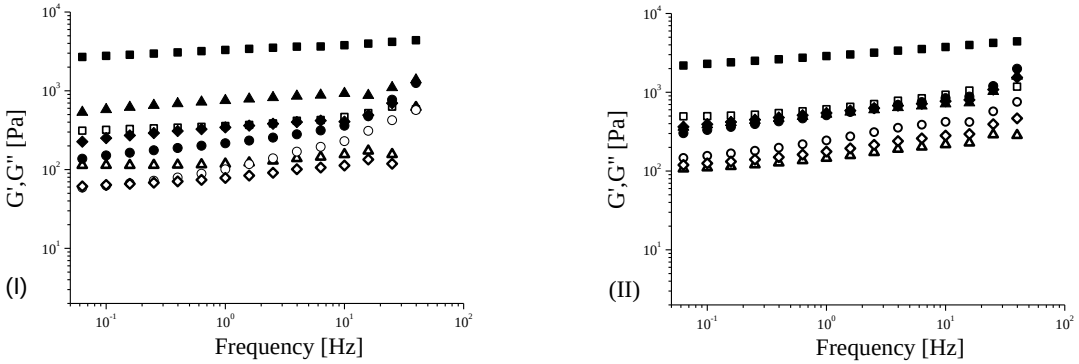

Figure 2.5. Oscillatory viscoelastic profiles for emulsions made with mixture of oils
Legend: Emulsions made with I) Corn oil + Castor (■ - G', □ - G"), Margarine + Corn oil (1:3)(□ - G', △ - G"), Margarine + Corn oil (3:1) (● - G', ○ - G") and Margarine + Corn oil + Castor oil (1:1:1) (□- G', □ - G") for 0 hours II) Corn oil + Castor (■ - G', □ - G"), Margarine + Corn oil (3:1) (● - G', ○ - G"), Margarine + Corn oil (1:3)(□ - G', △ - G") and Margarine + Corn oil + Castor oil (1:1:1) (□- G', □ - G") for 72 hours of storage.

The tan δ was used to calculate an approximate value of the plateau modulus (G_N^0) which can be seen in Table A1. 1 (in Appendix). Stiffer gels tend to have higher values of G' and smaller values of tan δ [26] as is the case of corn oil containing emulsions.

Over the 72-hours period, it was also apparent that the values of the storage modulus (G') for the pure corn oil and margarine systems decreased significantly; while for castor oil and the mixtures of corn oil + castor oil (1:1) and margarine + corn oil (1:3) the decrease was smaller. The decrease

of G' (which may be analysed based on the variation of G_N^0) reflects the presence a less structured emulsion. Contrastingly, the storage and loss moduli, G' and G" increased for the mixtures of margarine + corn oil (3:1) and margarine + corn oil + castor oil (1:1:1) indicating that these systems are stable. This stability is also confirmed by the absence of droplet coalescence effects along the emulsion storage, as evidenced by the negligible changes in droplet size as shown in Table 2. 1. These emulsions seemed to have achieved a balance between the surfactant necessary for stabilizing the emulsion and the volume fraction of oil droplets present, reaching a stabilized emulsion with homogeneously dispersed droplets. It can also be seen that the values of G' and G" seem to be converging with storage for all samples, which means that the viscous component was gaining dominance over the elastic component, envisaging that with longer storage the de-stabilization of the emulsion may occur eventually showing the mechanical spectra of a predominantly viscous behaviour.

It is interesting to note that, in addition to a significant decrease in the values of the moduli (G' and G") with storage, the emulsion prepared with pure margarine exhibit a higher dependence of G´ and G'' on the oscillatory frequency. The increase of G' and G'' with frequency observed is indicative of a decrease of the emulsion cohesion, possibly due to the presence of limited flocculation but significant Ostwald ripening and coalescence, meaning that larger droplets are indeed formed but they are not interconnected. As explained before, this is probably due to the effect of the composition of margarine, which reduces the proportion of the dispersed phase (oil) in the emulsion, while affecting the emulsion stability. This effect is also observable in the other emulsions containing margarine, prepared with mixtures of oils, though it is somewhat mitigated due to the presence of castor and corn oils, decreasing the volume fraction of margarine in the emulsion. However, significantly larger droplet sizes are also observed in these mixtures, albeit interconnected.

Attempts to correlate rheology and microstructural parameters of high internal phase ratio emulsions may be found in the literature. Princen and Kiss [27] proposed an equation that related the low-strain elastic modulus (G') to the interfacial tension (σ), the volume fraction of the dispersed phase (ϕ) and the Sauter mean droplet diameter ($d_{3,2}$), for highly concentrated poly dispersed emulsions as:

$$G' \propto \frac{\sigma}{d_{3,2}} \varphi^{1/3} \qquad \text{(Equation 2)}$$

This equation was applied to the data points obtained for the emulsion systems studied in the present work, by using the plateau modulus, G_N^0 (corresponding to the values of G' at the plateau) as representative of G' [28]. By this relationship, for a system with a constant dispersed phase volume fraction, such as the ones studied in the present work, G' should be directly proportional to the interfacial tension and inversely proportional to the Sauter mean droplet diameter as seen in Fig 2. 6. I and II. Though the proportionality varies with several other factors, there seems to be a general trend indicating the validity of the above relationship for the emulsions systems studied in the present work.

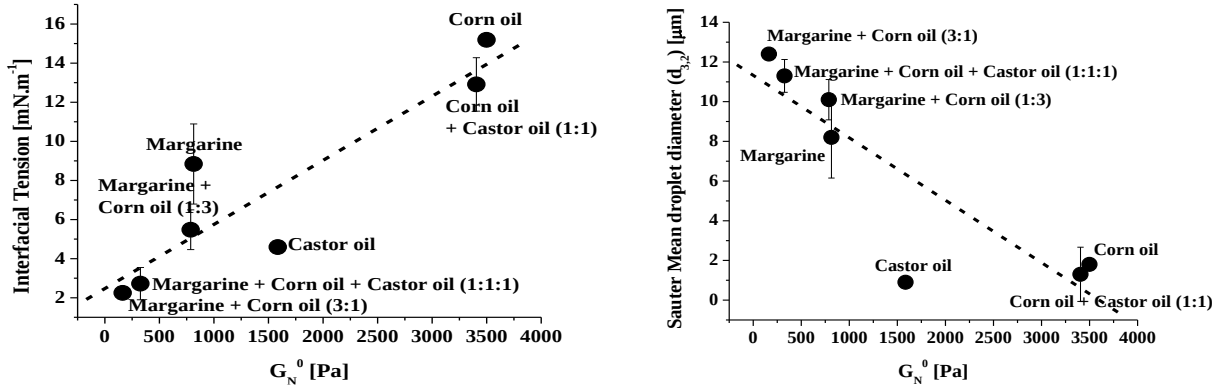

Figure 2.6. I) Interfacial tension vs. plateau modulus II) Sauter mean droplet diameter vs. plateau modulus for the prepared emulsions

Studies were conducted for characterization of the microstructure of the *green bodies* after sintering combining information from SEM (Figs 2. 1 and 2. 2 – 3rd column) and mercury intrusion porosimetry analysis (Figs 2. 7 I and II). According to the SEM images depicted in Fig 2. 1 and 2. 2 all the samples appear to be highly porous with multimodal porosity and pore sizes.

A typical monolithic structure, showing a hierarchical porous networks combining large cavities (formed by the burnout of the oil droplets) with smaller interconnecting pores (formed by the points where the droplets were contacting) was particularly evident for *green bodies* produced from pure corn oil, pure castor oil and the mixture of corn oil + castor oil (1:1).

The samples obtained from margarine containing emulsions (Figs 2. 1- C.3 and Fig 2. 2 - B.3, C.3 and D.3) show dense surfaces with scattered defects corresponding to positions occupied by the larger droplets before sintering. Such structural differences were also confirmed by mercury porosimetry analysis which showed samples with low porosities of 32% (Fig2. 8 I) and a small average pore sizes of 200 nm (Fig 2. 7 II), still amplified by the presence of large cavities (defects). As previously discussed, the use of margarine as a dispersed phase component lead to emulsions

with weak structures, containing fewer droplets in a viscous flowing fluid unable to sustain suspended matter, where the aggregation of alumina particles is likely to occur, explaining the denser structure of the monoliths obtained.

The addition of corn oil as emulsion component led to *green bodies* which appear to have some degree of interconnectivity by minute pores (Fig 2. 1 – A.3, Fig 2. 2 - A.3, B.3, D.3 and E.3), with increased porosities (ranging 40% - 55 %) and average pore sizes, reaching particularly high values (>3 μm) for samples prepared with margarine + corn oil + castor oil emulsions. The impact of corn oil and margarine is also clear by analysis of the pore size distribution (PSD) profiles of the respective monoliths. Most of the monoliths exhibit two well defined bands located in different pore size microscale regions. Monoliths prepared using pure corn oil and margarine present bands located in similar regions with maxima at 0.1 μm and 2 μm, but with different relative predominance in each case (Fig A1. 3 in Appendix). The band at 0.1 μm has higher significance in monoliths prepared using margarine emulsions, which justifies their lower average pore size of 0.2 μm (Fig 2. 7 II). Furthermore, monoliths prepared with emulsions containing both lipids (corn oil and margarine) depict an increase in the dimension of larger pores observed as a shift of the band from 2 μm (for single lipid emulsion) to ~10 μm (for binary lipid emulsions) whereas the band at lower microscale region remains in the same position, with maximum at 0.1-0.2 μm (Figs A1.3 and A1 .4 in Appendix). However, and in contrast to that observed for monoliths prepared with pure corn oil, the contribution of the pore sizes in the smaller microscale is significant, explaining the lower average pore sizes observed for monoliths obtained with margarine + corn oil emulsions (Fig 2. 7 II).

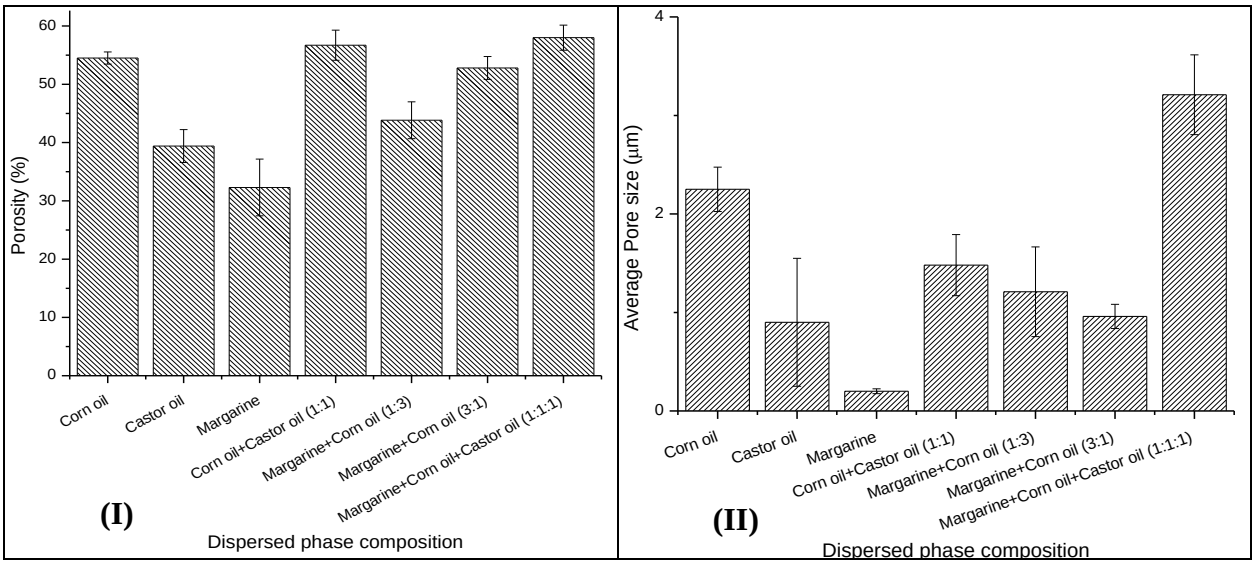

Figure 2.7. I) Values of porosity and II) average pore sizes of the monoliths prepared with different oils, after sintering, measured by mercury intrusion porosimetry

The monoliths obtained with castor oil emulsions also depicted structures with small porosities of 40 % and average pore sizes of ~0.8 µm. In this case, the pore size distribution profile (Fig A1. 3 in Appendix) shows that there is no predominance of pores with a specific pore size, rather a wider distribution of pores sizes between 0.1 µm and 100 µm (with a maximum at 0.8 µm) was observed.

The structural characteristics of these monoliths are associated with the small and highly stable droplet sizes observed in the emulsions obtained with pure castor oil (Table 2. 1). Identical trend is observed for all the *green bodies* produced with other emulsions containing castor oil. Indeed, samples prepared from emulsions with corn and castor oils result in monoliths with high porosities resembling those obtained with pure corn oil but with lower average pore sizes (1.75 µm) caused by the additional droplet size stability due to the presence of castor oil (Table 2.1 1). This effect is also clear by the relative increase of the band of pores sizes at lower microscale, with a maximum at 0.2 µm for monoliths prepared with corn oil + castor oil emulsions (Figs A1. 3 and A1. 4 in Appendix.). However, one should bear in mind that the analysis of porous morphology based on mercury intrusion porosimetry only considers the presence of open pores permeable to Hg, which does not preclude the presence of closed pores in the monoliths. The presence of closed pores is suggested through microscopy images, especially observable for margarine-based emulsions systems (Fig. 2.2 B, C and D). Nevertheless, it is important to note that for most applications, such as those involving fluid flows only through-pores are significant.

Furthermore, correlations between some rheological and morphological properties of the emulsions and the final structural characteristics of monoliths were determined. The plots in Fig. 2. 8 show that the average pore sizes present a proportional tendency towards the interfacial tension between the phases of the emulsion. Also, a linear correlation was found between the pore sizes and the changes of plateau modulus (ΔG_N^0) and the droplet size (Δdp) along storage. These correlations indicate that the average pore size of the monolith increases with the decrease of plateau modulus and with the increase of the droplet size. The observed variations of these parameters are concordant with the presence of droplet coalescence effects with storage. Hence, these correlations confirm that the formation of monoliths with larger pore sizes benefit from conditions that destabilize the emulsions inducing droplet coalescence effects, ultimately leading to the increase of the droplet size with storage.

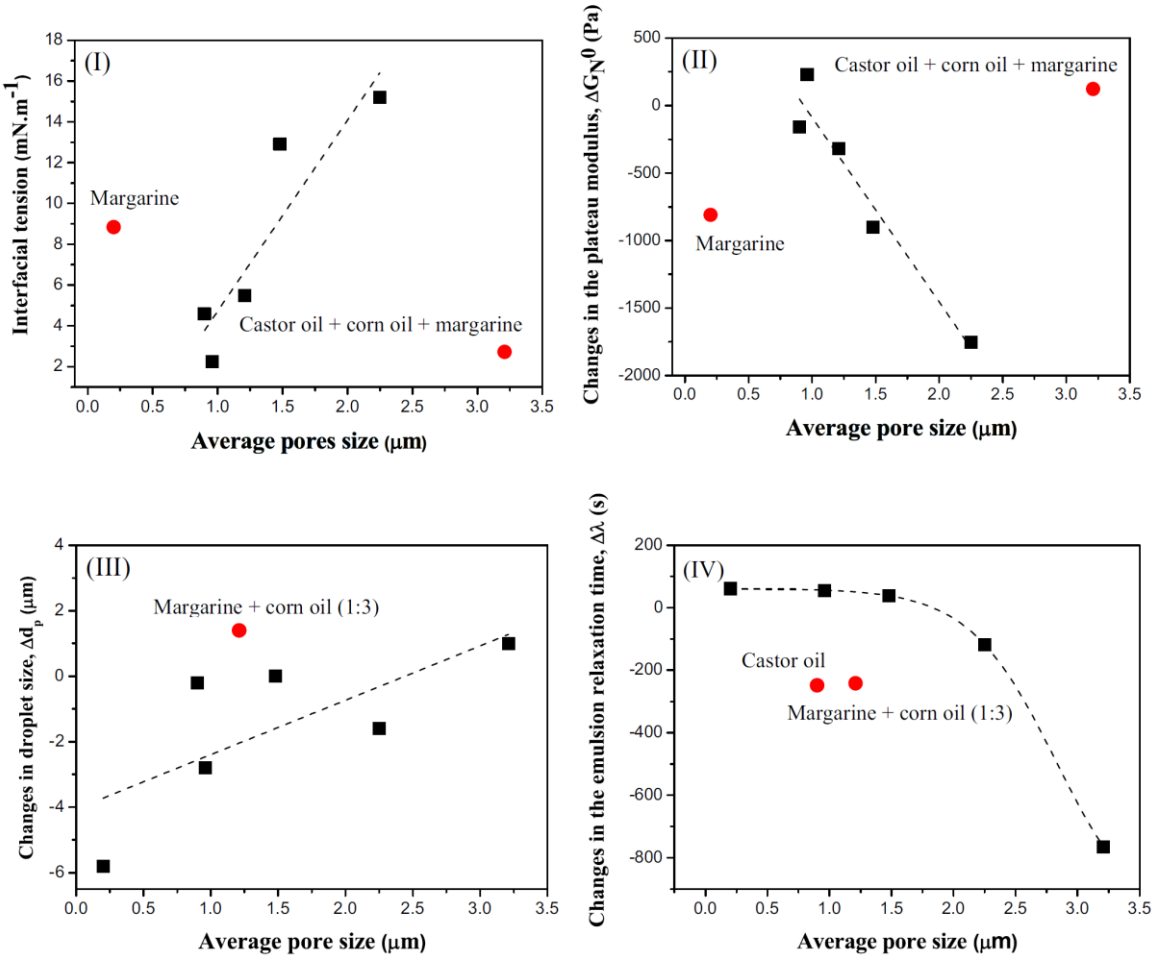

Figure 2.8. Correlation of the average pore sizes of the monoliths with the I) interfacial tension, II) changes in plateau modulus (ΔG_0^N), III) changes in droplet size (Δdp) and IV) changes in the emulsion relaxation time ($\Delta\lambda$) with storage.

In contrast a non-linear correlation was found between the average pore sizes and changes in the emulsion relaxation time (Δλ) with storage. According to the results shown in Fig 2. 8 (IV), the degree of dependence between the average pore size of the monolith and changes of the emulsion relaxation time is insignificant at low pore size range, as expressed by a plateau observed in this region. However, a transition from the steady regime (represented by a plateau at lower pore sizes) to a regime of linear dependency was observed for monoliths with average pore sizes higher than 1.5 μm. The formation of monoliths with higher average pore sizes seems to be associated with the reduction of the emulsion relaxation time with storage. This relation may also be understood from the point of view of the structural characteristics of the emulsion, since a decrease of relaxation time indicates a loss of structural cohesion which is generally associated with an increase of the droplet sizes and thus larger pore sizes.

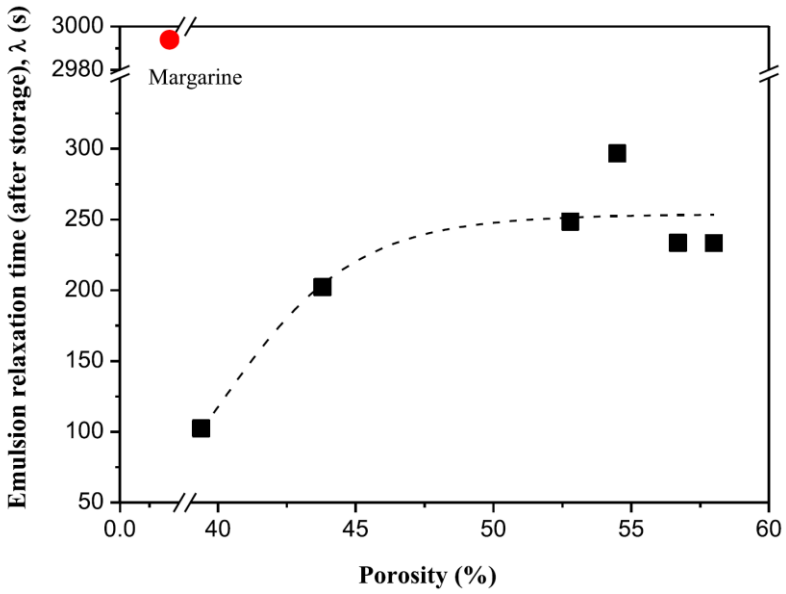

Figure 2.9. Correlation of the relaxation time of the emulsions after storage (72h) with the porosity of the monoliths

Similar analysis was performed aiming to identify possible relationships between the emulsion properties and the monolith porosity. The porosity of monoliths seemed to exhibit a linear dependence with the interfacial tension, with changes of the plateau modulus (ΔG_N^0) with storage period and with the droplet size (Fig. A1. 5. in Appendix). However, in all cases, these correlations are mainly verified for emulsions containing margarine as component of the dispersed phase. The porosity of monoliths produced from emulsions prepared using corn oil and castor oils appear as outliers of these correlations. These results suggest that such correlations do not express a real

dependence of the porosity on these emulsion parameters, but much likely a predominant and consistent effect of margarine on the monoliths structure, yielding monoliths with denser structures and thicker pore walls as observed in SEM images (Fig. 2. 1 E.3, F.3, G.3).

The porosity of the monoliths was found to correlate with the emulsion relaxation time (Fig 2. 8) observed after storage. Similarly, to that observed for the average pore sizes, a non-linear two-step relationship was found between the porosity and the emulsion relaxation time. The porosity of monoliths is positively dependent on the emulsion relaxation time, increasing with the increase of the relaxation time in the low porosity range (up to ~45%), and becomes independent from monolith porosity at values higher than 50%.

Mechanical strength is an important requirement for prospective applications of highly porous monolithic columns. Thus, compressive strength testing was carried out. The corresponding results, shown in Fig 2. 10, are within the range reported for cellular ceramics [7-9, 29, 30].

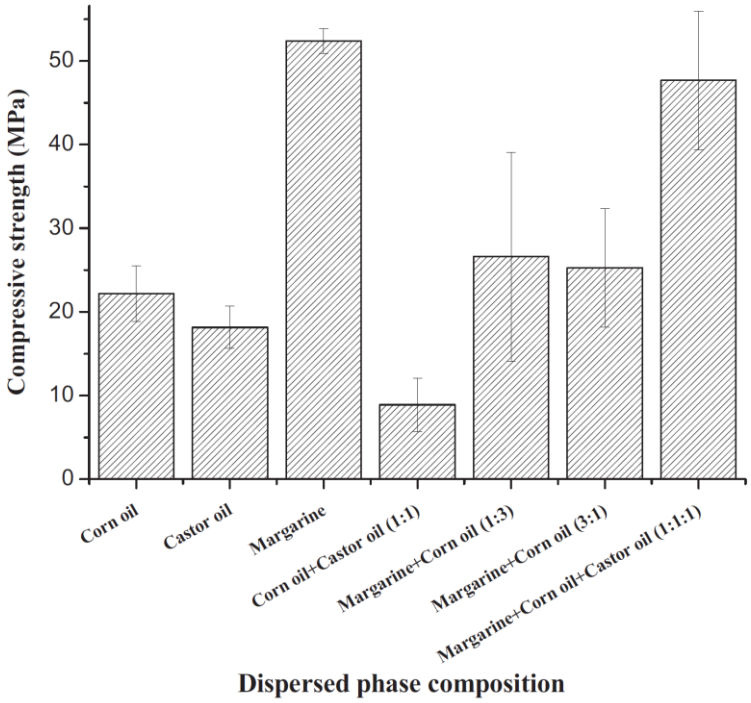

Figure 2.10. Measured compressive strength upon rupture for the monoliths prepared with different oils

The higher the porosity the weaker the column is expected to be. In concordance with this, the monolith columns made with margarine had the highest compressive strength due to a low

porosity. Monolithic columns with higher porosity such as those prepared using emulsions containing castor oil and castor oil + corn oil mixtures showed the weakest compressive strength values. Surprisingly the monolithic columns prepared with emulsions containing margarine + castor oil + corn oil as the dispersed phase showed to have quite a high compressive strength, despite the high porosity. As suggested by the SEM image in Fig. 2.2. D.3, monoliths prepared with margarine + castor oil + corn oil (1:1:1) emulsions seems to combine the multi-modal porosity resulting from the use of castor and corn oils with the high pore wall thickness due to the presence of margarine as an emulsion component, which may explain the high compressive strength shown by these monoliths.

2.4. Conclusions

Mechanically stable and highly porous cellular ceramics can be produced by emulsion gel casting with alumina suspension as the continuous phase and eco-friendly lipids as the dispersed phase, which constitutes a viable alternative to the use of toxic and more expensive dispersed phases, e.g. alkanes. The structural characteristics of the monoliths may be tuned by suitable selection of the lipids (or lipid mixtures) forming the dispersed phase, since they dictate the behaviour of the emulsion-gel along aging (storage period). In this regard, storage and loss moduli (G' and G") and the analysis of their behaviour along storage may provide important insights about droplet coalescence, flocculation and ripening events occurring along emulsion aging and eventually explaining the final microstructure of the sintered green bodies. Emulsions prepared from pure corn and castor oils or a mixture with equivalent weight proportions of these led to *green body* structures resembling the typical monolith morphologies, i.e. high porosities (up to 58%), well interconnected pores and multimodal porous sizes (0.8 μm-2.2 μm). Contrastingly, margarine emulsions led to green bodies with dense structures (low porosities and average pore sizes) and scattered large cavities (defects). Corn oil reduces emulsion stability, prompting more intense droplet coalescence and flocculation effects along aging, leading to the formation of green bodies with a more perceptible hierarchical porous structure, improved porosities and higher average pore sizes. The sintered green bodies produced also depict good mechanical resistance exhibiting compressive strengths in the range of 8 - 50 $N.mm^{-2}$. It is also important to highlight that it is possible to scale up the preparation of monoliths by emulsion-gel casting processes as long as a mixing system with appropriate dimensions is used, along with a proportional increase in the chemical components while maintaining the geometry and aspect ratio of the system. Furthermore, it was demonstrated in this work that some rheological and morphological properties

of the gel-emulsions (i.e. interfacial tension, droplet size, relaxation time and storage modulus) are correlated with monolith structural descriptors, i.e. the average pore size and porosity. The correlations established provide the possibility to anticipate the final microstructural features of the monoliths based on easy measurable emulsion-gel properties. The design of monoliths with fine-tuned morphologies is regarded as an important aspect since it directs the production of porous medium, for chromatography and membrane-based separations, in a way to fulfil the requirements of a wide range of purification processes, privileging the efficiency of separation processes.

References

[1] J. Binner, Ceramic Foams, in: P. Colombo, M. Scheffer (Eds.), Cellular Ceramics: Structure, Manufacturing, Properties and Applications, Wiley-VCH Verlag GmbH, Weinheim, 2005, pp 33-54.

[2] I. Kozo, K. Sridhar, N. Makoto, Porous Materials: Process technology and applications, Springer US, 1998.

[3] P. Colombo, Conventional and novel processing methods for cellular ceramics., Philos. Trans. A. Math. Phys. Eng. Sci. 364 (2006) 109–124.

[4] T. Norby, The promise of protonics, Nature. 410 (2001) 877-878.

[5] X. Wang, J. Li, W. Guan, M. Fu, L. Liu, Emulsion-templated high porosity mullite ceramics with sericite induced textured structures, Mater. Des. 89 (2016) 1041-1047.

[6] R. Moreno, B. Ferrari, Effect of the slurry properties on the homogeneity of alumina deposits obtained by aqueous electrophoretic deposition, Mater. Res. Bull. 35 (2000) 887- 897.

[7] I. Akartuna, A.R. Studart, E. Tervoort, L.J. Gauckler, Macroporous ceramics from particle-stabilized emulsions, Adv. Mater. 20 (2008) 4714–4718.

[8] S. Karaman, M.T. Yilmaz, A. Kayacier, M. Dogan, H. Yetim, Steady shear rheological characteristics of model system meat emulsions: Power law and exponential type models to describe effect of corn oil concentration, J. Food Sci. Technol. 52 (2014) 3851–3858.

[9] B. Yuan, H. Wu, X. Sun, G. Wang, H. Li, Fabrication of porous alumina green bodies from suspension emulsions by gelcasting, Mater. Lett. 81 (2012) 151–154.

[10] M.F. Sanches, N. Vitorino, C. Freitas, J.C.C. Abrantes, J.R. Frade, J.B. Rodrigues Neto, D. Hotza, Cellular ceramics by gelatine gelcasting of emulsified suspensions with sunflower oil, J. Eur. Ceram. Soc. 35 (2015) 2577–2585.

[11] M.F. Sanches, N. Vitorino, J.C.C. Abrantes, J.R. Frade, J.B. Rodrigues Neto, D. Hotza, Effects of processing parameters on cellular ceramics obtained by paraffin emulsified suspensions, Ceram. Int. 40 (2014) 9045–9053.

[12] N. Vitorino, J.C.C. Abrantes, J.R. Frade, Cellular ceramics processed by paraffin emulsified suspensions with collagen consolidation, Mater. Lett. 98 (2013) 120–123.

[13] C. Gallegos, M. Berjano, L. Choplin, Linear viscoelastic behaviour of commercial and model mayonnaise, J. Rheol. (N. Y. N. Y). 36 (1992) 465–478.

[14] A.J. Millán, M.I. Nieto, R. Moreno, C. Baudín, Thermogelling polysaccharides for aqueous gelcasting - Part I: A comparative study of gelling additives, J. Eur. Ceram. Soc. 22 (2002) 2209–2215.

[15] P. Bednarek, M. Szafran, Y. Sakka, T. Mizerski, Gelcasting of alumina with a new monomer synthesized from glucose, J. Eur. Ceram. Soc. 30 (2010) 1795–1801.

[16] P. Sepulveda, J.G. Binner, Processing of cellular ceramics by foaming and in situ polymerisation of organic monomers, J. Eur. Ceram. Soc. 19 (1999) 2059–2066.

[17] Y. Chen, Z. Xie, J. Yang, Y. Huang, Alumina casting based on gelation of gelatine, J. Eur. Ceram. Soc. 19 (1999) 271–275.

[18] Z.P. Xie, J.L. Yang, D. Huang, Y.L. Chen, Y. Huang, Gelation forming of ceramic compacts using agarose, Br. Ceram. Trans. 98 (1999) 58–61.

[19] S. Dhara, P. Bhargava, Egg White as an Environmentally Friendly Low-Cost Binder for Gelcasting of Ceramics, J. Am. Ceram. Soc. 84 (2001) 3048–3050.

[20] M. A Janney, O.O. Omatete, C. a Walls, S.D. Nunn, R.J. Ogle, Development of Low-Toxicity Gelcasting Systems, J. Am. Ceram. Soc. 91 (1998) 581–591.

[21] P.J. Carreau, Rheological Equations from Molecular Network Theories, Trans. Soc. Rheol. 16 (1972) 99–127.

[22] J. Schindelin, I. Arganda-Carreras, E. Frise, V. Kaynig, M. Longair, T. Pietzsch, S. Preibisch, C. Rueden, S. Saalfeld, B. Schmid, J.Y. Tinevez, D.J. White, V. Hartenstein, K. Eliceiri, P. Tomancak, A. Cardona, Fiji: An opensource platform for biological-image analysis, Nat. Methods. 9 (2012) 676–682.

[23] T. Tadros, Application of rheology for assessment and prediction of the long-term physical stability of emulsions, Adv. Colloid Interface Sci. 108-109 (2004) 227-258.

[24] A. Romero, F. Cordobés, M.C. Puppo, A. Guerrero, C. Bengoechea, Rheology and droplet size distribution of emulsions stabilized by crayfish flour, Food Hydrocoll. 22 (2008) 1033–1043.

[25] E. Dickinson, Food colloids - An overview, Colloids Surf. 42 (1989) 191–204.

[26] A.M. Grillet, N.B. Wyatt, L.M. Gloe, Polymer Gel Rheology and Adhesion, in: J. De Vicente (Ed.), Rheology, InTech, London, UK, 2012, pp 59-80.

[27] H.M. Princen, Rheology of foams and highly concentrated emulsions. I. Elastic properties and yield stress of a cylindrical model system, J. Colloid Interface Sci. 91 (1983) 160–175.

[28] S. Wu, Chain structure and entaglement, J. Polym. Sci. Part B Polym. Phys. 27 (1989) 723–741.

[29] M. Potoczek, Gelcasting of alumina foams using agarose solutions, Ceram. Int. 34 (2008) 661–667.

[30] U.T. Gonzenbach, A.R. Studart, D. Steinlin, E. Tervoort, L.J. Gauckler, Processing of particle-stabilized wet foams into porous ceramics, J. Am. Ceram. Soc. 90 (2007) 3407–14.

CHAPTER 3

CFD MODELLING OF FLOW PATTERNS, TORTUOSITY AND RESIDENCE TIME DISTRIBUTION IN MONOLITHIC POROUS COLUMNS RECONSTRUCTED FROM X-RAY TOMOGRAPHY DATA

Published as: *S. Pawlowski, N. Nayak[#], M. Meireles, C.A.M. Portugal, S. Velizarov, J.G. Crespo, CFD modelling of flow patterns, tortuosity and residence time distribution in monolithic porous columns reconstructed from X-ray tomography data, Chem. Eng. J. (2018). doi:10.1016/j.cej.2018.06.017.*

[#]Contributed towards development of the monolith, acquisition and digital reconstruction of X-Ray μ-Tomography data while on Erasmus Mundus mobility at Université Paul Sabatier, Toulouse. FR.

Abstract

Highly porous monolithic alumina columns find a wide variety of applications, including in chromatography, due to increased surface area and good accessibility to the ligands and reduced diffusional hindrances. Several modelling approaches have been applied to describe experimentally observed flow behaviour in such materials, which morphology plays a key role in determining their hydrodynamic and mass transfer properties. In this work, a direct computational fluid dynamics (CFD) modelling approach is proposed to simulate flow behaviour in monolithic porous columns. The morphological structure of a fabricated alumina monolith was first reconstructed using 3D X-ray tomography data and, subsequently, OpenFOAM, an open-source CFD tool, was used to simulate the essential parameters for monoliths' performance characterisation and optimisation, i.e. velocity and pressure fields, fluid streamlines, shear stress and residence time distribution (RTD). Moreover, the tortuosity of the monolith was estimated by a novel method, using the computed streamlines, and its value (~1.1) was found to be in the same range of the results obtained by known experimental, analytical and numerical equations. Besides, it was observed (for the case of the monolith studied) that fluid transport was dominated by flow heterogeneities and advection, while the shear stress at pore mouths was significantly higher than in other regions. The proposed modelling approach, with expected high potential for designing target materials, was successfully validated by an experimentally obtained residence time distribution (RTD).

3.1. Introduction

Porous ceramics find applications in a wide variety of areas, such as molten or gas stream filters [1], tissue culture scaffolds [2], solid oxide fuel cell components and chromatographic stationary phases [3] due to a combination of favourable properties, like a relatively low thermal conductivity, low density, high porosity and high chemical resistance [4]. Monolithic stationary phases prepared from ceramic materials like alumina or porous silica could be an effective alternative to particulate beds as they allow for a higher permeability, due to their high porosity (0.6-0.8) and large and easily modifiable through-pore size/skeleton size ratios [4–9]. Monolithic columns present a hierarchical structure with an intertwined network of through-pores (2–8 μm diameter) enabling easy convective transport, while also providing a mesoporous intra-skeleton structure (1–2 μm diameter) with a large functionalizable surface area accessible by diffusion [9,10].

The monolith morphology plays a key role in determining its hydrodynamic and mass transfer properties [10]. The microporous structure governs the fluid flow dynamics and associated fluid dispersion [11], whereas the intra-skeleton mesoporous structure determines the mass transfer resistance and diffusion mechanisms (bulk and/or surface diffusion; Knudsen diffusion, etc.) [11]. The heterogeneity of the microporous space, variable thickness of the skeleton wall and/or border layer trans-column eddy dispersion effects lead to flow velocity bias at various scales and a consequent fluid dispersion [12,13]. Therefore, the separation process efficiency is related with the width of the residence time distribution (RTD) curve, which is influenced by the mobile phase velocity and the monolith morphology [11]. A narrow residence time distribution and a small band broadening are desirable, since this means small hydrodynamic dispersion and fast mass transfer into and out of the porous media [11].

To visualise and gain better knowledge about the internal structure of a monolith, most of the reported studies involve the use of scanning electron microscopy (SEM) [14–19] or confocal laser scanning microscopy (CLSM) [20–28], wherein dyes are used to stain the samples and obtain images through the depth of the sample. In such a way, a number of 2D image slices are obtained, which are used to construct a 3D virtual structure of the monolith and to perform a quantitative morphological image analysis. Such reconstructed structures were also used for simulation of flow profiles and dispersion within monoliths by the Lattice-Boltzmann method (LBM), allowing to correlate their morphological properties, by calculating the Darcy permeability, fluid velocities dispersion/distribution, pressure gradient and plate height [16,22–26]. Recently, a commercial computational fluid dynamics (CFD) tool, Starccm+, was used to calculate velocity fields, streamlines, pressure drop and permeability in a polymethacrylate-based monolith reconstructed from 898 image slices, of 50 nm each, acquired by SEM [18]. The images resolution was 1024 x 1024 pixels (pixel size 98 nm) and the reconstructed cubic block had an edge length of 45 µm. The choice of the column region to perform simulations is puzzling since the monolith may present internal differences between regions which are created during the manufacturing process [29].

X-ray tomography (where the actual 3D object is reconstructed from 2D images acquired at different angles of the sample [30]) has been used so far to access the morphology of packed bed chromatography columns, analyse their porosity, tortuosity and identify axial and radial morphologic heterogeneity [31]. In a similar way, X-ray tomography was used to reconstruct the arrangement of slurry electrodes and visualise percolation pathways [32] and to obtain accurate representations of a spacer filament shape, used later to perform CFD simulations [30]. CFD

simulations using X-ray tomography images were found to be close to experimentally obtained results, indicating that the images obtained are suitable to approximate real feed-side spacer geometries [30].

In this work, an open source CFD software, OpenFOAM (https://openfoam.org/), was used to simulate the flow behaviour and hydraulic dispersion in an alumina monolithic column. The 3D morphology of the monolith was reconstructed using X-ray tomography. Velocity, pressure, shear stress (especially important in protein separations [33]) and the monolith column tortuosity were estimated. The tortuosity was directly assessed by measuring lengths of the streamlines which, in laminar regime and steady state, represent the actual fluid pathways. Moreover, the residence time distribution (RTD) was also simulated and experimentally successfully validated. To test the reproducibility of the simulations, they were performed in two different sub volumes. The modelling approach presented in this work can be useful for designing porous monolith columns by providing a number of straightforward parameters describing their performance.

3.2. Materials and methods

Alumina monolithic columns prepared as described elsewhere [8] were characterised in terms of their porosity, residence time distribution (RTD) and internal morphology. A detailed description of the monolith preparation method can be found in Supplementary Material. The internal morphology was assessed by X-ray tomography, which images were used further for a 3D virtual reconstruction of the column. CFD simulations (the core of this work), aiming at prediction of velocity, pressure, shear stress, tortuosity and residence time distribution, were performed in two sub volumes (with average edge length of 107 and 142 μm, respectively) of the virtually reconstructed column. Fig 31 shows the flow chart describing the steps followed from the column characterisation to the modelling approach validation.

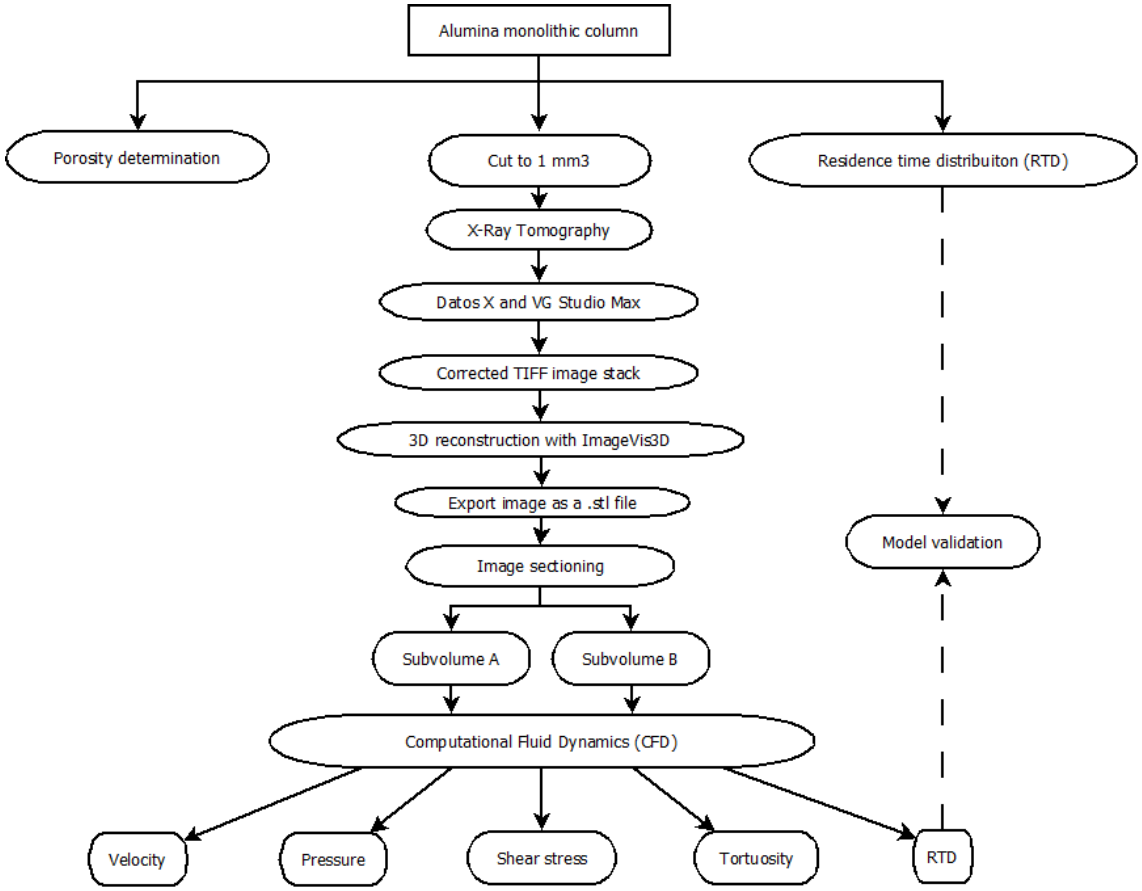

Figure 3.1. A flow chart of the steps followed from column characterisation to modelling approach validation

3.2.1. Porosity determination

The total void volume or gross porosity was measured as follows:

$$\varphi = \frac{V_V}{V_T} \qquad (1),$$

where φ is the porosity, V_V is the volume of the void space and V_T is the total or bulk volume. The void volume in this case was determined as the difference between the volumes occupied by the sintered whole monolith and the by its particles when it was crushed.

3.2.2. Residence time distribution (RTD)

A pulse input of 0.13 g of pure acetone was injected at the inlet of a 2 cm long piece of a previously prepared monolithic column attached to a piston pump, which provided a constant eluate (de-

ionised water) flow rate of 0.27 cm^3/min. Acetone was selected as a tracer due to its negligible chemical interaction with the monolith surface. The eluted samples were collected for 28 minutes, in individual tubes using a fraction collector at a tube switching frequency of 90 seconds. The acetone elution from the monolithic column was followed by UV-Vis analysis using a spectrophotometer Evolution 200, Thermo Unicam, at an absorbance wavelength of 260 nm. The absorbance results along the elution time (t) were used to determine the acetone throughput (C_t) and the dimensionless residence time distribution ($E(\theta)$) in the monolithic column as described in the following equations [34]:

$$E(t) = \frac{C_t}{\int_0^\infty C_t dt} \quad (2),$$

$$\bar{t} = \frac{\int_0^\infty t C_t dt}{\int_0^\infty C_t dt} \quad (3),$$

$$\theta = \frac{t}{\bar{t}} \quad (4),$$

$$E(\theta) = \bar{t} E(t) \quad (5),$$

where $\bar{t}$ is the mean residence time, θ is the dimensionless time and $E(t)$ is the tracer residence time distribution.

3.2.3. X-Ray tomography

X-ray tomography was performed on a ~1 mm^3 sample with the Phoenix/GE Nanotom 180 using a Tungsten target from the Research Federation FERMaT (FR3089) based in Toulouse, France. A cone shape X-ray beam with energy of 80 KeV was transmitted and produced 1440 images as the specimen underwent a 360° rotation (1.7 um/voxel). The stack of images was constructed using Datos X (Pheonix X-ray system) and VG Studio Max (Volume Graphic GmbH, Germany). The total recording time was 4 h 47 minutes.

3.2.4. 3D virtual reconstruction of the column morphology

3D image reconstruction and conversion to STL format

ImageVis3D was used to reconstruct the 3D geometry of the column from the stack of 2D images. The image stack of 1440 images in TIFF format was imported into ImageVis3D v. 3.1.0 and noise

was removed. The improved 3D image was then exported as an STL file with a resolution of 520x520x520 pixels/cm suitable for mesh grid creation and use in the CFD simulation studies.

Mesh generation

From the reconstructed 1 mm^3 monolith, two different randomly selected sub volumes, with the dimensions summarised in Table 3. 1, were virtually cut out using Autodesk Meshmixer, v. 3.2.37, software, in order to create a computational mesh to be used in the CFD simulations.

Table 3.1. Dimensions and porosities of monolithic subvolumes A and B used for CFD simulations.

Sub volume	A	B
Dimensions (μm)	86x98x144	142x134x150
Porosity (-)	0.809	0.837

The computational mesh of the selected monolith sub volumes was created using the Salome v. 7.8.0 software (http://www.salome-platform.org/) and the snappyHexMesh OpenFOAM grid generation utility (https://cfd.direct/openfoam/user-guide/snappyhexmesh/). Salome was used to create a box around the selected sub volumes with its faces 2 μm apart from the skeleton. The monolith skeleton was cut out from the created box in order to define a computational domain through which the fluid flows. The computational domain obtained was checked for illegal intersections which, if present, were corrected by the intrinsic repair operators of Salome. The bottom, upper and lateral faces of the box were defined as inlet, outlet and walls, respectively, while the resulting interior was referred to as skeleton. A 2D Mefisto algorithm was applied to all (the exterior and interior) faces to create uniform triangulations at their surfaces, to facilitate the generation of the final computational mesh by the snappyHexMesh utility from the respective stl. files containing the geometry of the faces. The snappyHexMesh utility was used to refine the grid near the boundaries in order to accurately resolve the boundary conditions. A preliminary mesh independence study was performed to select the appropriate mesh for each case.

3.2.5. Computational fluid dynamics (CFD) simulations

Strategy

The open source OpenFOAM software package, version 5.0 (http://www.openfoam.org), was used to simulate the flow patterns of a single-phase incompressible laminar flow of a Newtonian fluid (water) in 3D image reconstructions of the monolithic porous column sub volumes under study. Subsequently, using the previously obtained velocity profiles, a pulse injection of the tracer (acetone) was simulated and its concentration at the outlet was followed in order to obtain the residence time distribution (RTD) curve. The simulations were performed in two sub volumes (Table 3.2 1) since with current methods of fabrication, random pore size distributions and flow velocity inequalities at various scales may occur [6][26][29], thus it is important to test the replicability of the results.

Modelling methodology

The governing equations for the CFD simulations performed were the mass continuity and Navier-Stokes equations define as follows [35,36]:

$$\nabla \boldsymbol{U} = 0 \qquad (6),$$

$$\frac{\partial \rho U}{\partial t} + (u \cdot \nabla)\rho \boldsymbol{U} - \nabla \cdot (\mu \nabla \boldsymbol{U}) = -\nabla p \qquad (7),$$

with $\boldsymbol{U}$ being the fluid velocity vector, ρ the fluid density, μ the dynamic viscosity and p the pressure. These equations were solved by the SIMPLE (semi-implicit method for pressure-linked equations) algorithm using 8000 iterations to grant numerical stability (steady state) of the velocity and pressure fields. In turbulence Properties foam file, the *simulationType* was chosen to be laminar and the inertial forces were neglected (creeping flow regime), which is an acceptable assumption for Reynolds number values below 100 [37].

Velocity fields were solved with preconditioned biconjugate gradient (PBiCG) solver, diagonal-incomplete LU (DILU) preconditioner, tolerance of 10^{-5} and relTol of 0.1. For pressure, a generalised geometric-algebraic multi-grid (GAMG) solver with 10 cells in coarsest level, GaussSeidel smoother, tolerance of 10^{-6} and relTol of 0.01was used. Relaxation factors have

been set to 0.3 for the pressure field and 0.7 for the velocity. The choice of the above-mentioned parameters resulted from preliminary studies, in which computational time and residuals values had been compared.

After obtaining the flow fields at steady state, the tracer concentration time variation was simulated with the scalarTransportFoam solver, which resolves a transport equation (eq. 8) for a passive scalar [38]:

$$\frac{\partial C_t}{\partial t} + \nabla \cdot (\boldsymbol{U} C_t) - \nabla^2 (\nu C_t) = 0 \qquad (8),$$

where C_t is the tracer concentration, v is the kinematic viscosity of the tracer, t is the time and $\boldsymbol{U}$ is the previously obtained stationary velocity field. Acetone properties were used as the tracer physical properties, and the method of pulse input injection was implemented by choosing for the tracer, at the inlet, a *fixedValue* boundary condition with a value of 1 during the initial 0.0005 seconds (which is the time of pulse injection) and a value of 0 until the end of the simulation equal to 10 seconds. The tracer concentration field was solved with the preconditioned biconjugate gradient (PBiCG) solver, diagonal-incomplete LU (DILU) preconditioner, tolerance of 10^{-6} and relTol of 0.

The remaining boundary conditions and numerical schemes used in the CFD simulations are detailed in Table 3. 2.

Table 3.2. Numerical methods and boundary conditions for CFD simulations

Solver	Operator	Method
simpleFoam	time derivative	steadyState
	gradient	Gauss linear
	divergence	bounded Gauss limitedLinear 1
	Laplacian	Gauss linear corrected
scalarTransportFoam	time derivative	Euler
	gradient	Gauss linear
	divergence	Gauss limitedLinear 1
	Laplacian	Gauss linear corrected

Variable	Boundary	Condition
velocity	inlet	fixedValue (uniform 0 0 u)
	outlet	inletOutlet (uniform 0 0 0)
	walls	slip
	skeleton	fixedValue (uniform 0 0 0)
pressure	inlet	zeroGradient
	outlet	fixedValue (uniform 0)
	walls	zeroGradient
	skeleton	zeroGradient
concentration (tracer)	inlet	fixedValue (uniform 1 or 0)
	outlet	zeroGradient
	walls	zeroGradient
	skeleton	zeroGradient

Data post-treatment

The post-treatment of the CFD results obtained was performed using ParaView 5.3.0 (https://www.paraview.org/). The streamlines were calculated by Stream Tracer functionality from the previously obtained velocity vectors. The tortuosity ( ) of the fluid pathways was calculated as follows:

$$\tau_i = \frac{L_i}{C_i} \qquad (9),$$

where *L* is the length of a streamline *i* and *C* is the distance between the ends of a streamline *i*. The distribution of the tortuosity in simulated sub volumes A and B, was obtained using 155 randomly generated streamlines. From these results, an arithmetic average value of tortuosity was calculated for both sub volumes. The shear stress around the alumina skeleton was computed using OpenFOAM function object wallShearStress. Finally, the dimensionless residence time distribution ($E(\theta)$) curves were calculated along time (t) by using the average concentration of the tracer at the outlet (C_t) of the simulated computational domains as described in equations 1-4. These computational RTD results were compared with the experimentally obtained data in order to validate the modelling approach.

3.3. Results and discussion

3.3.1. Alumina monoliths

The alumina monoliths obtained have a hierarchical morphology with the oil droplets forming the macroporous structure, and the interfaces between the coalesced drops forming the inter-connecting channels. The porosity of the monolithic sample was determined to be 0.76. Fig 3. 2 shows the alumina monolith sample reconstructed from these images and saved as a .stl file.

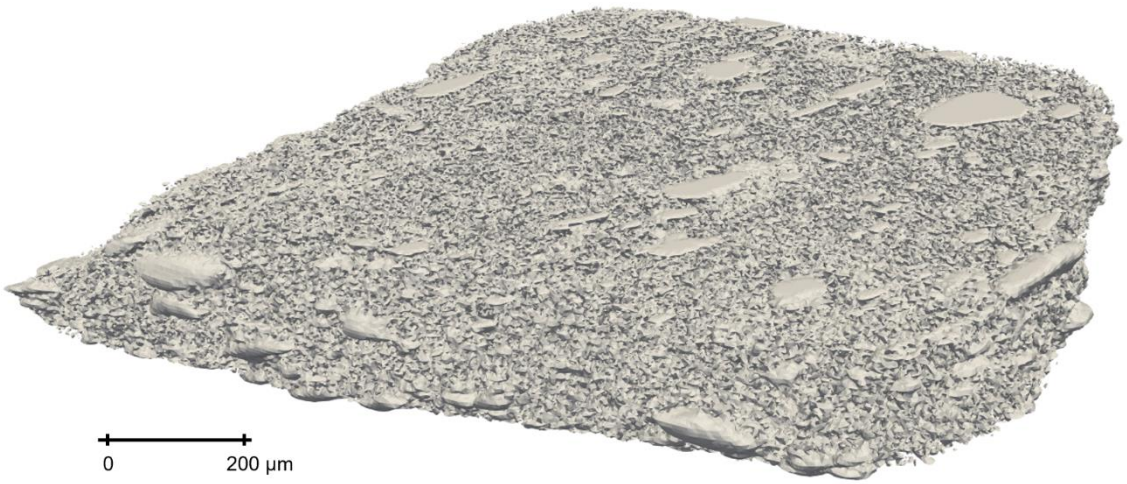

Figure 3.2. 3D virtual reconstruction of alumina monolith from X-ray tomography images

It is possible to observe a highly porous structure and interspersed dense areas, which comprise the “crystalline zones” and appear as solid impervious fragments. Since CFD simulations for the entire volume block of 1 mm^3 would require extremely high amount of computing power, two smaller arbitrary finite sub volumes (of $1.21*10^{-3}$ mm^3 and $2.85*10^{-3}$ mm^3 respectively) were considered from the original volume. These sub volumes, A and B, are shown in Fig 3. 3.

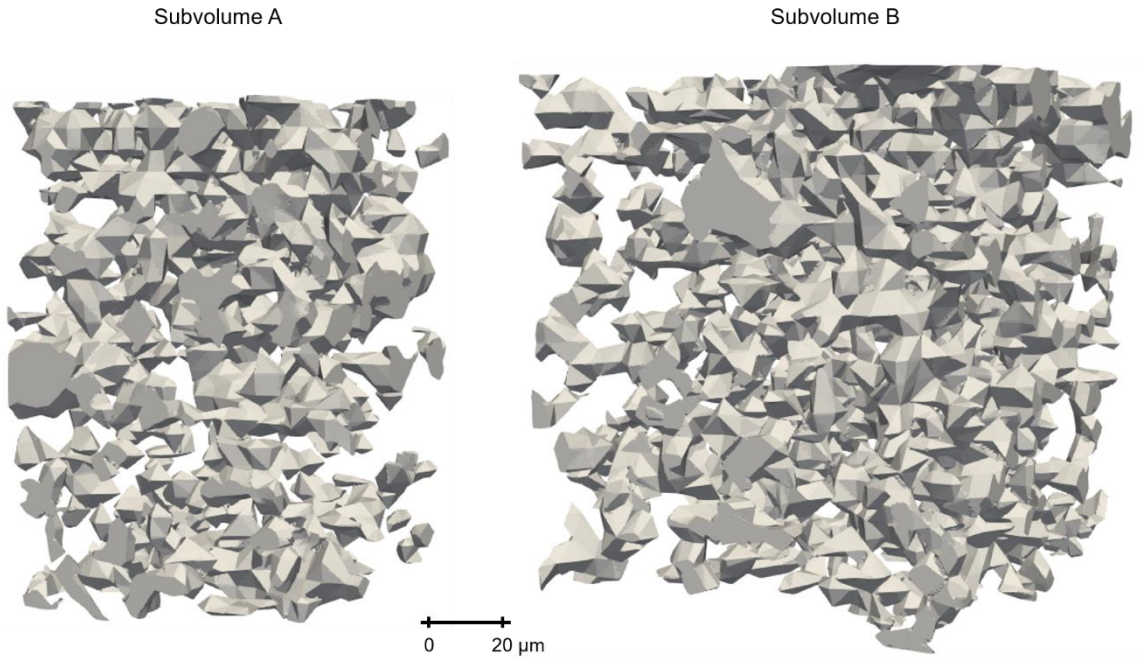

Figure 3.3. Subvolumes of the 3D virtual reconstruction of the monolith with porosities of A = 0.809 and B = 0.837 used for CFD simulations

Sub volumes A and B are represented at the same scale in Fig 3. 3. Sub volume B has a 2.35 larger volume than that of sub volume A. Sub volumes A and B exhibit similar porosities, 0.809 and 0.837, respectively.

3.3.2. Computational fluid dynamics (CFD) simulations

The CFD simulations, and the applied methodology were validated by comparing the computational and an experimentally obtained residence time distribution. In the CFD simulations performed, the linear flow velocity (*u*) at the inlet was the same as used in the experimental study ($5.97_{*}10^{-5}$ m/s, which corresponds to an experimental flow rate of 0.27 ml/min). From the fields obtained, it was possible to calculate fluid streamlines, the tortuosity, the shear stress and the residence time distribution (RTD). The CFD results obtained are presented for sub volume A, while the ones obtained for sub volume B can be found in Supplementary material.

Flow behaviour

Fig 3. 4 shows the computational domain of sub volume A, which includes the monolith skeleton and the void spaces, through which the fluid can flow.

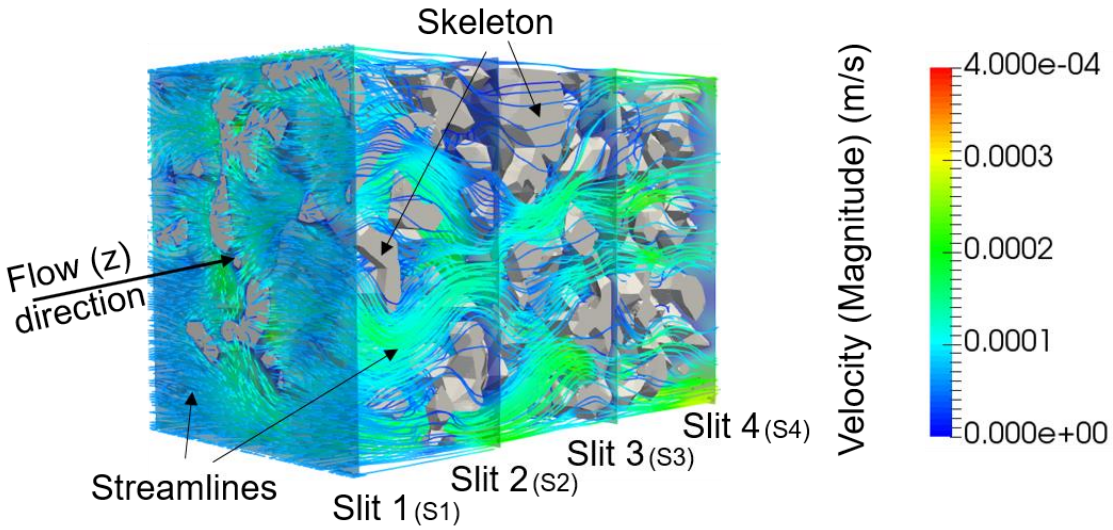

Figure 3.4. Representation of streamlines (fluid pathways) in subvolume A of the 3D virtually reconstructed monolith

The displayed streamlines (since obtained at laminar regime and steady state) show the pathways that the fluid "packages" travel while moving through the monolith. It is important to notice that movement does not occur at constant velocity along a streamline. All streamlines depart from the inlet and, as can be seen, they are not straight lines and deviate from the obstacles (skeleton) in their path from inlet to outlet. The geometry/shape of the streamlines provides information about the monolith tortuosity, which is discussed in the next section. Fig 3. 4 also shows the location of the slits showing velocity (Fig 3. 5a), pressure (Fig 3. 5b) and shear stress (Fig 3. 5c) fields, respectively. For the sake of clarity, only four slits are shown, but they can be generated in any number and position. The slits shown were chosen to be equidistant, with the first slit located at the pores' mouth (where the skeleton begins) and the last, fourth slit, located where the skeleton ends.

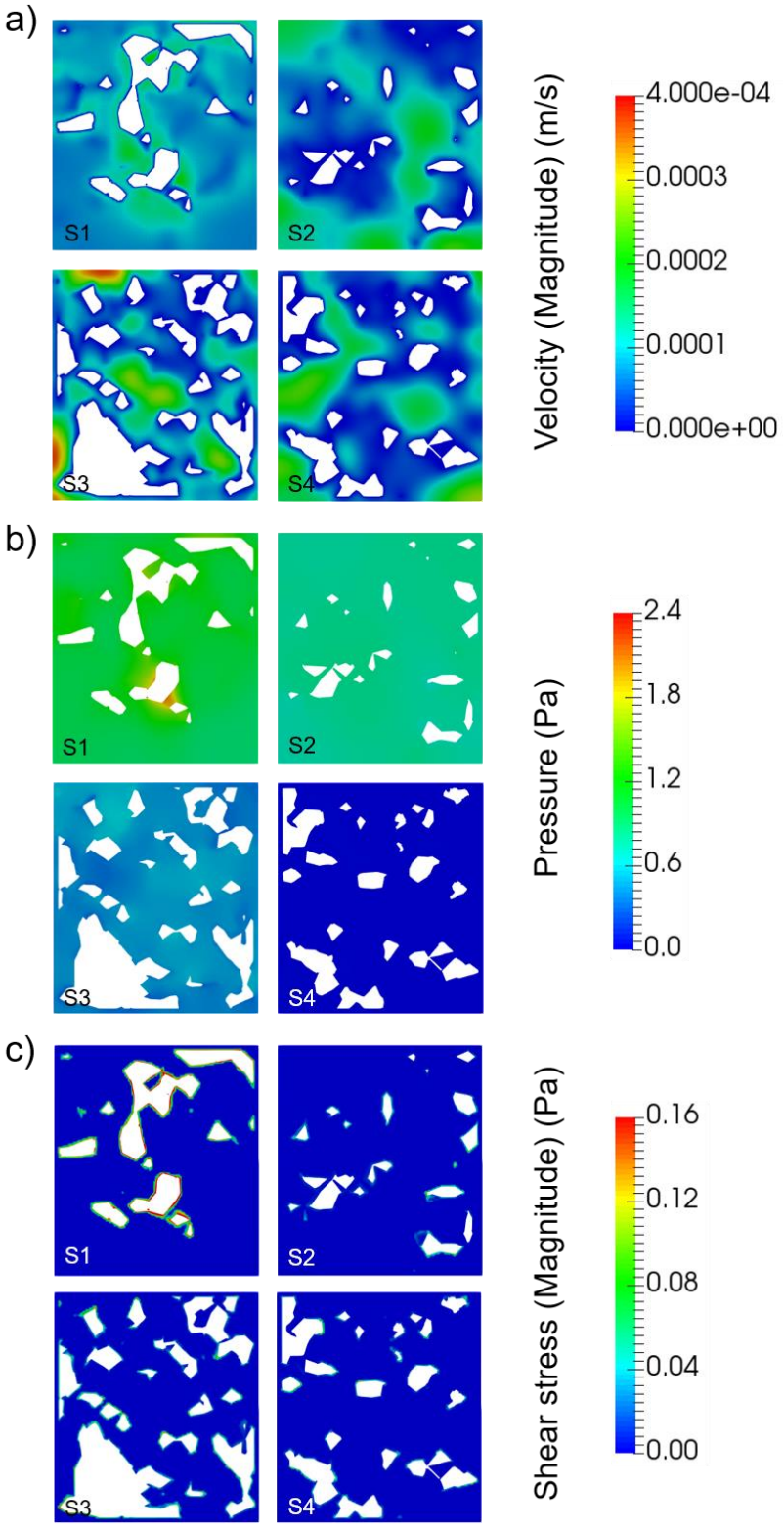

Figure 3.5. CFD results obtained in subvolume A, showing slits S1, S2, S3 and S4 with information about computed a) velocity, b) pressure and c) shear stress. The white regions are the skeleton

In Fig 3. 5a it is possible to see that there are differences in the fluid velocity distribution at the given z-plane (slit) of the monolith, while along the flow axis the velocity is almost constant and its distribution is only affected by presence or obstructions due to the shape of the skeleton. Therefore, there are widely open regions with high velocity (if, for example, the skeletal obstruction is located around that region, and therefore the flow is preferentially directed through that region), as well as less open regions, with a lower fluid velocity, if there is an obstruction immediately before or after. Therefore, it is important to visualise the velocity distribution in a 3D way. The local velocity is usually higher than the inlet velocity, since the fluid flow accelerates when entering a porous structure, for which there are clear flow heterogeneities. Such flow heterogeneities affect the shape of the residence time distribution (RTD) curves.

Regarding the pressure (Fig 3. 5b), it can be observed that it gradually decreases along the simulated monolith (pressure drop) but is almost constant at the given z-plane (slit). The average pressure drop (at linear flow velocity of $5.97*10^{-5}$ m/s) was 7.96 kPa/m in sub volume A and 5.83 kPa/m in sub volume B. The higher average pressure drop found for sub volume A may have resulted from the lower porosity of that sub volume [39].

The shear stress at the vicinity of the skeleton (Fig 3. 5c) is very similar at all simulated monolith volumes, except for the zone located near the inlet (slit 1), at the pore mouth, where it more than four times higher. This can be attributed to pore and flow entrance effects [40,41], as the flow moves from a void space region to a volume partially occupied by skeleton, thus causing a sudden increase of the local linear flow velocity.

Tortuosity

The use of a Paraview visualisation tool allows to calculate the length of each streamline, as well as the shortest distance between each streamline' beginning and end. Knowing these two values, it becomes possible to estimate the tortuosity. Tortuosity of a porous medium can be estimated based on its geometric tortuosity extrapolated from its geodesic reconstruction or it can be derived from diffusion coefficients and empiric equations [14,42–44]. The geometric tortuosity presents lower values than diffusive (or any other mass-transport related) tortuosity, as it reflects an ideal route [44]. The herein proposed method is different from previous methods, as it is based on the actual fluid pathway, accessed straightforwardly by the computed streamlines. Fig 3. 6 shows the

obtained histograms of tortuosity calculated for sub volumes A and B, using 155 streamlines in each case.

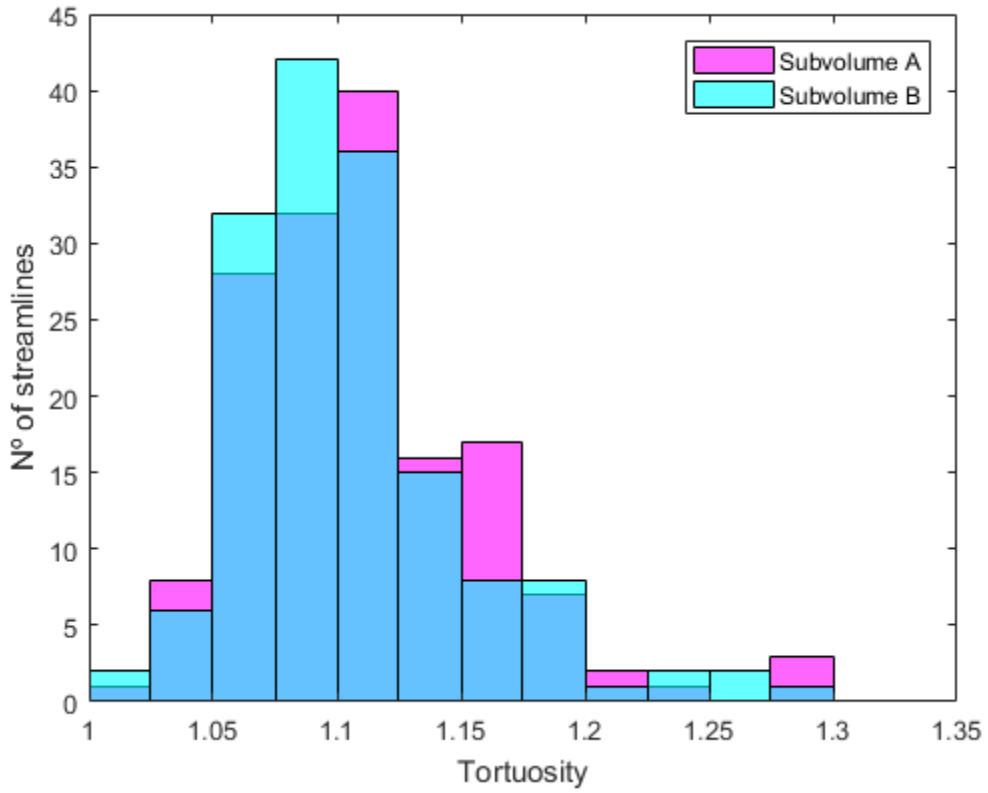

Figure 3.6. Histograms of tortuosity obtained in subvolumes A and B of the 3D virtually reconstructed monolith

It is possible to see in Fig 3. 6 that the tortuosity values obtained from the streamlines are within the range between 1 and 1.3. The histogram for both sub volumes have similar appearances and the highest number of occurrences lies within the range between 1.050 and 1.125. The histograms obtained show a resemblance with geometric tortuosity of a silica monolith calculated from SEM images [14], although the obtained values are shifted towards 1, as the herein investigated structure is more open. The mean tortuosity values are practically the same for both sub volumes being equal to 1.110 and 1.106, for sub volume A and B, respectively (Table 3. 3).

Table 3.3. Comparison between mean tortuosity computed by the approach used in this work and tortuosity values obtained using models available in the literature

Model (Reference)	Condition (Method)	Sub volume A	Sub volume B
This work	Monolith (CFD/Streamlines)	1.110	1.106
$\tau = 1 - 0.49 \ln \varepsilon$ ([45])	Bed of spheres (Experimental)	1.104	1.087
$\tau = \frac{1}{\varepsilon^{0.33}}$ ([46])	Granular packings (Analytical)	1.072	1.060
$\tau = 1 + 0.64(1 - \varepsilon)$ ([47])	Spherical particles (Numerical)	1.122	1.104

As shown in Table 3, the experimental, analytical and numerical equations, describing systems comprised of spherical particles, relate tortuosity to porosity (ε). Since the monoliths with a nonporous skeleton or an inaccessible intraskeletal pore network resemble beds of nonporous spheres [48], the values of tortuosity obtained by herein presented method are very similar to these calculated by the known models, which validates the approach developed in this work.

Residence time distribution (RTD) & Validation of the modelling approach

Based on the velocity field obtained at steady state, the injection of a tracer (acetone) into sub volumes A and B was simulated. Fig 3. 7 shows the tracer concentration (normalised by the tracer input concentration) along time (normalised by mean time residence) at the outlet of sub volume A.

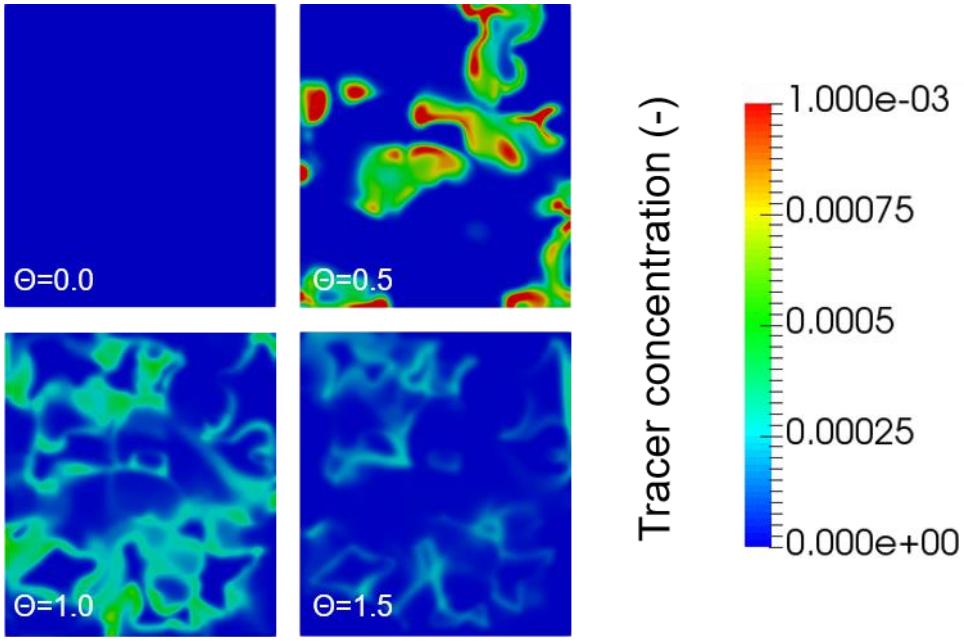

Figure 3.7. Local dimensionless tracer concentration at the outlet of subvolume A along time (normalised by mean time residence)

When performing a residence time distribution (RTD) analysis of the data obtained, time is normalised by the mean residence time, which means that for example at Θ=1, half of the injected tracer amount had already left the computational domain. In such a way, for example, it is possible to see that at Θ=0.5 the tracer concentration leaving the monolith was higher than that at Θ=0, 1.0 and 1.5. Videos (Sub volume A.ogv and Sub volume B.ogv) illustrating these simulations are available in Supplementary material. These videos show the motion and dispersion of the tracer (acetone) through the 3D computed domains upon a pulse tracer injection. Additionally, the instantaneous concentration of the tracer at the outlet and at three equidistant y-plane slits, which are parallel to the main flow direction, is also displayed in the videos.

Fig. 3. 8 shows the residence time distribution (RTD) curves obtained by the CFD modelling approach for the investigated sub volumes A and B, as well as the experimentally determined RTD points.

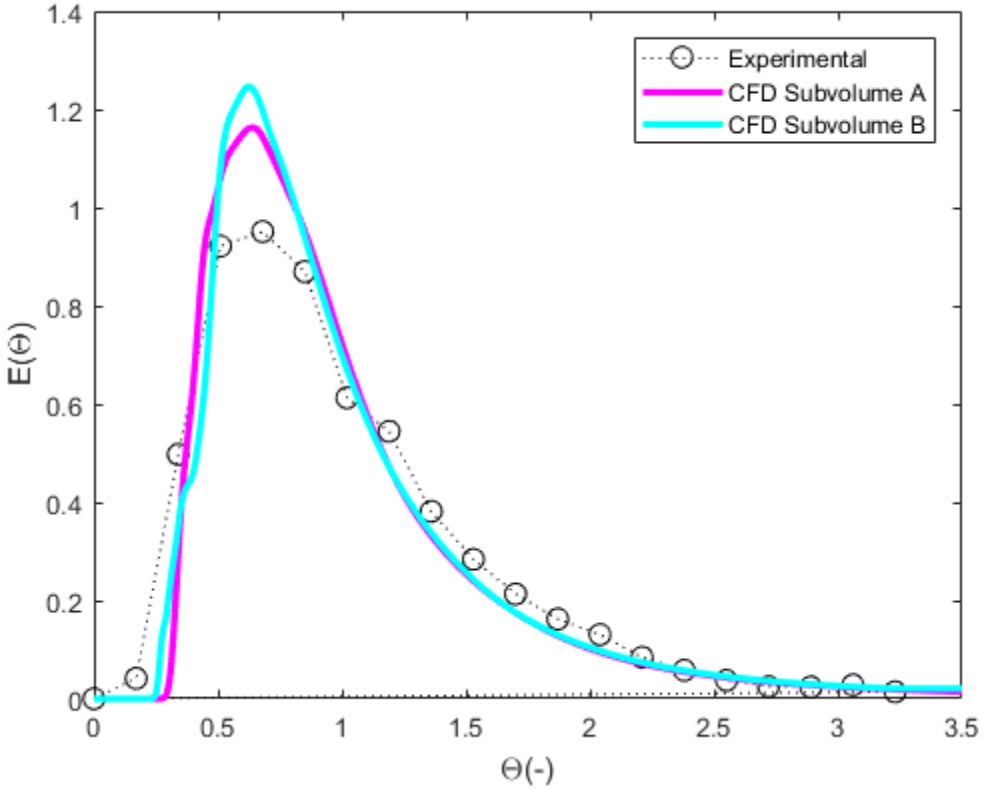

Figure 3.8. Comparison of computational fluid dynamics (CFD) and experimental dimensionless residence time distribution (RTD) curves

As it can be seen in Fig 3. 8, the two simulated RTD curves do not overlap completely. The peak of the curve for sub volume B is slightly higher than that of the curve for sub volume A. The simplest possible explanation is the higher porosity of sub volume B and its lower tortuosity (see Fig 3. 6), which translates in a lower fluid dispersion (and, thus, a higher and narrower peak). In this case-study, these differences are small; nevertheless, if significant structural non-uniformities exist, statistical treatment and/or creation of a representative average structure/morphology has been suggested in order to predict the behaviour of the whole monolith column [16,30].

The curve connecting experimental RTD points is slightly wider and lower than the computed RTD curves. This curve shape suggests that the experimental fluid dispersion is slightly larger than the dispersion in the computed domain [34]. This result is not unexpected, since the skeleton is considered as non-porous in the computed domain, as pores smaller than 1 μm in diameter were not captured by the X-ray tomography. Therefore, the predicted dispersion is slightly lower than the experimentally observed one. A higher image resolution, than that provided by the

tomography apparatuses used in the present study, would allow for capturing a more detailed monolith´s morphology, and will lead to an even better approximation between the modelling results and the physical reality. Nevertheless, the differences in the results obtained are not expected to be significant since in the case studied the fluid transport is dominated by advection. This confirms that the porous media morphology, associated with the flow heterogeneities, is the major contribution to the residence time distribution width in flow-driven applications [15]. In such a way, the proximity between the experimentally obtained and simulated curves validates the herein used modelling approach.

3.4. Conclusions and Outlook

In this study, we demonstrated the potential of a computational fluid dynamics (CFD) modelling approach to simulate fluid behaviour in monolithic porous columns, such as those used in chromatography. The structure of an alumina monolith porous column was reconstructed from 3D scans obtained by X-ray tomography. Afterwards, a computational fluid dynamics (CFD) study, consisting in first simulating the velocity and pressure fields, followed by simulation of tracer pulse injection were performed in randomly selected sub volumes of the 3D virtually reconstructed monolith. This approach enables a detailed characterisation of structural and hydrodynamic parameters such as streamlines (flow pathways), tortuosity and residence time distribution (RTD). The herein used approach obviates the need for model-dependent fitting parameters, thus being an important step towards process optimisation, in which monoliths (or other porous structures) are used.

In a very close future, chromatographic materials will be produced by additive manufacturing (AM), also known as 3D-printing, with the main advantage of being prepared according to the “made-on-demand” principle [29]. So far, this method has proven to be feasible for producing precisely controlled porous media with minimal apothem of 115 µm [49]. The performance of such 3D printed columns was validated by residence time distribution (RTD) measurements and radial and fractal flow distributor design procedures [49]. The *.stl* (stereolithography) files used to give information about geometry, shape and dimensions of 3D printed object are the same type of files used in this work to create computational mesh and perform CFD studies. Consequently, the herein presented CFD modelling approach can be used to optimise and virtually test the performance of chromatographic materials before being even printed/manufactured, thus leading

to production of materials “right at the first time” and according to the “design-for-purpose” approach.

References

[1] L.J. Gauckler, M.M. Waeber, C. Conti, M. Jacob-Dulière, Industrial Application of Open Pore Ceramic Foam for Molten Metal Filtration, in: J.F. Grandfield, D.G. Eskin (Eds.), Essent. Readings Light Met. Vol. 3 Cast Shop Alum. Prod., Springer International Publishing, Cham, 2016: pp. 251–262. doi:10.1007/978-3-319-48228-6_31.

[2] L.M. Rodríguez-Lorenzo, J.M.F. Ferreira, Development of porous ceramic bodies for applications in tissue engineering and drug delivery systems, Mater. Res. Bull. 39 (2004) 83–91. doi:10.1016/j.materresbull.2003.09.014.

[3] M. Scheffler, P. Colombo P, ed. In Cellular Ceramics: Structure, Manufacturing Properties and Applications (1st ed.). Wiley-VCH Verlag GmbH, Weinheim, 2005: pp 596-618.

[4] L.J. Gibson, M.F. Ashby, In Cellular Solids, Structure and Properties (2nd ed.). Cambridge University Press, Cambridge, England, 1999. pp. 82-87.

[5] H. Kobayashi, T. Ikegami, H. Kimura, T. Hara, D. Tokuda, N. Tanaka, Properties of monolithic silica columns for HPLC, Anal. Sci. 22 (2006) 491–501. doi:10.2116/analsci.22.491.

[6] G. Guiochon, Monolithic columns in high-performance liquid chromatography, J. Chromatogr. A. 1168 (2007) 101–168. doi:10.1016/j.chroma.2007.05.090.

[7] F.C. Leinweber, U. Tallarek, Chromatographic performance of monolithic and particulate stationary phases: Hydrodynamics and adsorption capacity, J. Chromatogr. A. 1006 (2003) 207–228. doi:10.1016/S0021-9673(03)00391-1.

[8] M.F. Sanches, N. Vitorino, C. Freitas, J.C.C. Abrantes, J.R. Frade, J.B. Rodrigues Neto, D. Hotza, Cellular ceramics by gelatin gelcasting of emulsified suspensions with sunflower oil, J. Eur. Ceram. Soc. 35 (2015) 2577–2585. doi:10.1016/j.jeurceramsoc.2015.03.008.

[9] M. Motokawa, H. Kobayashi, N. Ishizuka, H. Minakuchi, K. Nakanishi, H. Jinnai, K. Hosoya, T. Ikegami, N. Tanaka, Monolithic silica columns with various skeleton sizes and through-pore sizes for capillary liquid chromatography, J. Chromatogr. A. 961 (2002) 53–63. doi:10.1016/S0021-9673(02)00133-4.

[10] R. Hahn, M. Panzer, E. Hansen, J. Mollerup, A. Jungbauer, Mass transfer properties of monoliths, Sep. Sci. Technol. 37 (2002) 1545–1565. doi:10.1081/SS-120002736.

[11] T. Müllner, K.K. Unger, U. Tallarek, Characterization of microscopic disorder in reconstructed porous materials and assessment of mass transport-relevant structural descriptors, New J. Chem. 40 (2016) 3993–4015. doi:10.1039/C5NJ03346B.

[12] F. Gritti, G. Guiochon, Mass transfer kinetic mechanism in monolithic columns and application to the characterization of new research monolithic samples with different average pore sizes, J. Chromatogr. A. 1216 (2009) 4752–4767. doi:10.1016/j.chroma.2009.04.034.

[13] F. Gritti, G. Guiochon, Perspectives on the evolution of the column efficiency in liquid chromatography, Anal. Chem. 85 (2013) 3017–3035. doi:10.1021/ac3033307.

[14] D. Stoeckel, C. Kübel, M.O. Loeh, B.M. Smarsly, U. Tallarek, Morphological analysis of physically reconstructed silica monoliths with submicrometer macropores: Effect of decreasing domain size on structural homogeneity, Langmuir. 31 (2015) 7391–7400. doi:10.1021/la5046018.

[15] T. Müllner, A. Zankel, A. Höltzel, F. Svec, U. Tallarek, Morphological properties of methacrylate-based polymer monoliths: From gel porosity to macroscopic inhomogeneities, Langmuir. 33 (2017) 2205–2214. doi:10.1021/acs.langmuir.7b00337.

[16] H. Koku, R.S. Maier, M.R. Schure, A.M. Lenhoff, Modeling of dispersion in a polymeric chromatographic monolith, J. Chromatogr. A. 1237 (2012) 55–63. doi:10.1016/j.chroma.2012.03.005.

[17] T. Müllner, A. Zankel, C. Mayrhofer, A. Höltzel, Y. Lv, F. Svec, U. Tallarek, Reconstruction and characterization of polymeric monolithic stationary phases using serial block face scanning electron microscopy, Langmuir. 28 (2012) 16733–16737. doi:10.1021/la3038395.

[18] C. Jungreuthmayer, P. Steppert, G. Sekot, A. Zankel, H. Reingruber, J. Zanghellini, A. Jungbauer, The 3D pore structure and fluid dynamics simulation of macroporous monoliths: High permeability due to alternating channel width, J. Chromatogr. A. 1425 (2015) 141–149. doi:10.1016/j.chroma.2015.11.026.

[19] T. Müllner, A. Zankel, F. Svec, U. Tallarek, Finite-size effects in the 3D reconstruction and morphological analysis of porous polymers, Mater. Today. 17 (2014) 404–411. doi:10.1016/j.mattod.2014.07.003.

[20] K. Hormann, T. Müllner, S. Bruns, A. Höltzel, U. Tallarek, Morphology and separation efficiency of a new generation of analytical silica monoliths, J. Chromatogr. A. 1222 (2012) 46–58. doi:10.1016/j.chroma.2011.12.008.

[21] K. Hormann, U. Tallarek, Analytical silica monoliths with submicron macropores: Current limitations to a direct morphology-column efficiency scaling, J. Chromatogr. A. 1312 (2013) 26–36. doi:10.1016/j.chroma.2013.08.087.

[22] A. Daneyko, D. Hlushkou, S. Khirevich, U. Tallarek, From random sphere packings to regular pillar arrays: Analysis of transverse dispersion, J. Chromatogr. A. 1257 (2012) 98–115. doi:10.1016/j.chroma.2012.08.024.

[23] D. Hlushkou, K. Hormann, A. Höltzel, S. Khirevich, A. Seidel-Morgenstern, U. Tallarek, Comparison of first and second generation analytical silica monoliths by pore-scale simulations of eddy dispersion in the bulk region, J. Chromatogr. A. 1303 (2013) 28–38. doi:10.1016/j.chroma.2013.06.039.

[24] D. Hlushkou, S. Bruns, A. Holtzel, U. Tallarek, From pore scale to column scale dispersion in capillary silica monoliths, Anal. Chem. 82 (2010) 7150–7159. doi:10.1021/ac101393b.

[25] D. Hlushkou, S. Bruns, U. Tallarek, High-performance computing of flow and transport in physically reconstructed silica monoliths, J. Chromatogr. A. 1217 (2010) 3674–3682. doi:10.1016/j.chroma.2010.04.004.

[26] D. Hlushkou, S. Bruns, A. Seidel-Morgenstern, U. Tallarek, Morphology-transport relationships for silica monoliths: From physical reconstruction to pore-scale simulations, J. Sep. Sci. 34 (2011) 2026–2037. doi:10.1002/jssc.201100158.

[27] S. Bruns, T. Hara, B.M. Smarsly, U. Tallarek, Morphological analysis of physically reconstructed capillary hybrid silica monoliths and correlation with separation efficiency, J. Chromatogr. A. 1218 (2011) 5187–5194. doi:10.1016/j.chroma.2011.05.090.

[28] S. Bruns, T. Müllner, M. Kollmann, J. Schachtner, A. Höltzel, U. Tallarek, Confocal laser scanning microscopy method for quantitative characterization of silica monolith morphology, Anal. Chem. 82 (2010) 6569–6575. doi:10.1021/ac100909t.

[29] M.T. Hearn, Trends in additive manufacturing of chromatographic and membrane materials, Curr. Opin. Chem. Eng. 18 (2017) 90–98. doi:10.1016/j.coche.2017.11.003.

[30] V.A. Haaksman, A. Siddiqui, C. Schellenberg, J. Kidwell, J.S. Vrouwenvelder, C. Picioreanu, Characterization of feed channel spacer performance using geometries obtained by X-ray computed tomography, J. Memb. Sci. 522 (2017) 124–139. doi:10.1016/j.memsci.2016.09.005.

[31] T.F. Johnson, P.R. Levison, P.R. Shearing, D.G. Bracewell, X-ray computed tomography of packed bed chromatography columns for three dimensional imaging and analysis, J. Chromatogr. A. 1487 (2017) 108–115. doi:10.1016/j.chroma.2017.01.013.

[32] K.B. Hatzell, J. Eller, S.L. Morelly, M.H. Tang, N.J. Alvarez, Y. Gogotsi, Direct observation of active material interactions in flowable electrodes using X-ray tomography, Faraday Discuss. 199 (2017) 511–524. doi:10.1039/C6FD00243A.

[33] C.A.M. Portugal, J.C. Lima, J.G. Crespo, Effect of physicochemical conditions on the ultrafiltration of β-lactoglobulin: Fluorescence probing of induced structural changes, J. Memb. Sci. 321 (2008) 69–80. doi:10.1016/j.memsci.2007.11.027.

[34] O. Levenspiel, Chemical reaction engineering, Third Edition, John Wiley & Sons, United States of America, 1999, pp. 257-320. doi:10.1021/ie990488g.

[35] S. Pawlowski, V. Geraldes, J.G. Crespo, S. Velizarov, Computational fluid dynamics (CFD) assisted analysis of profiled membranes performance in reverse electrodialysis, J. Memb. Sci. 502 (2016) 179–190. doi:10.1016/j.memsci.2015.11.031.

[36] S. Pawlowski, T. Rijnaarts, M. Saakes, K. Nijmeijer, J.G. Crespo, S. Velizarov, Improved fluid mixing and power density in reverse electrodialysis stacks with chevron-profiled membranes, J. Memb. Sci. 531 (2017) 111–121. doi:10.1016/j.memsci.2017.03.003.

[37] P. Pánek, R. Kodým, D. Šnita, K. Bouzek, Spatially two-dimensional mathematical model of the flow hydrodynamics in a spacer-filled channel - The effect of inertial forces, J. Memb. Sci. 492 (2015) 588–599. doi:10.1016/j.memsci.2015.03.099.

[38] M.J. Nieves-Remacha, A.A. Kulkarni, K.F. Jensen, OpenFOAM computational fluid dynamic simulations of single-phase flows in an advanced-flow reactor, Ind. Eng. Chem. Res. 54 (2015) 7543–7553. doi:10.1021/acs.iecr.5b00232.

[39] S. Pawlowski, J.G. Crespo, S. Velizarov, Pressure drop in reverse electrodialysis: Experimental and modeling studies for stacks with variable number of cell pairs, J. Memb. Sci. 462 (2014) 96–111. doi:10.1016/j.memsci.2014.03.020.

[40] A. Delavari, R. Baltus, The effect of the pore entrance on particle motion in slit pores: Implications for ultrathin membranes, Membranes 7, 42 (2017). doi:10.3390/membranes7030042.

[41] S. Pawlowski, P. Sistat, J.G. Crespo, S. Velizarov, Mass transfer in reverse electrodialysis: Flow entrance effects and diffusion boundary layer thickness, J. Memb. Sci. 471 (2014) 72–83. doi:10.1016/j.memsci.2014.07.075.

[42] C.J. Gommes, A.J. Bons, S. Blacher, J.H. Dunsmuir, A.H. Tsou, Practical methods for measuring the tortuosity of porous materials from binary or gray-tone tomographic reconstructions, AIChE J. 55 (2009) 2000–2012. doi:10.1002/aic.

[43] S. Khirevich, A. Höltzel, A. Daneyko, A. Seidel-Morgenstern, U. Tallarek, Structure-transport correlation for the diffusive tortuosity of bulk, monodisperse, random sphere packings, J. Chromatogr. A. 1218 (2011) 6489–6497. doi:10.1016/j.chroma.2011.07.066.

[44] K. Hormann, V. Baranau, D. Hlushkou, A. Höltzel, U. Tallarek, Topological analysis of non-granular, disordered porous media: determination of pore connectivity, pore coordination, and geometric tortuosity in physically reconstructed silica monoliths, New J. Chem. 40 (2016) 4187–4199. doi:10.1039/C5NJ02814K.

[45] M. Barrande, R. Bouchet, R. Denoyel, Tortuosity of porous particles, Anal. Chem. 79 (2007) 9115–9121. doi:10.1021/ac071377r.

[46] R. Dias, J.A. Teixeira, M. Mota, A. Yelshin, Tortuosity variation in a low density binary particulate bed, Sep. Purif. Technol. 51 (2006) 180–184. doi:10.1016/j.seppur.2006.01.010.

[47] L. Pisani, Simple expression for the tortuosity of porous media, Transp. Porous Media. 88 (2011) 193–203. doi:10.1007/s11242-011-9734-9

[48] F.C. Leinweber, D. Lubda, K. Cabrera, U. Tallarek, Characterization of silica-based monoliths with bimodal pore size distribution, Anal. Chem. 74 (2002) 2470–2477. doi:10.1021/ac011163o.

[49] C. Fee, S. Nawada, S. Dimartino, 3D printed porous media columns with fine control of column packing morphology, J. Chromatogr. A. 1333 (2014) 18–24. doi:10.1016/j.chroma.2014.01.043.

Chapter 3: CFD modelling of flow patterns, tortuosity and RTD in monolithic porous columns reconstructed from X-ray tomography

CHAPTER 4

Surface Modification of Alumina Monolithic Columns with 3-Aminopropyltetraethoxysilane (APTES) for Protein Attachment

Published as: *N. Nayak, R. Huertas, J.G. Crespo, C.A.M. Portugal, Surface Modification of Alumina Monolithic Columns with 3-Aminopropyltetraethoxysilane (APTES) for Protein Attachment, Sep. Purif. Technol. (2019) 115674.*

Abstract

In the present work, a simpler and expedited functionalization method was used envisaging the preparation of functionalized alumina monoliths for effective purification of immunoglobulins. Single stage sol-gel synthesis method was used for the silanization of alumina monoliths with (3-Aminopropyl)triethoxysilane (APTES) in an aqueous environment. The nature of the attachment of APTES to the alumina and its distribution through the monolith column was evaluated through FTIR-ATR, SEM-EDS and XPS measurements. Monolith silanization process was optimized by adjustment of the reaction conditions in terms of catalyst used (acid or base), temperature and using a factorial design approach to elicit the interdependent influence of humidity, number of APTES coating layers and precursor concentration on the silanization of alumina. The reaction was found to be optimum at basic pH and a temperature of 80˚C. Etching free functionalized monoliths with highest amine density of 166 µmol/g of the column were obtained upon a single coating with a 2M APTES solution, at 100% humidity. The binding capacity of the functionalized alumina monolith was conducted using BSA and Protein A and then with the immunoglobulin G (IgG) aiming to infer about the suitability of the functionalized alumina monolith for purification of immunoglobulins. Adsorption-elution experiments showed that the functionalized alumina monoliths allowed the attachment of 0.78 mg IgG per mg of bound Protein A and the recovery of 89% of the captured IgG.

4.1. Introduction

Development of porous monolithic columns has received considerable attention in recent years specially for application as a chromatographic medium for separating proteins since they combine an increased surface area, good accessibility to the ligands and reduced diffusional hindrances [1]. Therefore, monolithic stationary phases prepared from ceramic materials like alumina or porous silica could be an efficient and effective alternative to particulate beds as they allow for a much higher permeability due to the high porosity (50-70%) and a large, modifiable skeleton [2]. Such columns usually have a hierarchical porous structure with an intertwined network of channels of 2–8 µm diameter enabling easy convective transport and a mesoporous structure comprising pores with 1–2 µm of average diameter [3–5]. This enables effective interaction between the components of the flowing liquid and surface-attached ligands in the column. There are several techniques available to functionalize the relatively inert ceramic materials, ranging from physical methods like sputtering to chemical modification methods like silanization [6–12]. Silanization involves attachment of silanol containing groups onto the surface of a material and is usually carried out by sol-gel synthesis. As it is a popular technique a wide range of silane agents

are available which opens the possibility to functionalize the surface with the desired functional groups. This provides scope for developing materials for variety of purposes from catalysis to protein separation. It is well documented that proteins interact with aldehyde, amine or epoxy groups most effectively [8,10,13–15]. Therefore, there are several possibilities from the perspective of silane agents which can be used to functionalize a column for protein separation. Amino silanes are among the most economical and easily available. They also tend to form strong bonds with proteins and therefore are quite popular. However, there are also certain problems associated with the use of amine agents, mainly they tend to affect material integrity and cause etching [8]. Therefore, it is important to achieve a balance between available amine groups and column integrity.

There are several factors which influence silanization. The effect of humidity is well documented as it supplies the necessary OH groups for the formation of silanol complexes [8,16–18] and is therefore critical to the process. Further, factors such as precursor concentration and number of silanization coats influence the density and availability of functional groups. The reaction temperature plays a major role in the preservation of structural integrity by reducing etching [8,19]. It is therefore imperative that these factors be optimized to obtain ideal conditions, and thus effective media for separation/purification.

In the present work, we have developed a simplified modified silanization method to produce amine functionalized alumina monoliths using (3-Aminopropyl)triethoxysilane as the silane agent at relatively moderate conditions. The functionalized monoliths have been characterized by specific analytical techniques, including FTIR, SEM-EDX, XPS and ninhydrin assay to determine the type of bond, binding strength, distribution and quantity of available amine groups throughout the monolith. Further, we have optimized the silanization parameters like temperature, pH, humidity (%RH), initial precursor concentration and number of coatings to obtain monoliths with most favorable characteristics considering their future application for protein separation. In this regard, we have carried out proof of concept studies using these monoliths and assessed the effectiveness of binding BSA and Protein A to these columns and capacity to attach immunoglobulin G (IgG).

4.2. Materials and Methods

4.2.1. Materials

(3-Aminopropyl)triethoxysilane, ninhydrin reagent, hydrindantin, dimethyl sulfoxide, bovine serum albumin (BSA), sodium dodecyl sulfate (SDS), gelatin porcine skin (Oxoid – LP 0008) and glycine

were procured from Sigma Aldrich. Alumina (CT-3000) was supplied from Alcoa chimie. Commercially available corn oil. castor oil and margarine were used. Dolapix PC67 was procured from Zschimmer and Schwarz. Analytical grade sulfuric acid (concentrated), citric acid, sodium citrate, sodium chloride, hydrochloric acid (concentrated), sodium hydroxide pellets, ethanol, acetic acid, di-sodium hydrogen phosphate and sodium di-hydrogen phosphate were purchased from local distributors. Standard Bicinchoninic acid assay (BCA) and Protein A were procured from Thermo Fisher. Heat-shrink Teflon tubes were acquired locally. Fittings for the columns were obtained from Biotoolomics PLC., UK.

4.2.2. Column Preparation

Alumina monolithic columns were prepared as described elsewhere [5]. Briefly, an alumina suspension was prepared with 50% (v/v) of water and added deflocculent (10% Dolapix). This suspension was used as the continuous phase to prepare an emulsion with cooking oil with a fixed phase ratio of oil: water of 1.5. An emulsifier (Sodium Dodecyl Sulfate, SDS) was added to stabilize the emulsion and additionally, a gelling agent (Gelatin) was added to solidify the monolith structure. This emulsion was poured into column shaped molds of dimension 1.1 cm (diameter) x 5 cm (length). Once sufficiently solidified the columns were taken out of the mold and sintered with an appropriate temperature cycle up to 1550 °C. The columns obtained after sintering had average pore sizes of ~2 µm (determined by mercury intrusion porosimetry as fully described in our previous paper [5]) and were further modified.

4.2.3. Silanization

To prepare the columns for functionalization they were pretreated by immersion in 30% H_2O_2 along with application of vacuum until the solution stopped bubbling. These samples were then heated at 80 °C for 90 minutes. The columns were then dried at 80 °C for 16 hours.

A silanization reaction mixture containing APTES: EtOH: H_2SO_4:: 1: 9: 0.004 (molar ratios) was prepared and incubated at 60 °C for 90 minutes. The dried columns were added to this reaction mixture and vacuum was applied to completely perfuse the reaction mixture into the pores of the column. These columns were then incubated at 60 °C for a further 90 minutes. Subsequently the columns were removed from the reaction mixture and dried in air at room temperature for 24-48 hours.

4.2.4. Characterization of the monolithic columns

In order to determine the nature and abundance of the silane attached to the alumina columns, several characterization steps were performed.

Fourier transform infrared – attenuated total reflectance (FTIR-ATR)

Fourier transform infrared (FTIR) spectral analysis gives information regarding the presence of certain types of functional groups in a given sample. In this context we used FTIR to detect the presence of silanes in the modified columns. Pellets were prepared using a 1:3 weight ratio of powdered sample to KBr (de-moisturized). A Thermo Scientific Nicolet 6700 FTIR (Fourier Transform infrared) with ATR (attenuated total reflectance) equipment was used. Software package Omics was used to analyze the signals obtained from the sample.

Scanning electron microscopy (SEM-EDX)

Scanning electron microscopy (SEM) was used to inspect the microstructural features of the sintered monoliths after carbonizing the sample with graphite. These analysis were performed using a SEM equipment (SU1510, Hitachi) coupling an energy dispersive X-ray system (EDX). The attached energy dispersive X-ray spectrum (EDX) helped reveal the elemental composition of the observed region and was used to determine the presence and dispersion of Si (relative to the presence of APTES), C, Al and O in the column after silanization.

X-ray photoelectron spectroscopy (XPS)

Further chemical characterization of the surface of the studied monoliths was performed by XPS in order to investigate the silanization efficiency through the column diameter. With this purpose, XPS analysis were performed at 4 points of the sample cross-sectional surface (2 points at the cross-section edges and 2 near the center). A Physical Electronics spectrometer (PHI 5700) with X-ray Mg Ka radiation (300W, 15 kV, 1253.6 eV) as the excitation source was used. High-resolution spectra were recorded at a given take-off angle of 45º by a concentric hemispherical analyzer operating in the constant pass energy mode at 29.35 eV, using a 720 µm diameter analysis area. Binding energies were determined with respect to the position of the adventitious C 1s peak at 285.0 eV, and the residual pressure in the analysis chamber was maintained below 5×10^{-7} Pa during data acquisition. Samples were kept overnight at high vacuum in the preparation chamber before being transferred to the analysis chamber of the spectrometer for testing. Each spectral region was scanned several sweeps up to a good signal to noise ratio was observed. PHI ACCESS ESCA-V6.0 F software package was used for acquisition and data analysis. A

Shirley-type background was subtracted from the signals. Recorded spectra were always fitted using Gauss–Lorentz curves and following the methodology described in detail in [20,21], in order to determinate more accurately the binding energy (BE) of the different element core levels. Atomic concentration (A.C.) percentages of the characteristic elements (Al, N, Si) on the sample surfaces were determined taking into account the corresponding area sensitivity factor for the different measured spectral regions [20,22](Table 4. 1).

4.2.5. Optimization of column silanization process: effect of the silanization parameters

Effect of acidic or basic catalyst on silanization

The effect of acidic/basic catalyst on the effectiveness of silanization was tested by substituting H_2SO_4 with 1M NaOH. FTIR spectra were used to evaluate the effects, specifically the bands in the range of 3200-3500 cm^{-1} for the OH groups and in range of 1500-1700 cm^{-1} for N-H groups. The presence or absence of other bands was also evaluated.

Effect of humidity, concentration of amine precursor, number of coats

There are several factors which affect the effectiveness of silanization. Among them humidity, concentration of the precursor and the number of the coating layers are well known to influence the formation and durability of the silane coating formed. Therefore, a conventional 3 level full factorial design was applied considering humidity, concentration of amine precursor (APTES) and number of coating layers as the three factors which were varied at 3 levels. The design comprised 27 experiments (Table A3. 1. in Supplementary materials).

The obtained samples were tested for primary amine (δ N-H) and -OH (hydroxyl concentrations). The δ N-H concentration was determined to quantify the amount the APTES bound in each column sample, using the ninhydrin method, wherein 100 mg of each crushed sample was taken in test tubes and 1 mL of Ninhydrin reagent was added. This mixture was vigorously stirred and boiled in a digester at 100 °C for 10 minutes. After cooling to room temperature, 10 mL of ethanol was added to each tube and the absorbance was read at 570 nm. The blank was prepared by substituting the sample with water and two controls were used one with pure ethanol and one prepared using pure alumina powder. A calibration curve was prepared using APTES in the concentration range of 0 – 0.43 µmol/mL (0-0.01 % v/v).

The OH groups were determined to identify the possibility of other available reactive groups for protein binding. They were quantified based on peak height by normalizing all the FTIR spectra against the control sample of pure alumina.

Effect of temperature

Temperature of incubation of the reaction mixture plays an important role in the stability and durability of the coating. Hence, the effect of incubation temperature of reaction mixture was also evaluated at 3 different temperatures i.e., at 40 °C, 60 °C and 80 °C. The samples were tested for presence of functional groups (FTIR) and stability in an aqueous environment i.e., visually verified for etching.

4.2.6. Evaluation of the monolith performance

Preparation of the monolith for the simulated stirred flow setup

The amine functionalized alumina monoliths were initially weighed (dry weight) and their size was measured (length and diameter) with a Vernier caliper. Then they were inserted in the Teflon tubing and a short duration of heat was applied externally to the tube using a standard Bunsen burner to shrink the tube to tightly wrap around the monolith – making it water-tight around the sides. The HPLC fittings were then attached to the ends of the tube.

Simulated stirred flow setup and operation

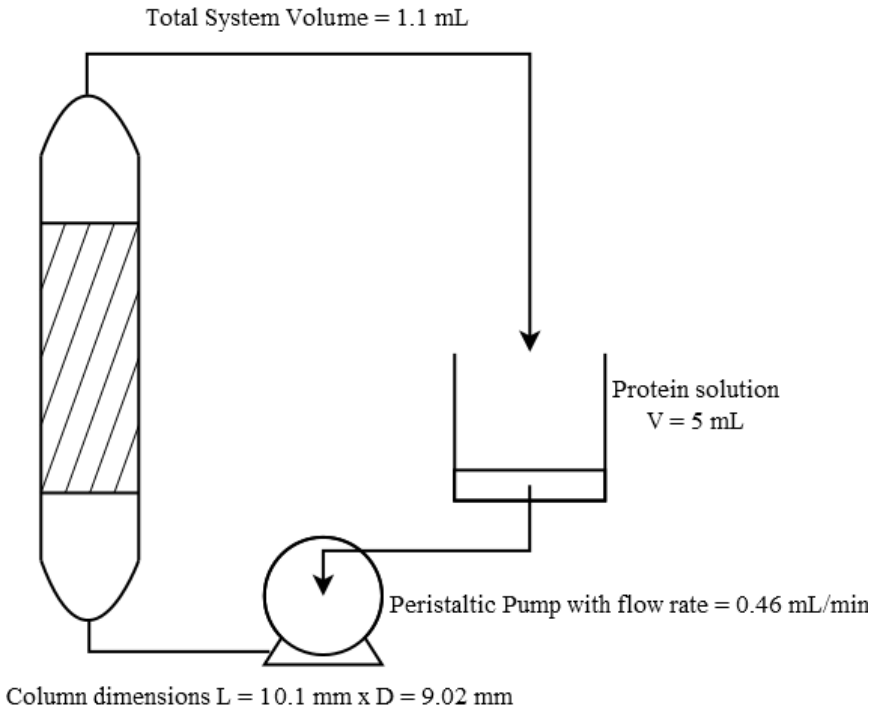

Figure 4.1. Process set up used in protein binding experiments

The setup was assembled as can be seen in the scheme in Fig 4. 1. The heat-shrink Teflon tube wrapped monoliths, modified with APTES, were connected with reservoirs containing 5 mL of

protein solution, through a peristaltic pump. This configuration of the setup was used to ensure the complete wetting of the highly porous monoliths. Standard HPLC fittings were used for the connections. The pumps were calibrated before each run and the final flow rates were also checked after each attachment cycle.

Operation of the setup

Initially, the column was equilibrated by re-circulating 5 mL of phosphate buffer (50 mM, pH=7.4) for 1 hour. Subsequently the column was emptied. Protein A solution (5 mL) was used as the feed solution (reservoir). The pump was set to a flow rate of 0.467 $ml.min^{-1}$ and the experiment was started. Once the column was completely filled the time was recorded. Samples (100 µL) were drawn from the reservoir every 30 minutes for the first 3 hours and then finally after 17 hours. The sample volume lost from the system was accounted for in the calculations. After 17 hours the column was emptied and a rapid wash with 5 ml of fresh buffer was carried out, without re-circulation. Note that the column was eluted for 17 h, to assure the maximum attachment of Protein A, for column characterization purposes. Subsequently, the column was subjected to a re-circulated wash with fresh phosphate buffer for 1.5 hours. The experiments were carried out for initially for using BSA (0.5 $mg.\ mL^{-1}$) and then using Protein A concentration of 1.0 $mg.\ mL^{-1}$. The protein was quantified using standard Bicinchoninic acid assay (BCA) test using the test kit procured from Thermo Fisher Scientific [23], USA.

4.2.7. Binding stability experiments

To determine the stability and durability of the protein bound to the column, a set of stability or detachment experiments were carried out by altering pH conditions and ionic strength.

Binding stability experiments with pH modulation were carried out using Glycine-HCl (pH=3.1) and Glycine-NaOH (pH=11) buffers at concentrations of 0.1 M and 1 M. The buffer (2 mL) was taken in the reservoir and the experiment was carried out at flow rate of 0.467 ml.min-1 for 19 hours. A sample (control) was drawn at the beginning of the experiment and a final sample was collected after 19 hours. Since the pH of the buffers are at extremes (3.1 and 11) the samples had to be treated by acetone precipitation before quantification using the BCA test kit, as described in the protocol by Thermo Fisher [23]. The precipitated samples were then re-dissolved in PB at pH=7.4 and subsequently quantified.

Stability experiments with modulation of ionic strength were carried out using 5 mM and 0.1 M NaCl solutions. Briefly, 2 mL of saline solution was taken in the reservoir and the experiment was

carried out at flow rate of 0.467 mL.min^{-1} for 19 hours. Similar to the pH experiments, a sample (control) was drawn at the beginning of the experiment and a final sample was collected after 19 hours. Additionally, an experiment was carried out at temperature of 50 °C also for each concentration to check if temperature had any effect on the binding.

4.2.8. IgG adsorption – elution experiment

To test the possibility of using the Protein A attached monolith as an affinity chromatography column for IgG purification a simple adsorption-desorption test was carried out. IgG (5mg) in 5ml of phosphate buffered saline (50 mM @ph = 7.4 with 150 mM NaCl) was re-circulated through the column for 6 hours. Subsequently, the column was washed with pure PBS to remove any un-attached IgG. Following this, the IgG was eluted out using a citrate buffer (25 mM, pH = 3.5).

4.3. Results and Discussion

Alumina is a relatively inert material and is generally highly stable in most environments. To effectively use it as a base material (substrate) for application in separation processes it is necessary to appropriately functionalize it with groups which can improve its efficacy to the compounds of interest. Silanization is an effective way of functionalizing or derivatizing inorganic structures. It has been used very effectively with silica wafers [24] and even alumina particles [25] among others. The ultimate objective of this work was to prepare alumina monolithic columns for affinity-based separations of proteins, taking advantage of their excellent mass transport properties. Therefore, the alumina monoliths were functionalized with appropriate functional groups capable to bind ligands, such as protein A and protein G, depicting high specificity towards the proteins of interest (e.g. immunoglobulins). According to that reported in further literature, Protein A and Protein G have high efficacy for attachment to either amine groups or epoxy groups [13,15,26,27]. There were several possible silane agents to choose from [28], however, (3-Aminopropyl)triethoxysilane was chosen because it is quite well studied and has previously been applied in a similar context i.e., for attachment of peptides [16]. The alumina surface was then activated by a pre-treatment with H_2O_2 for inducing the formation -OH groups on the surface.

4.3.1. Functionalization of alumina monolith samples by single step silanization method

Conventionally, silanization is performed in two steps: in the first step a silane agent such as triethylmethoxysilane (TEOS) is first attached to a surface and subsequently APTES is attached to TEOS. This process usually takes place in an organic solvent like toluene with typically low concentrations of the silane agent, in the range of 1%-5%, which showed to work very well for

silica wafers [11,24]. The same approach was attempted to functionalize the alumina samples prepared in the present work but the signal for the δ N-H bonds around 1650-1550 cm^{-1} [22] and C-N (around 1400-1000 cm^{-1} [22]) in the IR spectra was not detected (Fig 4. 2).

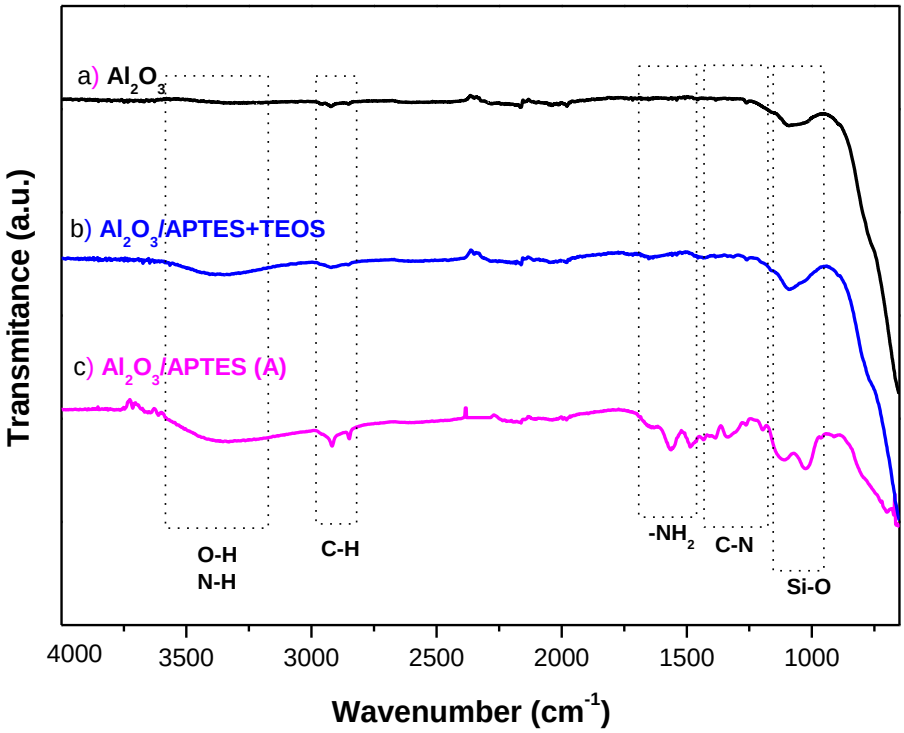

Figure 4.2. FTIR spectra for a) pristine Al2O3 b) Al2O3 modified with TEOS by conventional method then attaching of APTES to TEOS and c) direct reaction of APTES with alumina

Therefore, a different functionalization method was developed following the used by Yamaguchi et al [29]. The method described by these authors [29] consisted of a simple one step pre-activation of TEOS in an ethanol-based aqueous system by an acidic catalyst (H_2SO_4) at a relatively low temperature of 60 °C and subsequent reaction with the inorganic sample, which in their case was a silicon wafer. In the present work, the strategy developed by Yamaguchi et al. [29] was adapted by modification of few parameters to obtained functionalized monoliths by covalent binding of APTES. As can be seen in the FTIR spectrum shown in Fig. 4. 2, there are clear peaks in the range of 1350-1500 cm^{-1} corresponding to the reduced signals from C-N stretching bonds meaning that there was a reaction taking place between Al(OH) and APTES proving that this functionalization method was successful allowing the preparation of alumina coated with amine groups (primary amine N-H bend at 1650-1580 cm^{-1}). The probable reaction mechanism is pictorially represented in Fig 4. 3.

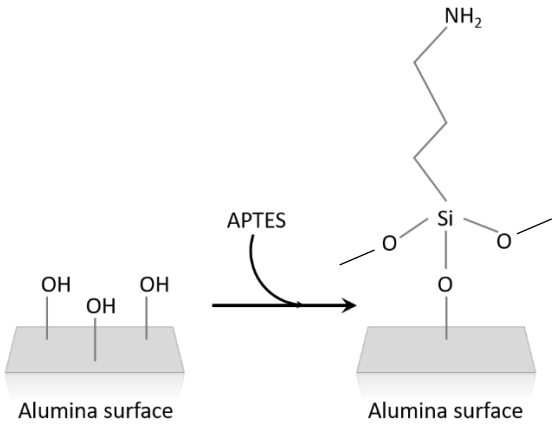

Figure 4.3. Schematic representation of the APTES binding mechanism to alumina surface

To corroborate these results, the samples were further characterized with SEM-EDX. The images obtained by SEM-EDX are shown in Fig 4. 4, highlighting the presence and distribution of C and Si (standing for the efficiency of APTES coating) in cyan and yellow colors in Fig. 4. 4 (b) and Fig. 4. 4 (c), respectively. The sample was taken from the lateral and longitudinal center of the column to infer about the homogeneity of the silanization. From SEM-EDX analysis it was possible to conclude that a uniform coating of Si and C appear to be deposited on the alumina.

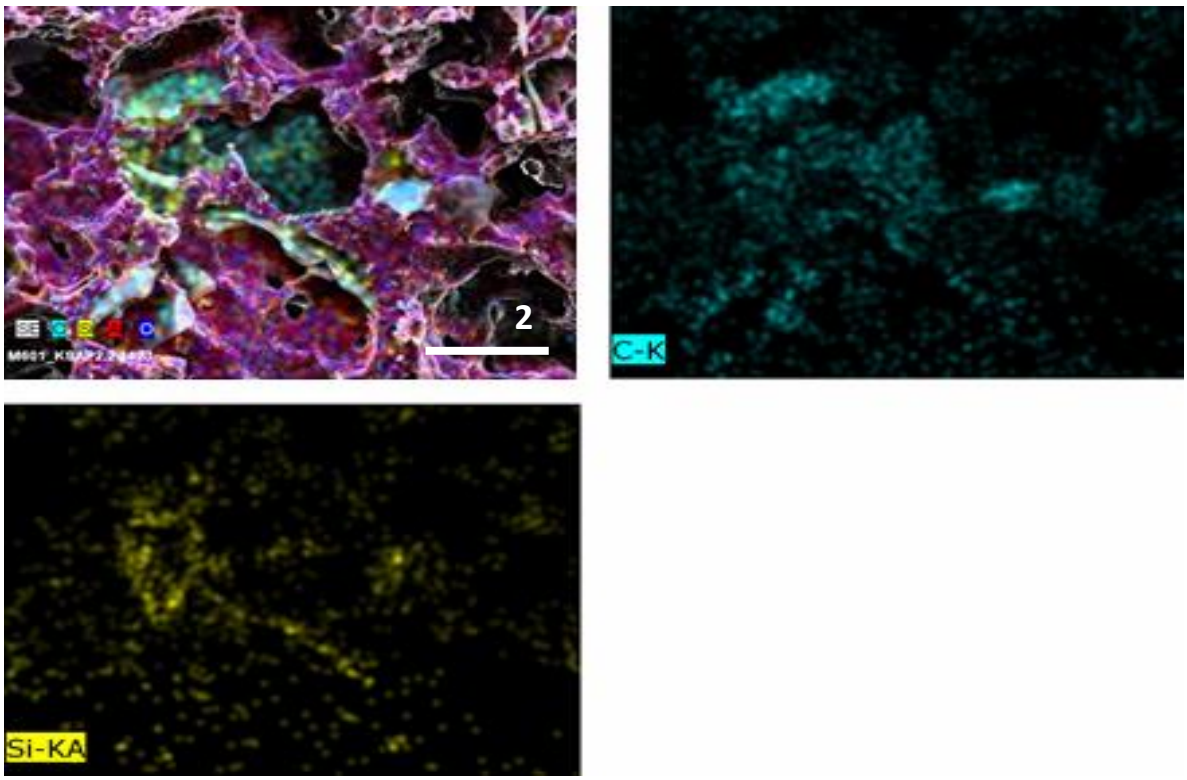

Figure 4.4. SEM-EDS images for alumina samples functionalized by the modified Yamaguchi method a) SEM-EDS imaging mapping different elements on the observed surface b) EDS map of Carbon on the surface c) EDS map of Silicon on the surface

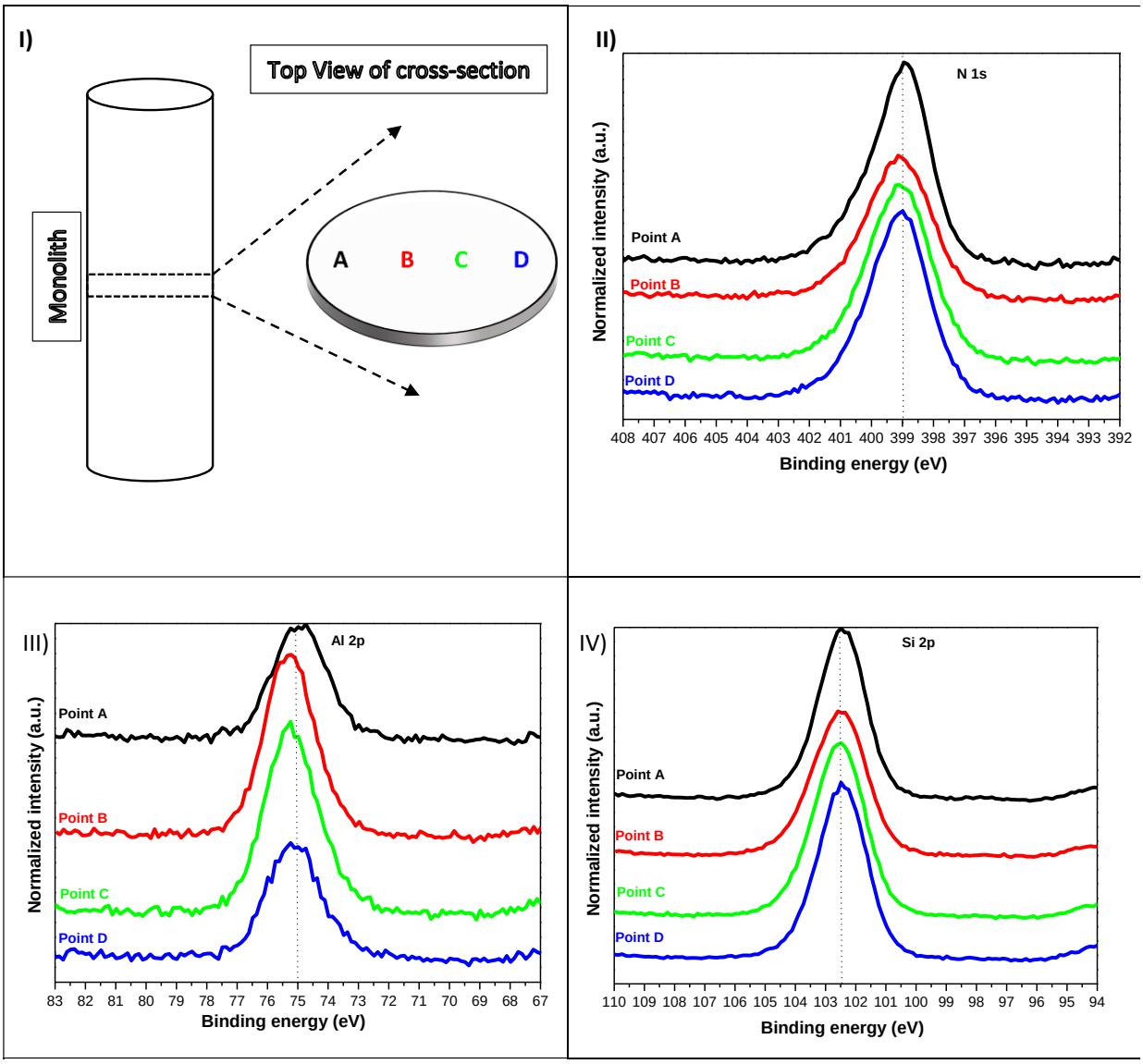

Figure 4.5. XPS spectra for APTES coated alumina samples: I) Schematic representation of the positions from where samples were obtained II) Spectra for Al 2p III) Spectra of Si 2p IV) Spectra of N 1s

The homogeneity of the alumina coating with APTES was also evaluated by XPS analysis. As shown in Fig 4. 5 (I), the APTES-coated alumina column was cut along its diameter at the center and the XPS spectra were acquired at 4 different points (A to D) along the column diameter: two points at the extremities of the diameter, represented by points A and D and two points at the bulk of the column represented by points B and C. The N 1s core-level spectrum can be curve-fitted with two peak components (Fig. 4. 5 II). The peak at around 399.5 eV is ascribed to the residual

neutral amino groups, and the peak at around 402.1 eV is assigned to the new quaternary ammonium cations. Considering that the documented binding energy of Al_2O_3 should be between 74 eV and 75 eV, and our samples show a small shift in the binding energy to ~75.3 eV we can assume that the alumina has reacted with the silanol groups (with Si showing a B.E of ~103.7 eV as shown in Fig. 4. 5. III). This is further corroborated by the lower % atomic composition of Alumina at points A and D as compared to points B and C (as in Table 4. 1). However, and despite the lower intensity and atomic % of Al in the spectra at the peripheral regions (points A and D) than at the column bulk, is possible to conclude that the APTES coating was consistent taking into account the molecular composition of APTES, i.e. the atomic % of C, Si, N and O in the APTES molecule, is similar to the atomic % of these elements in the alumina surface, as shown in Table 4. 1. Furthermore, analysis of Table 4. 1 shows that the % of C and Si (which are only ascribed to the presence of APTES) is quite identical at all four points, also matching the atomic % of these elements in APTES molecule. These results are strong indications of an extensive and homogeneous monolith functionalization.

Table 4.1. Atomic concentration (A.C.) percentages of the characteristic elements (C. O, Al, N, Si) on the sample surfaces were determined taking into account the corresponding area sensitivity factor for the different measured spectral regions

	C (%)	O (%)	Al (%)	N (%)	Si (%)
Point A	55.2	23.2	3.6	7.6	10.1
Point B	51.5	25.4	6.6	6.7	9.4
Point C	48.8	27.1	9.0	5.6	9.1
Point D	53.5	24.3	5.4	6.3	9.8

A solid-state NMR analysis was also carried out on the samples in order to have a better insight on the nature of the APTES binding to alumina, but the results were not conclusive. The results show that there was significant amount of Si and primary N-H groups in the sample masking the Al signal (See Fig. A4. 1 in Supplementary materials).

4.3.2. Optimization of the alumina functionalization

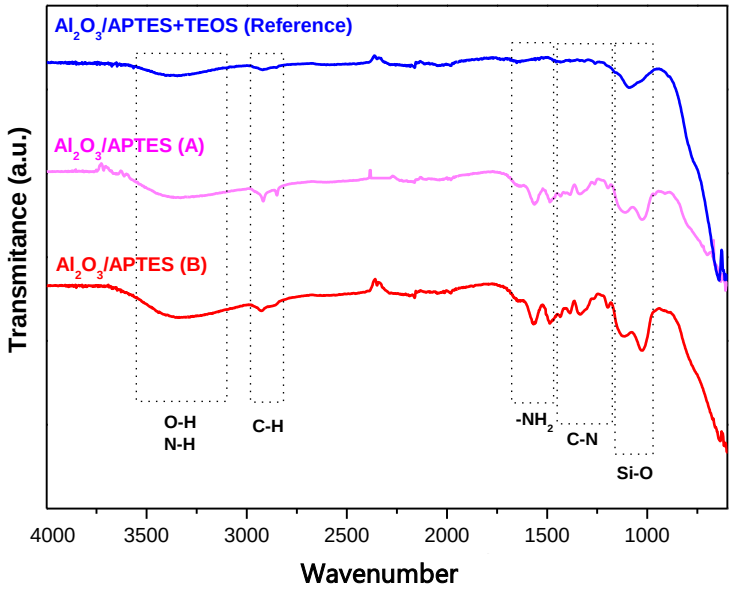

Figure 4.6. FTIR-ATR spectra showing the effect of pH on amine groups in silanization carried out using (A) concentrated H_2SO_4 and (B) 1M NaOH as the catalyst.

Legend: These FTIR-ATR spectra are compared with that obtained for Al_2O_3 modified by conventional method of attachment of TEOS then attachment of APTES to TEOS (as reference)

As our goal was to develop a protein affinity separation medium, specifically for purification of IgG, therefore it is important to have a highly porous medium meeting the characteristics which assure high and stable of immune-specific ligands, such as protein A or protein G. Protein attachment takes place primarily via the primary amine groups present on the functionalized column. Therefore, it is imperative to optimize the silanization conditions to improve the quantity and homogeneity of amines. The first step towards this was to determine which components of the silanization reaction mixture had an ultimate effect on the quantity and dispersion of amine groups in the monolith. Hence, the effect of pH (catalyst) was studied. As can be seen in FTIR-ATR spectra in Fig 4. 6, switching the catalyst (pH) from acidic (A) to basic (B) had a very significant effect on the intensity of the primary amine peak, observed at 1600 cm^{-1}, confirming the increase in quantity of APTES in the monolith at basic conditions.

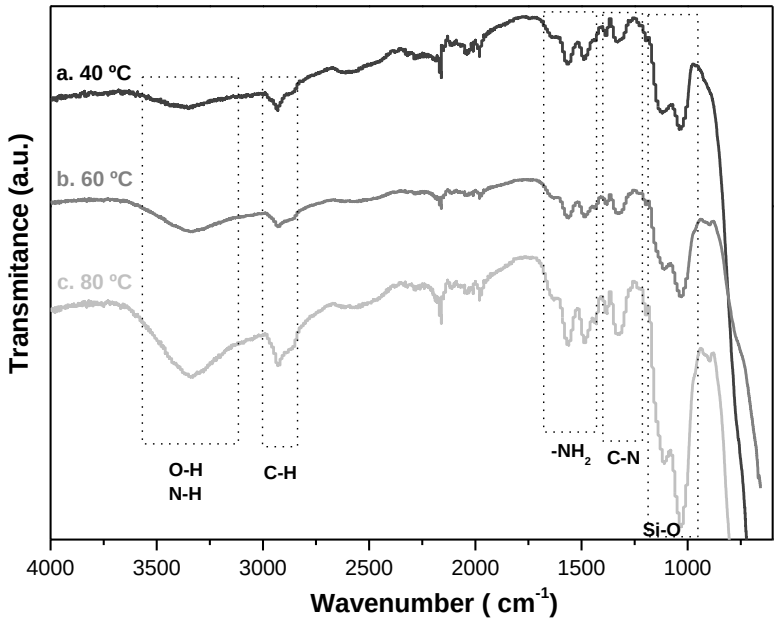

Figure 4.7. Effect of reaction temperature on silanization. FTIR-ATR spectra acquired for functionalized alumina samples silanized at a) T = 40˚C, b) T = 60˚C and c) T = 80˚C

One of the main issues faced when using amine silanes was the problem of the etching in aqueous environments. It was consistently observed that the column material was being rapidly etched away when the sample was placed in an aqueous environment compromising the integrity of the entire structure. Literature suggested using elevated temperatures and higher humidity to ameliorate this problem. However, it should be noted that increasing the temperature leads to the facilitation of Si-O-Si bonds releasing the amine groups, which leads to reduction in the quantity of binding sites. Therefore, we conducted experiments to ascertain the appropriate temperature at which we would have sufficient intensity for amine groups in FTIR spectra as well as reduced etching. As shown in Fig 4. 7, the monoliths functionalized at 80 ºC, exhibit a stronger signal for amine groups, as evidenced by the increase of the characteristic signal from primary amines, i.e. the NH stretch band at ~3300 cm^{-1} and NH bend at ~1600 cm^{-1}. Also, negligible column etching was observed at 80 ºC and thus silanization was carried out at 80ºC.

The process of silanization is also influenced by the presence of moisture as described in several works [8], generally the effect was found to be positive. Furthermore, it is possible that increasing the concentration of the silane precursor (APTES) might improve the overall quantity of primary amines present in the column. There have also been previous reports [30] which state that the coating of APTES degrades over time in aqueous environments and the suggested solution was to make multiple coatings of APTES. Since we had 3 different parameters which could hypothetically influence each other as well as the overall result we planned a full factorial

experiment with 3 factors and 3 levels (as shown in Table A3. 1 in Supplementary Information) i.e., APTES concentration (1.5 M, 2 M and 3 M), humidity (0%, 68% and 98%) and number of coatings (1, 3 and 5). The amine concentration was chosen as the response and was determined using the ninhydrin method using crushed samples. Contour plots showing the effect of these parameters are shown in Fig 4. 8.

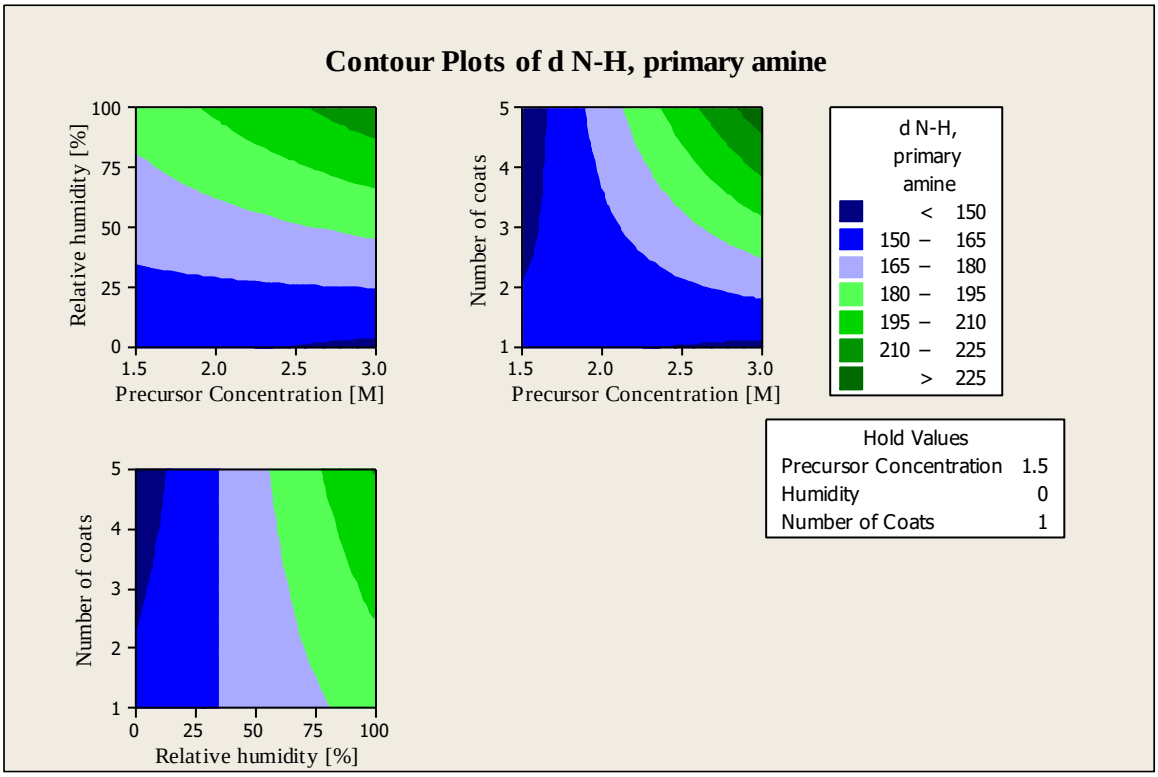

Figure 4.8. Contour plots showing the effects of humidity, APTES concentration and number of APTES coating layers on the NH2 content in monolith samples

It is visually clear that the optimal conditions (dark green) are 100% humidity, APTES concentration of 3M and 5 coating layers. Although, the columns that were functionalized with these conditions had significantly higher quantities of primary amines (172 µg/g of monolith) they also showed very high propensity for etching when in an aqueous environment. Some columns completely degraded within a few seconds crumbling into powder and releasing the APTES into the water. These features make columns prepared using these conditions unsuitable for protein purification, once proteins are mostly processed in aqueous systems. Since etching is not a quantifiable parameter, it was not possible to include this as a response in the experimental design (full factorial design) as a response. However, after screening all other samples from this experimental design, we arrived at a combination of 2 M APTES, 100% humidity and 1 APTES coating layer as a combination which showed the least amount of column degradation, while

having a slightly lower quantity of amines (166 µmol/g) than the predicted optimum. Hence, subsequent column functionalization was carried out at these conditions.

4.3.3. Evaluation of the performance of the functionalized alumina monolithic columns

The monoliths produced are highly porous, with an average porosity of around 60% and average pore diameter of around 1.8 µm (measured by mercury porosimetry as described in the previous work [5]). Generally, static adsorption experiments are carried out by immersing a sample in the solution containing the adsorbent and checking the change in concentration of the component over time. However, a monolith is a contiguous porous body and an aqueous solution might not permeate and wet the complete structure if it is just placed in a static solution. Hence, a system with a recirculating flow of the protein solution was designed and used to test the protein attachment. This system is not a dynamic adsorption study system; it rather simulates a stirred static adsorption experiment – this is advantageous, as we were able to contact the monoliths throughout its porous structure with the protein solution and thus, obtain a clearer idea about its attachment capacities.

The hydrodynamic behavior of fluids through the column were extensively evaluated in a work by the same authors [31]. Briefly using X-ray computed tomography, a small volume of the sample was digitally re-constructed as a 3D object (in STL format). The shear stress, pressure drop, velocity profile of a fluid flowing through this volume of column were simulated using computational fluid dynamics. The tortuosity of the fluid flow was calculated using a novel method, using the simulated stream-lines from the computed model (tortuosity ~1.1) and when compared to the methods used in literature it was found to be accurate (tortuosity calculated as per methods indicated in literature ~1.09). Additionally, it was observed (for the case of the monolith studied) that fluid transport was dominated by flow heterogeneities and advection, while the shear stress at pore mouths was significantly higher than in other regions. The residence time distribution of a pulse input of acetone through the length of the column was simulated by CFD and experimentally validated – the retention time was found to be < 30s. The next step was to test if the produced columns were suitable for protein attachment. One of conditions required for use of the produced columns as supports for chromatography is to have a high and stable binding of the specific ligand – an example of which is protein A. However, because of the expensive nature of protein A, BSA was initially used to test the propensity of the APTES-modified columns to feasibly attach proteins. Protein attachment studies with various concentrations of BSA were carried out and extensive work was performed which is out of the scope of this paper. One of the significant observations of the said work was that at lower feed concentrations there was stable chemical binding of BSA

to the amine groups in the column (up to 1 mg.mL^{-1}) – An example is shown in Fig 4. 9 with a feed of 0.5 mg/ml BSA concentration. The attachment appears to fit a Pseudo first order kinetic model as can be seen in the figure, suggesting that the rate is solely dependent on the BSA concentration.

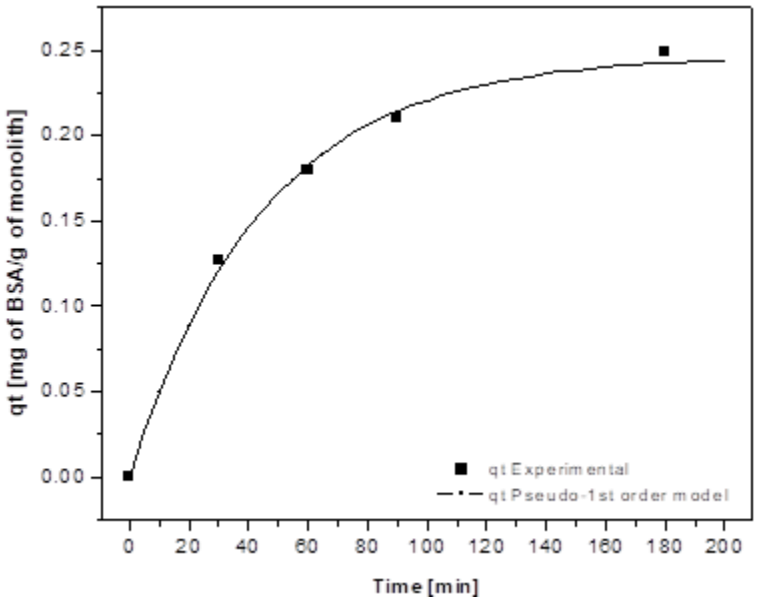

Figure 4.9. Attachment profile of BSA (0.5 mg/mL) to APTES modified alumina column
Legend: Symbols (■) indicate the measured values of qt and the line shows the calculated values of qt as per Pseudo 1st order model

These results indicate that the amine modified columns can successfully attach/bind proteins – leading to the possibility to showcase the use case of applying these columns as affinity chromatography columns for separation/purification of IgG. Subsequently, some basic adsorption experiments were carried out using Protein A bound modified monolithic columns to demonstrate the potential use of these columns.

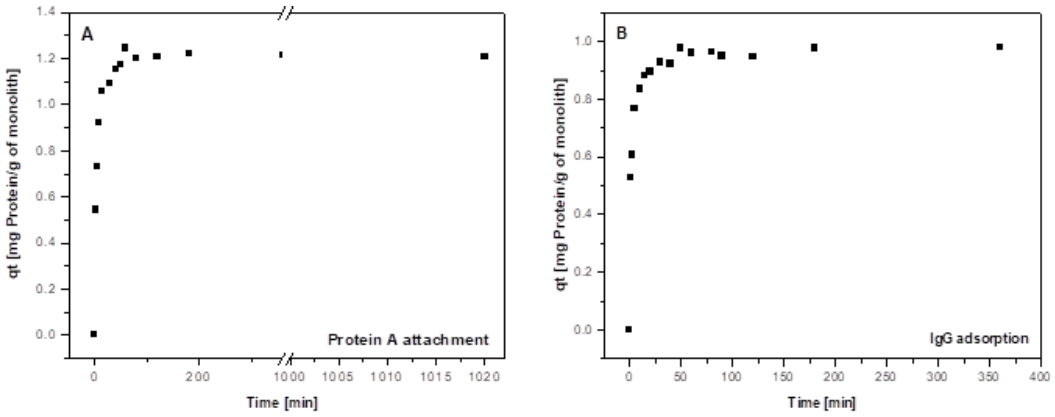

Figure 4.10. Protein A binding to the amine functionalized alumina monolith and B) IgG adsorption to the Protein A bound column

The above figure (Fig. 4. 10 A) shows the binding profiles of Protein A to the functionalized monolith. The experiment was conducted with an initial protein concentration of 1.0 $mg.ml^{-1}$. The experiments were run for a total of 17 hours at a flowrate of 0.467 $ml.min^{-1}$, followed by washing with phosphate buffer (PB) at a pH = 7.4 without recirculation to remove any free proteins, which was subsequently followed by another round of washing with PB with recirculation for 60 minutes. After the final washing with PB, the amount of bound protein A was measured to be 0.98 mg/g of monolith. Negligible protein detachment was observed after the phosphate buffer (pH = 7.4) washing steps.

Subsequently, the remaining possibly active attachment sites were nullified using BSA (0.5 $mg.ml^{-1}$) re-circulating it at the same flowrate. Two rounds of PB washing (the same as with Protein A) were carried out for BSA as well. After all the washing steps, it was found that about 23% BSA (with respect to the column weight) still attached to the column negating all possible non-specific binding sites. Thus, it was assumed that all the accessible active amine sites have been saturated with the BSA.

Stability tests were conducted to check the attachment of the protein to the column at various conditions. The principle was that since the pI value of Protein A is in the range of 4.85-5.10 and that of the amine groups of APTES is close to 11, if the attachment is just electrostatic interaction then we should be able to elute out most of the protein by using buffers of less than 4.85 or more than 11. The process was carried out for 19 hours with 2 mL of Glycine-HCL (pH=3.1) and Glycine-NaOH (pH=11.67) with PB (pH=7) washes in between. The resultant solution was treated with acetone precipitation to remove salts which could affect the BCA tests and the protein

concentration was estimated. In all the tests we were able to dislodge a maximum of 10-13% of the attached protein. This shows that the protein was very stably attached.

Subsequently, to check if the protein is attached due to other weak interactions like hydrogen bonds, the column was eluted with buffer solutions with ionic strengths of 5mM and 0.1 M NaCl at a temperature of 50 ˚C. We observed that in this case less than 5% (by weight) of the protein was desorbed. Again, this showed that the protein was very stably attached to the column.

Furthermore, an experiment was carried out to test the adsorption of bovine IgG onto this Protein A-attached monolith as shown in Fig. 4. 10 B. The experiment was performed using IgG at concentration of 1 $mg.ml^{-1}$ in a 50 mM phosphate buffered saline (PBS, at pH = 7.4). It was found that about 0.97 mg of IgG adsorbed per g of column, i.e. the binding was 0.785 mg IgG/ mg of Protein A. Subsequently, when eluted using a 25 mM citrate buffer (pH = 3.5) about 0.79 mg of IgG was recovered after 5 hours of elution.

Based on these results it is clear that APTES suitably modified the column with stable attachment via covalent bonds to alumina and similarly stable attachment to Protein A through possible ionic interaction. Furthermore, a basic experiment using IgG shows that such a column can effectively use for affinity-based purification of immunoglobulins.

4.4. Conclusions

A modified single step method to functionalize alumina monolithic columns was developed based on the method previously described by Yamagushi et al [29] using sol-gel synthesis with APTES as the silane agent. This method resulted in functionalized alumina monoliths with a high content of NH_2 groups well distributed through the column. The sol-gel reaction conditions were optimized in terms of catalyst (pH), temperature, humidity, number of APTES coating layers and concentration of precursor (APTES). Basic pH (1M NaOH) was found to positively influence the functionalization process. The optimal conditions for column functionalization were found by using a full factorial experimental design approach combined with the experimental evidence for column etching in aqueous solution. The optimal functionalization conditions were set at 100% humidity and 1 coating layer of 2M APTES solution, which led to monoliths containing 166 µg of NH_2/g monolith.

Protein attachment studies have also shown that both BSA and Protein A (0.98 mg Protein A/g monolith) attaches strongly to the column. Further protein affinity binding experiments show that it is possible to favorably attach IgG (0.78 mg IgG/mg Protein A) and elute it with a suitable buffer.

These observations evidence the suitability of the functionalization method used in this work for the development of alumina chromatographic stationary phases for the purification of immunoglobulins.

Besides, this method offers simplicity and the required versatility for the preparation of alumina monoliths with different functionalization, depending on the terminal group(s) carried by the selected silanol modifying precursor, allowing the possibility of broadening the application spectrum of alumina monoliths.

References

[1] D. Josic, A. Buchacher, A. Jungbauer, Monoliths as stationary phases for separation of proteins and polynucleotides and enzymatic conversion, 752 (2001) 191–205.

[2] Z. Walsh, B. Paull, M. Macka, Inorganic monoliths in separation science: A review, Anal. Chim. Acta. 750 (2012) 28–47. doi:10.1016/j.aca.2012.04.029.

[3] N. Vitorino, J.C.C. Abrantes, J.R. Frade, Cellular ceramics processed by paraffin emulsified suspensions with collagen consolidation, Mater. Lett. 98 (2013) 120–123. doi:10.1016/j.matlet.2013.02.020.

[4] M.F. Sanches, N. Vitorino, J.C.C. Abrantes, J.R. Frade, J.B. Rodrigues Neto, D. Hotza, Effects of processing parameters on cellular ceramics obtained by paraffin emulsified suspensions, Ceram. Int. 40 (2014) 9045–9053. doi:10.1016/j.ceramint.2014.01.117.

[5] N. Nayak, N. Vitorino, J.R. Frade, A. V. Kovalevsky, V.D. Alves, J.G. Crespo, C.A.M. Portugal, Design of alumina monoliths by emulsion-gel casting: Understanding the monolith structure from a rheological approach, Mater. Des. (2018). doi:10.1016/j.matdes.2018.07.017.

[6] A.N. Cloud, S. Kumar, M. Kavdia, H.H. Abu-Safe, M.H. Gordon, Protein adsorption on low temperature alpha alumina films for surgical instruments, Thin Solid Films. 517 (2009) 5927–5930. doi:10.1016/j.tsf.2008.08.002.

[7] J.A. Howarter, J.P. Youngblood, Optimization of silica silanization by 3-aminopropyltriethoxysilane, Langmuir. (2006). doi:10.1021/la061240g.

[8] R.M. Pasternack, S.R. Amy, Y.J. Chaba, Attachment of 3- Aminopropyl triethoxysilane on Silicon Oxide Surfaces: Dependence on Solution Temperature, Langmuir. 24 (2008) 12963–12971. doi:10.1021/la8024827.

[9] F. Brothier, V. Pichon, Immobilized antibody on a hybrid organic-inorganic monolith: Capillary immunoextraction coupled on-line to nanoLC-UV for the analysis of microcystin-LR, Anal. Chim. Acta. 792 (2013) 52–58. doi:10.1016/j.aca.2013.07.019.

[10] H. Mansur, R. Oréfice, M. Pereira, Z. Lobato, W. Vasconcelos, L. Machado, FTIR and UV–vis study of chemically engineered biomaterial surfaces for protein immobilization, Spectroscopy. 16 (2002) 351–360. doi:10.1155/2002/183053.

[11] K.C. Popat, G. Mor, C.A. Grimes, T.A. Desai, Surface modification of nanoporous alumina surfaces with poly(ethylene glycol), Langmuir. (2004). doi:10.1021/la049075x.

[12] S.H. Hyun, S.Y. Jo, B.S. Kang, Surface modification of α-alumina membranes by silane coupling for CO_2 separation, J. Memb. Sci. 120 (1996) 197–206. doi:10.1016/0376-7388(96)00160-3.

[13] K.F. Du, S. Bai, X.Y. Dong, Y. Sun, Fabrication of superporous agarose beads for protein adsorption: Effect of CaCO3 granules content, J. Chromatogr. A. 1217 (2010) 5808–5816. doi:10.1016/j.chroma.2010.07.046.

[14] Y. Wu, T. Buranda, R.L. Metzenberg, L.A. Sklar, G.P. Lopez, Diazo coupling method for covalent attachment of proteins to solid substrates, Bioconjug. Chem. 17 (2006) 359–365. doi:10.1021/bc050278m.

[15] A. Nanci, J.D. Wuest, L. Peru, P. Brunet, V. Sharma, S. Zalzal, M.D. McKee, Chemical modification of titanium surfaces for covalent attachment of biological molecules., J. Biomed. Mater. Res. 40 (1998) 324–35. doi:10.1002/(SICI)1097-4636(199805)40:2<324::AID-JBM18>3.0.CO;2-L.

[16] N. Aissaoui, L. Bergaoui, J. Landoulsi, J.F. Lambert, S. Boujday, Silane layers on silicon surfaces: Mechanism of interaction, stability, and influence on protein adsorption, Langmuir. (2012). doi:10.1097/BOT.0000000000000580.

[17] M.E. McGovern, K.M.R. Kallury, M. Thompson, Role of Solvent on the Silanization of Glass with Octadecyltrichlorosilane, Langmuir. (1994). doi:10.1021/la00022a038.

[18] K.T. Queeney, Y.J. Chabal, M.K. Weldon, K. Raghavachari, Silicon oxidation and ultra-thin oxide formation on silicon studied by infrared absorption spectroscopy, Phys. Status Solid Appl. Res. (1999). doi:10.1002/(SICI)1521-396X(199909)175:1<77::AID-PSSA77>3.0.CO;2-F.

[19] K.T. Queeney, Y.J. Chabal, K. Raghavachari, Role of interdimer interactions in NH3dissociation on Si(100)-(2 × 1), Phys. Rev. Lett. (2001). doi:10.1103/PhysRevLett.86.1046.

[20] J.F. Moulder, W.F. Stickle, P.E. Sobol, Handbook of X-ray Photoelectron Spectroscopy, 1992nd ed., in: Perkin-Elmer, Phys. Electron. Div., 1992. doi:10.1002/sia.740030412.

[21] N.S. McIntyre, in D. Briggs and M. P. Seah (eds.), Practical Surface Analysis in Auger and X-ray Photoelectron Spectroscopy, in: John Wiley Sons, New York, 1983. doi:10.1016/S0039-9140(97)80038-0.

[22] E. Pretsch, P. Bühlmann, M. Badertscher, Structure determination of organic compounds: Tables of spectral data, 2009. doi:10.1007/978-3-540-93810-1.

[23] Thermo Fisher Scientific Pierce Protein, Protein Purification Technical Handbook, 2010. doi:http://dx.doi.org/10.1016/S1251-8050(99)80047-0.

[24] W. Yoshida, Y. Cohen, Ceramic-supported polymer membranes for pervaporation of binary organic/organic mixtures, J. Memb. Sci. 213 (2003) 145–157. doi:10.1016/S0376-7388(02)00521-5.

[25] W. Li, X. Zhou, J. Ye, Q. Jia, Development of a α-alumina-nanoparticle-functionalized porous polymer monolith for the enrichment of Sudan dyes in red wine samples, J. Sep. Sci. 36 (2013) 3330–3337. doi:10.1002/jssc.201300754.

[26] R. Malaisamy, L. Lepak, M. Spencer, K.L. Jones, Surface modification of porous alumina membranes by collagen layers: Performance and characterization, Sep. Purif. Technol.

115 (2013) 114–122. doi:10.1016/j.seppur.2013.04.051.

[27] R. Tedja, A.H. Soeriyadi, M.R. Whittaker, M. Lim, C. Marquis, C. Boyer, T.P. Davis, R. Amal, Effect of TiO2 nanoparticle surface functionalization on protein adsorption, cellular uptake and cytotoxicity: the attachment of PEG comb polymers using catalytic chain transfer and thiol–ene chemistry, Polym. Chem. 3 (2012) 2743. doi:10.1039/c2py20450a.

[28] K.L. Mittal, Silanes and Other Coupling Agents, 2007. doi:10.1163/ej.9789067644525.i-410.

[29] A. Yamaguchi, F. Uejo, T. Yoda, T. Uchida, Y. Tanamura, T. Yamashita, N. Teramae, Self-assembly of a silica–surfactant nanocomposite in a porous alumina membrane, Nat. Mater. (2004). doi:10.1038/nmat1107.

[30] E.A. Smith, W. Chen, How to prevent the loss of surface functionality derived from aminosilanes, Langmuir. (2008). doi:10.1021/la802234x.

[31] S. Pawlowski, N. Nayak, M. Meireles, C.A.M. Portugal, S. Velizarov, J.G. Crespo, CFD modelling of flow patterns, tortuosity and residence time distribution in monolithic porous columns reconstructed from X-ray tomography data, Chem. Eng. J. (2018). doi:10.1016/j.cej.2018.06.017.

CHAPTER 5

Understanding Protein Attachment to Amine Functionalized Alumina Monoliths

Manuscript under preparation: *N. Nayak, F. Militano, R. Mazzei, T. Poerio, L. Giorno, J. G. Crespo, C A. M. Portugal. 'Understanding Protein Attachment to Amine Functionalized Alumina Monoliths'.*

Chapter 5: Understanding Protein Attachment to Amine Functionalized Alumina Monoliths

Abstract

In the present study, attempts have been made to elucidate protein interactions with amine functionalized alumina monolithic columns considering Bovine Serum Albumin (BSA) as a model protein. Studies were carried out at varied BSA concentrations (0.5 to 10 $mg.mL^{-1}$) to understand the type of binding between the protein and the column. It was found that at lower concentrations there appeared to be a more reactive interaction while at higher concentrations, due to the formation of aggregates, the interaction seems to be a more multi-layered physical adsorption. Dynamic light scattering measurements further confirmed the presence of protein aggregation phenomena at higher protein concentrations due to the contact of the protein solution with the column. Using this data, appropriate strategies were used to bind Protein G to the column - a maximum of 1.43 mg Protein G/g of monolith (or 2.1 mg of Protein G/cm^3 of the monolith) was bound. Finally, a binding-elution experiment using bovine immunoglobulin G was conducted and was found that 73.4% (IgG/Protein G) could bind to the column and 86% of the bound IgG could be eluted using an appropriate buffer. This proved the potential of the amine functionalized monolith for further application as an Affinity Chromatography medium.

5.1. Introduction

Downstream processing, especially in the case of biologically active molecules, remains a tightrope walk between maintaining the integrity of the molecule, reducing wastage and economics.

Ever since the 1986 approval for Orthoclone OKT3 for therapy in prevention of kidney transplant rejection and considering the advances in pharmaceutical manufacturing technologies, the application of monoclonal antibody as highly specific therapeutics has grown significantly. It is predicted that the biopharmaceuticals market will be dominated by monoclonal antibody and related products including antibody fragments, antibody-drug conjugates and Fc-fusion proteins by 2020 [1] with over 70 different products.

In affinity chromatography, immobilized binding agents are seen to be used with various supports. In the past, particulate-based materials such as silica particles, agarose beads, glass beads and particulate supports prepared from several organic polymers have been utilized for this purpose [2-5]. Nevertheless, scientific community has witnessed an increasing interest for incorporating affinity chromatography with monolithic supports [5-10]. This blend has off late been referred to as affinity monolith chromatography, or AMC [8-10].

Since 1967, in the field of size-exclusion chromatography, poly (ethylene glycol methacrylate) based polymeric materials were commonly used as protein separation media [11]. Other early media also included polyurethane foams, that were often observed to have undesirably lower permeabilities and increased swelling in few solvents that were seen as a hindrance to be effectively used in HPLC [12-15]. Alternative media were explored which included those based on membranes or compressed polyacrylamide gels and macroporous disks [16-20]. Nevertheless, these materials still faced limitations in terms of lower capacities of samples and depended majorly on using specific solvents for their utilization [21].

Eventually, modern monoliths were developed as supports for affinity chromatography that seem to offer several advantages [5-10]. Some of advantages of using these supports included better efficiencies, lower back pressure requirement and increased permeability in comparison to particle-based supports. These characteristics are beneficial, specifically for affinity-based separations to operate at higher fluxes such as rapid flow-based immunoassays. Furthermore, high efficiencies are required for certain applications like high-throughput drug screening and chiral separations [7-10].

Co-polymers of ethylene dimethacrylate (EDMA) and Glycidyl methacrylate (GMA) are presently the most commonly available monoliths [18–20]. These monoliths are known to have a facile method of synthesis and can be modified to have a hydrophilic form with traits of lower non-specific binding for several biological agents. They also have fabrication flexibility in terms of pore sizes, surface areas and shapes. This property makes it particularly beneficial to adapt these supports with proteins that are known to be larger binding agents [8,10]. Moreover, several immobilization methods incorporate these types of monoliths. However, their main disadvantage as a support to be placed in an affinity monolith chromatography column is that it has a tendency to exhibit smaller surface area while comparing it to the traditional particulate supports or monoliths. Thus, the volume of binding agent to immobilize on a support is limited [7-10, 22-24].

Another alternative, namely agarose offers several advantages including its low non-specific binding for many biological matrices, higher stability for a broad pH range, its easiness in modifying it to immobilize several binding agents and its intrinsic property of larger pore size. Thus, for several years, agarose has been routinely incorporated as a support in traditional affinity chromatography [1,2,5]. Nevertheless, its major drawback to be utilized in those applications involving HPLC is that it is fragile and displays lower mechanical stability [1,5]. However, agarose can be crosslinked or blended with different polymers to harden it and thus, allowing itself to be incorporated in relatively high-performance separations [5].

Adding to these are the necessary considerations of sustainability and environmental impact, which are gaining importance each passing day. Presently, the need to have efficient systems for purifying active molecules like therapeutic proteins and peptides seems to outweigh the need for proper assessment and development of a strategy to ensure a reduced effect on the environment when using said methods. However, with ever growing concerns regarding their immediate impact, especially synthetics like polymers and how we dispose of them, it is quite probable that equipment used for separations will soon come under the scanner.

In the present work, the Affinity Monolith Chromatography (AMC) potential of previously fabricated and functionalized amine modified alumina monolithic columns was analyzed. Extensive protein binding studies were carried out, using Bovine Serum Albumin (BSA) as model protein, to understand the intricacies of the interaction between the column and protein and to check the binding capacity of the amine functionalized monolith. The attachment has been characterized in terms kinetics and the mechanism of binding has been speculated understand how a globular protein like BSA or Protein G might interact with the column. Binding stability was tested under conditions of stresses, like acidic and basic pH, high ionic strength and temperature. Subsequently, attachment with Protein G using two different concentrations have been tested. Finally, these Protein G columns were used to assess the binding and elution of Immunoglobulin G as a model system.

5.2. Materials and Methods

5.2.1 Materials

Alumina monoliths modified with (3-Aminopropyl)triethoxysilane, prepared previously [25, 26], were used for the studies (α-alumina from Alcoa Chimie, CT-3000, Dolapix PC 67 from Zschimmer & Schwarz, Gelatin Porcine Skin (Oxoid – LP0008) and sodium lauryl sulfate/SDS from Sigma-Aldrich L-6026, stock concentration of 1 $g.L^{-1}$ and commercially available corn oil, castor oil and margarine were used). Heat-shrink Teflon tubes were procured from an online store. Analytical grade di-sodium hydrogen phosphate and sodium di-hydrogen phosphate were used to prepare a Phosphate buffer (PB) of 50mM concentration with a pH = 7. A standard BCA test (reagents sourced from Thermo Fisher) was used to assess the protein concentrations. Bovine serum albumin, sourced from Sigma-Aldrich, Portugal, dissolved in the PB, was used in the experiments and also to construct the protein concentration calibration curve (Protein concentration = 1.016 x Absorbance@562nm). For the desorption, Glycine-HCl (pH=3.1) and Glycine-NaOH (pH=11) buffers at concentrations of 0.1M and 1M were used. Further, desorption

with 5mM NaCl and 0.1M NaCl was also studied. All reagents used were analytical grade. Fittings for the columns were obtained from Biotoolomics PLC., UK.

5.2.2 Fabrication of α-alumina monoliths

The alumina monolithic columns were prepared as described elsewhere [25]. Briefly, 50% volume alumina suspension was prepared in water. Dolapix was added as the de-coagulant. Emulsions were prepared using this suspension with corn oil ($V_{oil}/V_{suspension}$ = 1.5) with SDS as the surfactant and gelatin as the gelling agent. These emulsions were poured into cylindrical molds and once set were sintered with a specific thermal cycle. The sintered columns were further activated by immersing in H_2O_2 (incubated at 90 ˚C for 120 minutes) [26]. Subsequently they were modified using sol-gel method with APTES as the silane agent in ethanol with NaOH as the catalyst. The process was carried out in a 100% relative humidity environment at 80 ˚C for 150 minutes. Furthermore, the samples were dried for 16 hours at 60 ˚C. These columns were then chosen for further studies on Protein attachment.

5.2.3 Preparation of the monolith for the setup

The amine functionalized alumina monoliths were initially weighed (dry weight) and their size was measured (length and diameter) with a Vernier caliper. Then, they were inserted in the Teflon tubing and a short duration of heat was applied externally to the tube using a standard Bunsen burner to shrink the tube to tightly wrap around the monolith – making it water-tight around the sides. The HPLC fittings were then attached to the ends of the tube (as seen in Fig 5. 1).

Figure 5.1. Amine coated alumina monoliths encapsulated in Teflon heat-shrink tubes

The setup was assembled as seen in the schematic representation in Fig 5. 2 and in final form in Fig 5. 3. The heat-shrink Teflon tube wrapped monoliths, modified with APTES, were connected to 5 ml reservoirs containing the protein solution, through a peristaltic pump. This configuration of

the setup was used to ensure the complete wetting of the highly porous monoliths. Standard HPLC fittings were used for the connections. The pumps were calibrated before each run and the final flow rates were also checked after each attachment cycle.

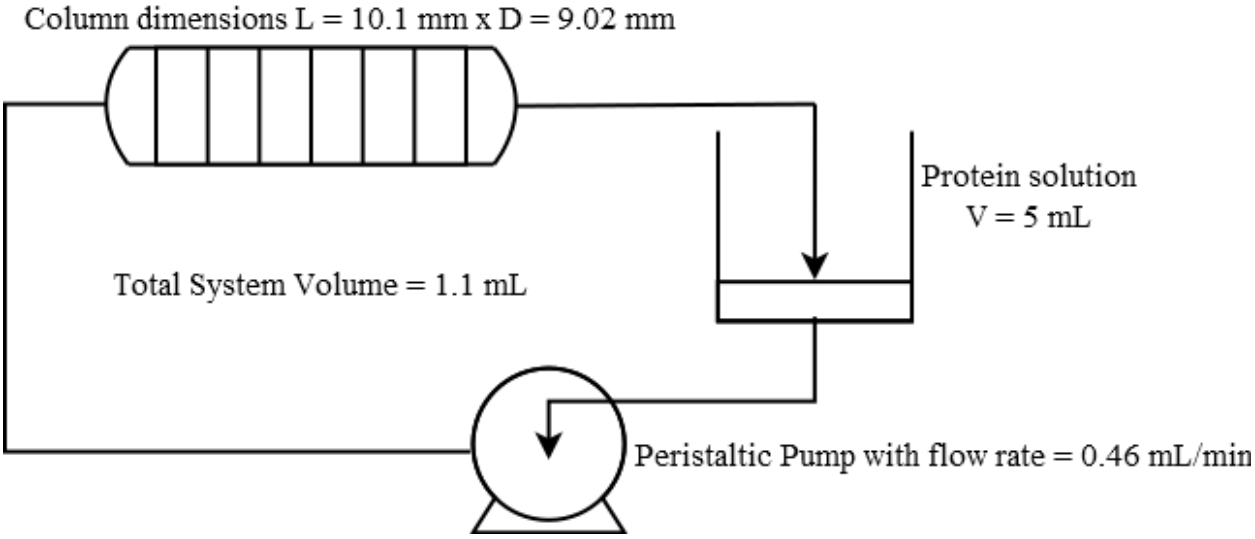

Figure 5.2. Schematic representation of process setup

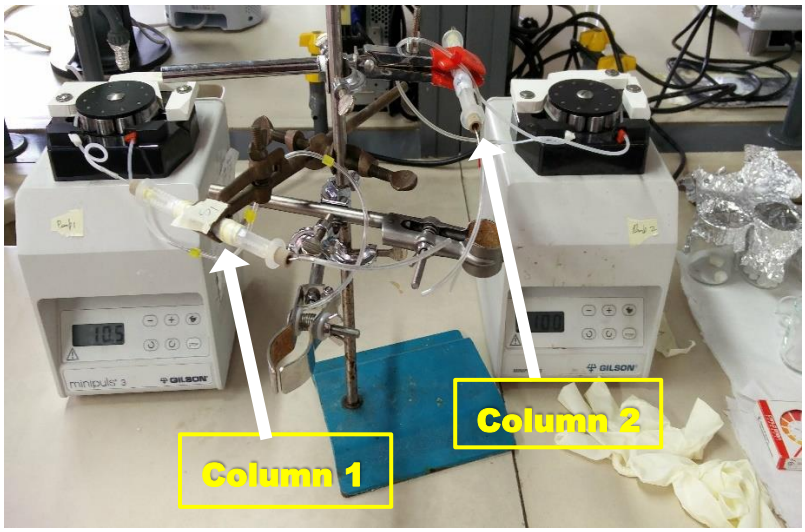

Figure 5.3. Process setup used for the experiments

5.2.4 Protein attachment and kinetics:

Protein attachment to the functionalized columns was testing using BSA as it is known to bind to amine groups. The column was initially equilibrated by re-circulating 5 ml of 50 mM Phosphate buffer (pH=7.4) for 1 hour. Next, 5 mL of the protein solution (BSA/Protein G) was taken in the

reservoir. The pump was set to a flow rate of 0.467 mL.min^{-1}. Time was recorded as soon as the column was filled. Samples (100 µL) were taken every 30 minutes for the first 3 hours, for protein quantification and to access the mass of protein attached to column along time. So, in all about 0.7 ml of sample was removed from the 5 ml reservoir. This was taken into account for the calculations. After 3 hours, the process was stopped, the column was emptied and a rapid wash with 5 ml of fresh buffer was carried out, without re-circulation. Subsequently, a re-circulated wash with fresh buffer (PB) was carried out for a further 1.5 hours, to remove the unbound proteins.

The experiments were carried out for initial BSA concentrations of 0.5, 1.0, 1.5, 3.0, 5.0 and 10.0 mg.mL^{-1}.

The obtained protein adsorption data [mg of protein.g of column^{-1} vs. time] were fit to the pseudo first order and pseudo second order kinetics equations shown below:

Table 5.1. The names and non-linear forms of studied kinetic models

Pseudo-first order	$q_t = q_e[1-\exp(-k_1 t)]$
Pseudo-second order	$q_t = \frac{k_2 q_e^2 t}{1+k_2 q_e t}$

Where, k_1 is the rate constant for the pseudo-first order adsorption; k_2 is the rate constant for the pseudo-second order adsorption; q_t corresponds to the absorption capacity at given time '*t'.*

Additionally, the obtained protein adsorption data were also fit to the following isotherms:

Table 5.2. The names and non-linear forms of studied two and three parameter isotherm models

Two parameter isotherms	
Langmuir	$q_e = \frac{Q_m K_a C_e}{1+K_a C_e}$
Freundlich	$q_e = K_F C_e^{1/n_F}$
Tempkin	$q_e = \frac{RT}{b_T}\ln(k_T C_e)$

Where, Q_m is the maximum adsorption capacity; C_e is the equilibrium concentration of solute (BSA/Protein G) K_a is the Langmuir constant; K_F, n_F are the Freundlich constants; b_T, k_T are the Tempkin constants; R corresponds to the universal gas constant; T is the absolute solution temperature (in Kelvin).

Subsequently, using the same setup, temperature and buffer conditions Protein G was used as the ligand and bound to the column with concentrations of 0.7 and 1.0 $mg.ml^{-1}$.

5.2.5 Stability of Protein Binding

The binding stability of the proteins to the amine-based columns were tested by various methods of dissociation described as follows:

Desorption using Glycine-HCl and Glycine-NaOH (0.1 M and 1 M)

Separate experiments were carried out using Glycine - HCl buffer at a pH of 3.1 and Glycine-NaOH buffer at pH = 11. Briefly, the buffer was taken in the reservoir and the experiment was carried out at flow rate of 0.467 $ml.min^{-1}$ for 19 hours. A sample (control) was taken at the beginning of the experiment and a final sample was collected after 19 hours.

As the pH of these buffers are at extremes (3.1 and 11) the samples had to be treated to precipitate and re-dissolve the protein before carrying out the estimation. This was done using acetone precipitation as recommended by Thermo Fisher [27].

Desorption using NaCl (5 mM and 0.1 M) and temperature

Saline solution (2 ml) with varying ionic strength (5 mM and 0.1 M) was taken in the reservoir and the experiment was carried out at flow rate of 0.467 $ml.min^{-1}$ for 19 hours. A sample (control) was taken at the beginning of the experiment and a final sample is collected after 19 hours. Additionally, an experiment was carried out at temperature of 50 ˚C also for each concentration.

Quantification of the total protein attached or entrapped in the monolith

To evaluate the total protein trapped in the column after all the stability tests were carried out, the column was crushed to a fine powder using a mortar and pestle. The protein content in this ground powder was quantified using the BCA test: 0.1 g of the powder was taken in a test tube and the protein was estimated using the standard BCA test kit. For the blank, 0.1g of pure alumina powder was used and amine functionalized alumina without protein attached was used as the control.

5.2.6 Protein attachment and aggregation by dynamic light scattering

The particle size distribution and polydispersity *PDI* of the samples were measured using a NanoZetaSizer particle size analyser (Malvern instruments, ZS 90, UK). The software used to collect and analyse the data was ZetaSizer Sofware 7.1 provided with the instrument. The samples measured were done at a controlled temperature of 25°C.

Dynamic Light Scattering (DLS) technique was used to measure the protein solution size distribution and polydispersity *PDI* of the sample. This technique measures the diffusion of particles subjected to Brownian motion, and by using Stokes-Einstein relationship, the motion of particles is converted to its size and size distribution. It incorporates non-invasive back scattering angle of 173˚ and allows the detection of droplets in the range of 0.6-6000 nm. All studies were repeated thrice, and the values of the z-average diameters were used.

5.2.7 Binding studies with IgG

The effectiveness of the attachment of Protein G to the amine-based columns for use in affinity chromatography was tested using Immunoglobulin G.

Initially, the column was equilibrated by re-circulating 5 ml of PB (pH=7) for 1 hour. To study the adsorption of IgG, 5 ml of the solution was taken in the reservoir. The pump was set to a flow rate of 0.467 ml.min^{-1}. Time was recorded as soon as the column filled. Samples (100 µL) were taken every 30 minutes for 3 hours. So, in all about 0.6 ml of sample was used for analysis from the 5 ml reservoir. This volume change is compensated accordingly in the calculations. After 3 hours, the process was stopped, column was emptied and a rapid wash with 5 ml of fresh buffer was carried out, without re-circulation to remove the unbound proteins. Subsequently, a re-circulated wash with fresh buffer (PB) was carried out for a further 1.5 hours to equilibrate the column.

The elution of IgG was performed using a 25 mM citrate buffer at pH 3.5 under the same conditions as above.

5.3 Results and Discussions

Considering that our goal was to ensure stable binding of proteins to the amine modified columns it was decided to determine the optimal concentration of protein required to achieve maximum possible adherence to the modified column, while avoiding wastage or loss. To determine this, it was decided to use bovine serum albumin (BSA, pI = 4.7, molecular weight = 66.5 kDa) given the fact that it is structurally quite similar to Protein G (pI = 3.7 – 4.4, mol weight = 22-34 kDa) and is

known to be used to eliminate non-specific binding sites in home-made columns [28-30]. There are many reported mechanisms for the attachment of BSA to the amine groups [31], the best possible conditions would need to be provided for the binding to proceed favorably. In the present case, as the isoelectric point (pI) of BSA is described in literature to be ~4.8 [32] while the pKa of APTES is described to be ~11.4, the ideal binding conditions would be in the range between these two pI values. Most proteins thrive in solutions of pH as close as possible to that in physiological media – therefore, phosphate buffer (50mM) at a pH =7.4, was used in the subsequently described experiments ensuring that the amine groups on the column surface remained protonated, while the BSA was negatively charged.

Experiments were carried out using different concentrations of BSA (0.5, 1.0, 1.5, 3, 5 and 10 $mg.mL^{-1}$). The solution was re-circulated through the column and samples were taken at fixed intervals up to a period of 3 hours. These data were used to analyse the kinetics of the reaction between the column and BSA. The data obtained were fitted to two different rate equations – a first order model and a pseudo-second order model. The parameters of the fitting and the obtained constants are shown in the table below (Table 5. 3 and Fig 5. 4).

Table 5.3. Experimentally determined and theoretically predicted parameters for absorption kinetics models

Where, Q_{expt} – experimentally determined amount of adsorbate [mg of protein/g of monolith]; Q_{pred} – mathematically predicted amount of adsorbate [mg of protein/g of monolith]; k_1 [min^{-1}] and k_2 [g/mg-min] are the pseudo-first order kinetic model and pseudo-second order kinetic model constants; χ^2 is Chi-square test constant and R^2 is the regression constant.

Initial Concentration [$mg.ml^{-1}$]	Q_{expt} [$mg.g^{-1}$]	Pseudo First order				Pseudo Second order			
		Q_{pred} [$mg.g^{-1}$]	k_1	R^2	χ^2	Q_{pred} [$mg.g^{-1}$]	k_2	R^2	χ^2
0.5	0.249	0.242	0.0224	0.99	0.00056	0.261	0.137	0.989	0.0033
1	0.276	0.319	0.0105	0.925	0.022	0.4605	0.0175	0.928	0.02
1.5	1.395	1.374	0.0374	0.997	0.003	1.474	0.0466	0.989	0.016
3	1.887	0.938	0.783	0.425	1.803	7.588	0.0003	0.988	0.025
5	2.2388	0.6775	0.7827	0.275	3.729	9.354	0.0004	0.905	0.434
10	5.333	3.208	0.7827	0.521	4.332	11.299	0.0005	0.964	0.229

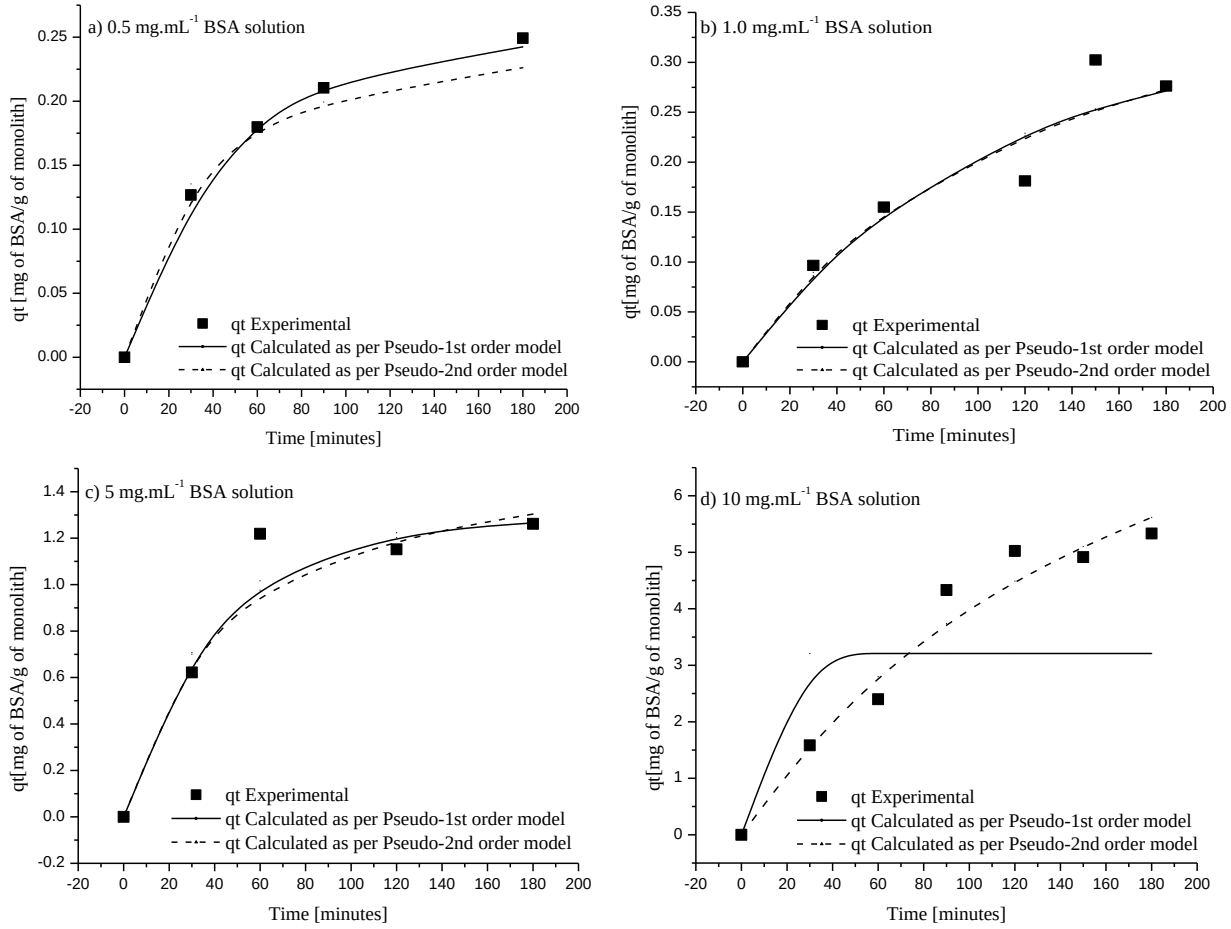

Figure 5.4. Binding data fit to kinetic models for concentrations a) 0.5 mg.mL^{-1} BSA b) 1.0 mg.mL^{-1} BSA c) 5 mg.mL^{-1} BSA d) 10 mg.mL^{-1} BSA

The data indicate that the changes in attachment over time for different initial concentrations of BSA (0.5 and 1.0 mg.ml^{-1}) which shows that at lower concentrations the tendency was towards a Pseudo-first order kinetic model. The reaction constant k_1 for the first order models and k_2 for the pseudo second order model are proportional to the energy of activation/bonding and indicates the energy dissipated due to the reaction [33]. Considering that at lower BSA concentrations (0.5 and 1.0 mg.mL^{-1}) the data fits better to the 1st order model and at higher BSA concentrations (3, 5 and 10 mg.mL^{-1}) the data fits better to the pseudo second order model. Furthermore, fitting of the data at higher BSA concentrations to the pseudo - second order kinetic model, suggests that the binding increases proportionally twice for every unit increase in BSA concentration. This model is typically used to describe adsorption phenomena and therefore it appears that as the concentration is increased the attachment switches to adsorption.

To understand this further, the data were fit to the most commonly known adsorption isotherms namely: Langmuir, Freundlich and Tempkin models. As can be seen in the below Fig. 5. 5, at concentrations below 1.5 mg.mL^{-1}, there seems to be no fitting to any isotherm, which is suggestive of the fact that the dominant process might not be adsorption in this concentration range. However, as the concentration increases above 1.5 mg.mL^{-1} it appears that the data fits into certain adsorption isotherms indicated below (Table 5. 4).

Table 5.4. Isotherm parameters determined through fitting of absorption data for BSA solutions with concentrations higher than 1 mg.mL^{-1}

Where, Q_m is the maximum amount of protein absorbed in a monolayer on the monolith surface [mg of protein/g of monolith]; K_a is the Langmuir isotherm constant related to the affinity of the binding sites [mg/mL]; K_F and n_F are Freundlich isotherm constants related to capacity and intensity of adsorption, respectively; K_T is the Tempkin isotherm constant [mL/mg] and b_T is the constant related to the heat of sorption [J/mol]; χ^2 is Chi-square test constant and R^2 is the regression constant.

Langmuir		Freundlich		Tempkin	
Q_m	429.5	K_F	0.85	K_T	1.39
Ka	0.00192	n_F	1.02	b_T	1194.86
χ^2	0.63	χ^2	0.62	B	2.11
R^2	0.92	R^2	0.92	χ^2	1.48
				R^2	0.72

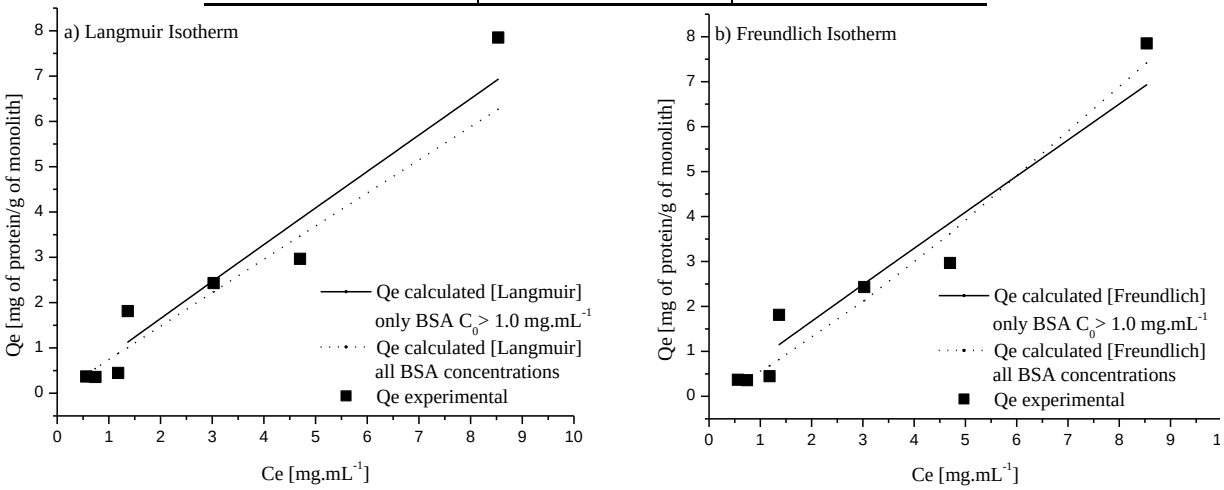

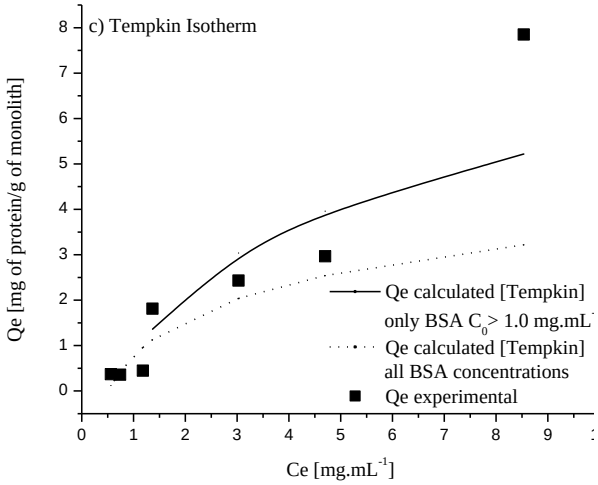

Figure 5.5. Fitting of BSA adsorption data at concentrations higher than 1.0 mg.mL^{-1} to a) Langmuir, b) Freundlich and c) Temkin isotherms

The values of the maximum adsorption amount (Q_m), correlation coefficient (R^2), chi-square (χ^2) and the other parameters for all the isotherms are shown in Table 5.4. The Langmuir isotherm [34] assumes that adsorption occurs on a homogeneous surface containing sites with equal energy and that are equally available for adsorption. This is valid for the complete monolayer of adsorption, on which there is no transmigration of adsorbate on the surface plane. An R^2 value of 0.92 shows passable fitting of this isotherm to the experimental data at higher BSA concentrations (Fig. 5. 4a). The separation factor ($R_L = 1/(1+K_a*C_0)$), an important parameter of the Langmuir isotherm, can be used to verify if the adsorption in the system studied is unfavorable ($R_L > 1$), linear ($R_L = 1$), favorable ($0 < R_L < 1$), or irreversible ($R_L = 0$). For the concentration range studied (0.5, 0.75, 1.0, 1.5, 3.0, 5.0 and 10.0 mg.L^{-1}), the respectively obtained values of 0.999, 0.999, 0.999, 0.998, 0.996, 0.994, 0.988 indicate borderline favorable adsorption of BSA to the monolith.

The Freundlich isotherm [35] is an empirical equation that can be used for heterogeneous systems, which besides protein-material interactions also considers interaction between adjacent adsorbed molecules. The n_F parameter, known as the heterogeneity factor, can be used to indicate whether the adsorption trend is linear ($n_F = 1$) and whether it is a chemisorption ($n_F < 1$), or physisorption ($n_F > 1$) process [36]. On the other hand, if the value of $1/n_F < 1$ it indicates that the process follows a cooperative binding trend and for values of $1/n_F > 1$ it follows a multi layered binding trend. The values of $n_F = 1.02$ and $1/n_F = 0.98$ indicate that the physical process and borderline multilayered binding are favorable. The fitting of the Freundlich isotherm to the experimental data ($R^2 = 0.92$) is shown in Fig. (5. 4b). Like the Freundlich isotherm, the Tempkin isotherm [37] considers the interactions between adsorbate molecules assuming that the adsorption heat of all molecules decreases linearly after the layer that is initially adsorbed on the

monolith surface is covered (i.e. the second protein layer) and that the adsorption has a maximum energy distribution of uniform bond. The constant b_T is the Tempkin isotherm constant, and this value can be used to calculate the value of heat of adsorption, $B = RT/b_T$, where R is the universal gas constant (value = 8.314 $J.K^{-1}.mol^{-1}$) and T is the temperature in kelvin [K]. Thus, we can find the heat of adsorption B = 2.11 kJ/kmol which is a low value indicating that the adsorption is mainly a physical phenomenon. The fit to experimental data ($R^2 = 0.72$) in Fig. (5. 4c) shows that the Tempkin isotherm is quite adequate to explain the adsorption of BSA onto the amine modified monolith along with the Freundlich isotherm.

To understand the behavior of BSA at higher concentrations, analyses of the particle size changes in the BSA with respect to concentration as well as contact time with the monolith while recirculating (simulated stirring). For freshly prepared solutions (see Fig. 5. 6 (a) and (b)) a bimodal distribution was observed for all concentrations. As the concentration of BSA increased, above $1mg.ml^{-1}$, the larger peak shifts to the right i.e. corresponding to the formation of larger particles, while the peak for the smaller particles (~10 nm) is still predominant. This is indicative that in highly concentrated solutions of BSA aggregation phenomena start to occur. With increased concentration, larger particles are formed.

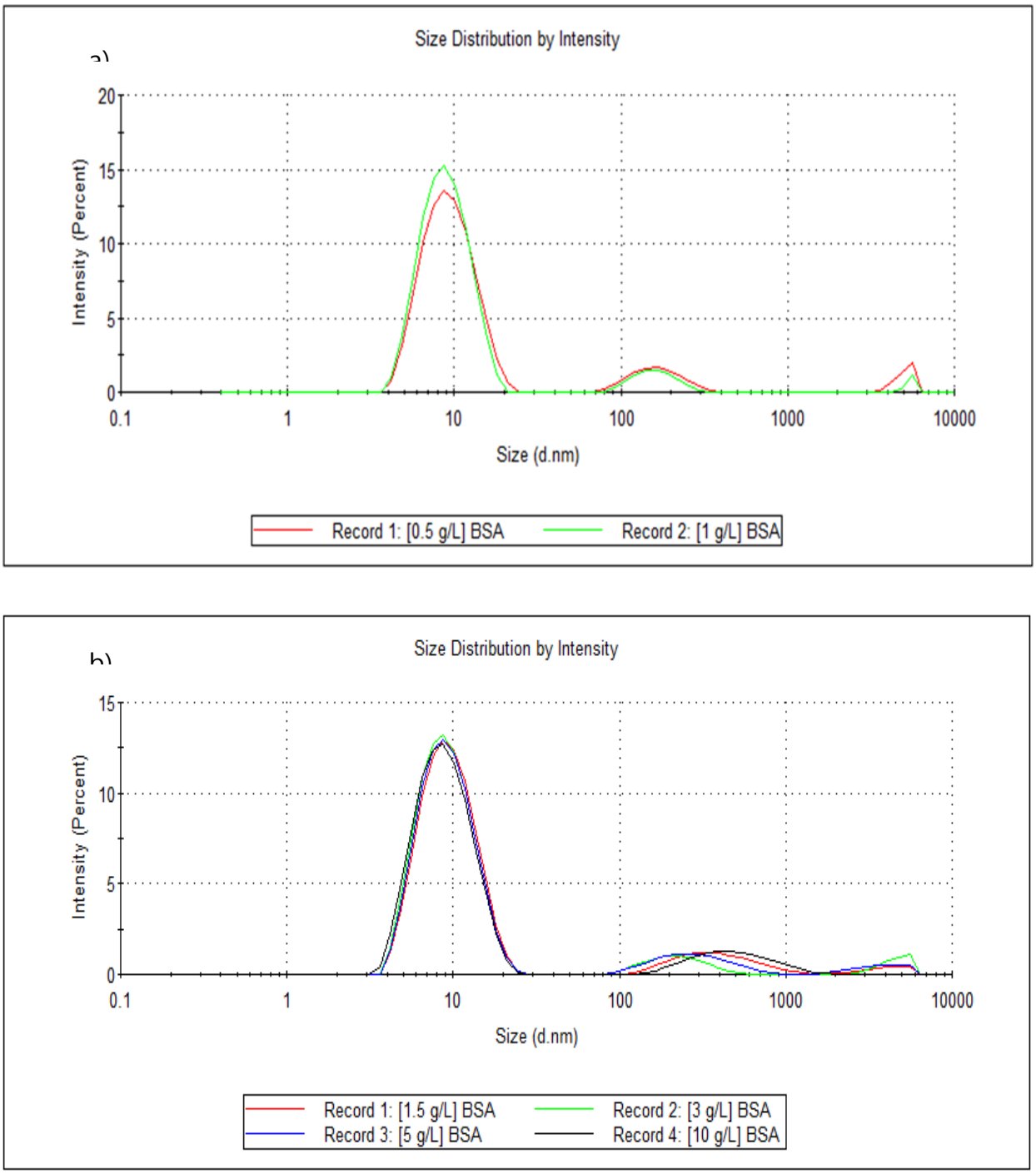

Figure 5.6. Particle size distribution at (a) lower concentrations of BSA, (b) higher concentrations of BSA

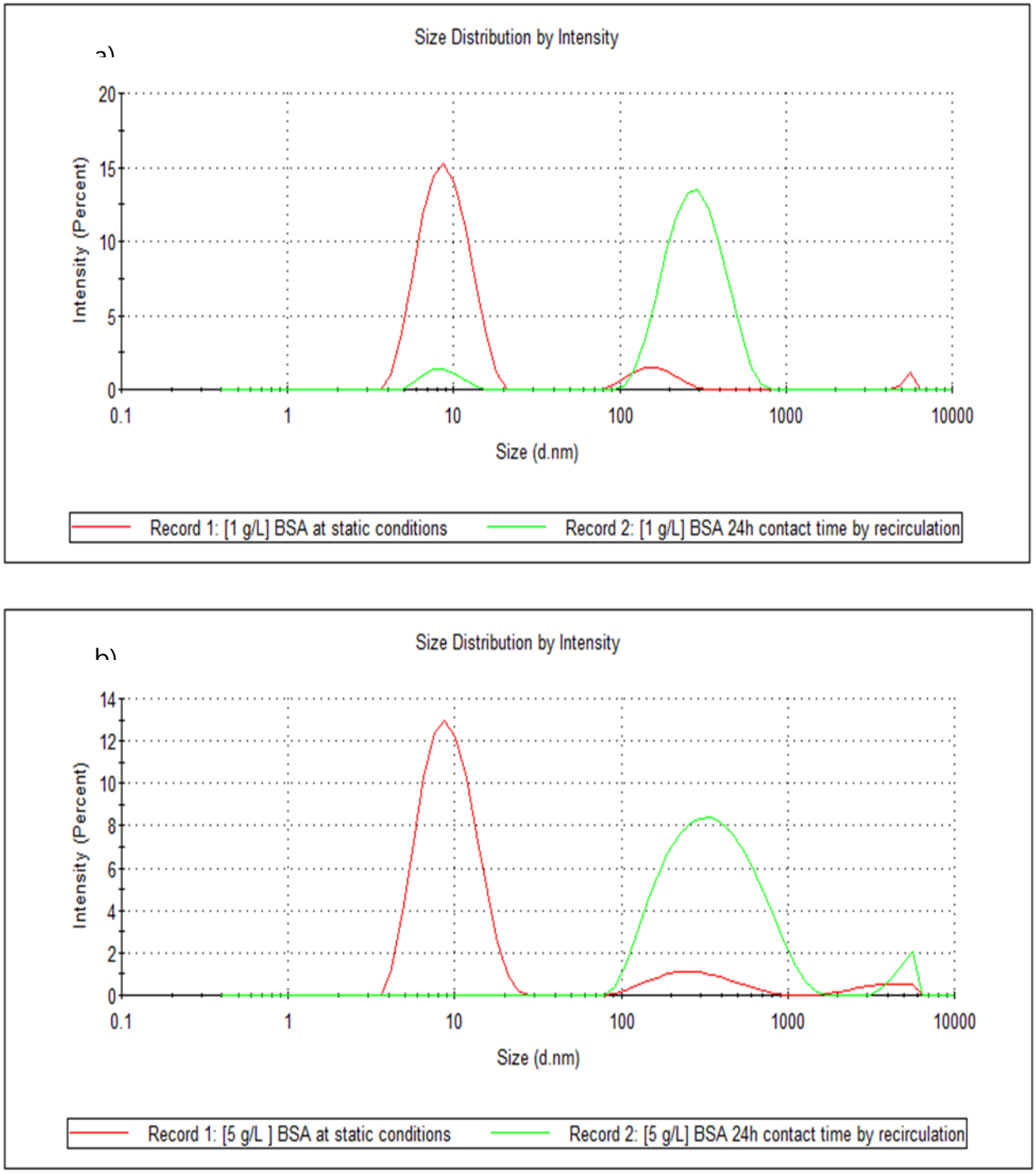

Figure 5.7. Effect of contact time with monolith while recirculation on particle size of BSA solution at (a) 1 mg.mL^{-1} and (b) 5 mg.mL^{-1}

The particle size distributions are shown in Fig 5. 7 (a and b). They clearly show a shift in the population of particle sizes from a higher population of ~10nm particles to a higher population of 100-1000 nm particles, with increasing contact time with the column. This behavior was even

more significant in the case of solutions of higher BSA concentration (the BSA solution with a concentration of 5mg.ml^{-1} is indicated here as an example). In fact, here the monomers appear to be in negligible quantity. The shift to the right shows that the Brownian motion is more sluggish indicating the presence of larger and heavier particles. Based on these observations it could be hypothesized that the observed “layer upon layer” attachment may just be the attachment of large and heavy aggregates to possible free attachment sites in the monolith, at higher BSA concentrations

It appears that BSA attachment to the column may be more complicated than expected. From the standpoint of applications, it is crucial that the attachment of protein-monolith is stable. Therefore, stability tests were conducted to check the attachment of BSA to the column, under diverse conditions. As it was assumed that the pI of BSA, APTES and buffer pH play key roles in the attachment of BSA to the column, it was imperative to determine if the attachment was just governed by an electrostatic interaction – in which case it should be possible to elute most of the protein by using buffers with pH < 4.85 or pH > 11. Experiments were carried out for 19 hours with 2 mL of Glycine-HCL (pH=3.1) and Glycine-NaOH (pH=11.67) respectively with PB (pH=7) washes in between. The resultant solution was treated with acetone precipitation [27] to remove salts for protein quantification by BCA assay, since the presence of salts could affect the BCA tests. In all the tests we were able to dislodge a maximum of only 8-10% of the attached protein. Not considering the functionality, this result shows that the protein attachment itself was very stable.

Subsequently, to check if the protein is attached due to other weak interactions like hydrogen bonds, the column was eluted with buffer solutions with ionic strengths of 5mM and 0.1 M NaCl at a temperature of 50 ˚C. In this case, it was observed that less than 5% (by weight) of the attached protein was desorbed. Again, this showed that the protein was very stably attached to the column.

To confirm that the attached protein was indeed entrapped in the column – the material was crushed, and protein estimation was performed using the resultant powder (using the BCA test). It was found that all the un-detached BSA was indeed present within the column – confirming without doubt that the protein was very stably attached to the column.

Considering these results with BSA, it is suggested that to avoid aggregation and ensure that the column is optimally functionalized with ligands – in this case Protein G – lower concentration solutions must be used in the functionalization process. This is ideal as it will avoid wastage of

the expensive Protein G. Subsequently, studies were carried out with 0.7 and 1 mg. mL^{-1} solutions of Protein G.

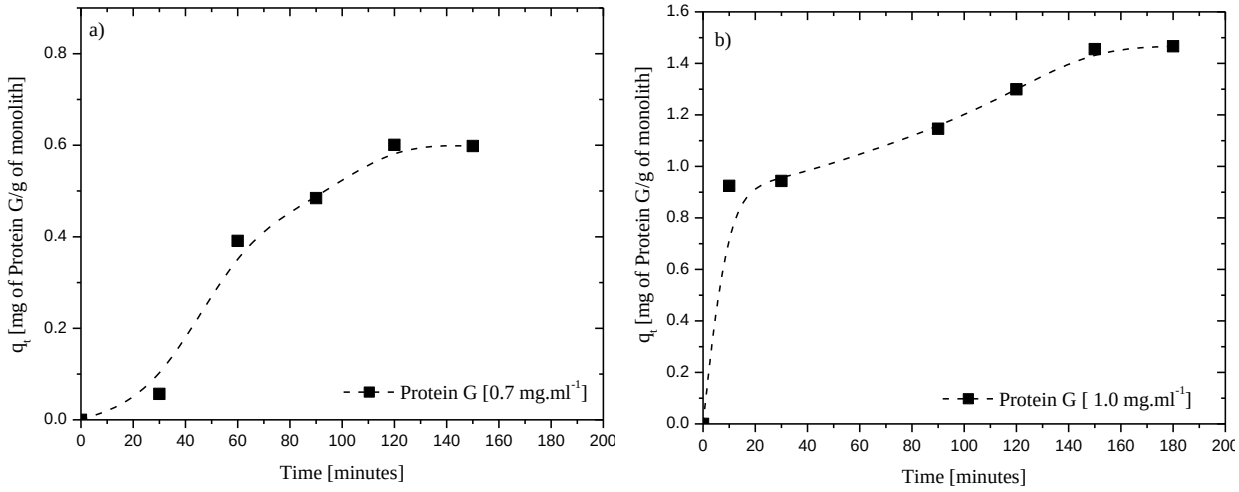

Figure 5.8. Studies with Protein G a) 0.7 mg.mL^{-1} Protein G b)1.0 mg.mL-1 Protein G

The above figure (Fig. 5. 8 a) and b)) shows the kinetics of attachment of Protein G. The experiment was conducted with an initial Protein G concentration of 0.7 and 1.0 mg.ml^{-1} and the experiment was run for a total of 3 hours. The final binding was measured to be 0.61 mg/g of monolith (0.91 mg of Protein G/cm^3 of monolith) in the case when the Protein G solution of 0.7 mg.mL^{-1} was used and 1.43 mg/g of monolith (2.1 mg Protein G/ cm^3 of monolith) when 1.0 mg.mL^{-1} was used. Unlike with BSA, where traces of protein detachment in the PB washing steps were observed, here there was negligible detachment.

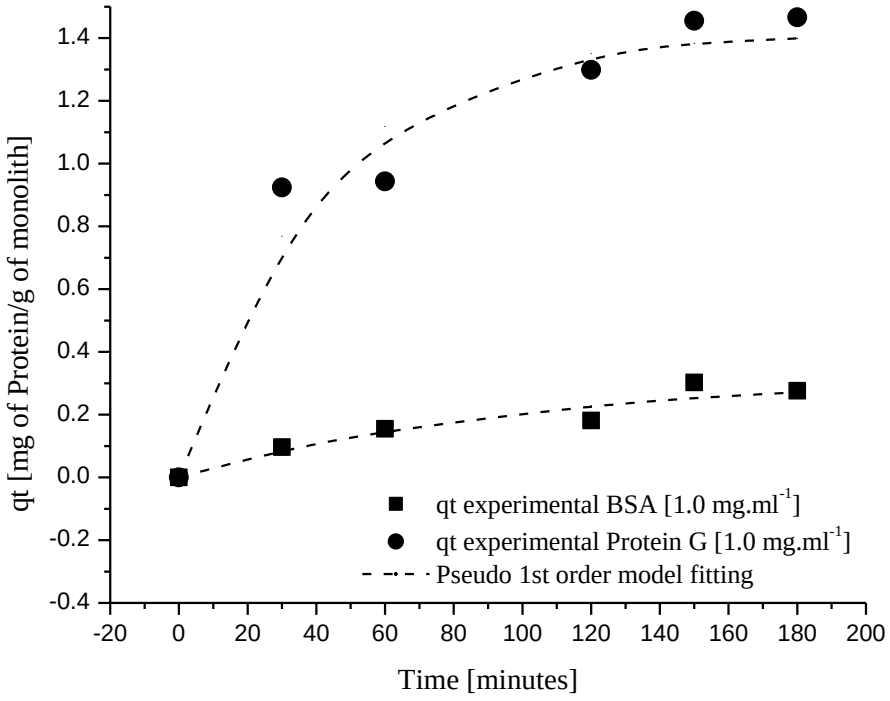

Figure 5.9. Comparison of binding of BSA vs Protein G at a concentration of 1 mg.ml^{-1} to amine functionalized alumina column

A significant increase in the amount of bound protein was observed as Protein G is about half the size of BSA as can be seen in Fig 5. 9. Subsequently, the nullification of possible unattached active sites was performed using BSA (0.5 mg.ml^{-1}) re-circulating it at the same flowrate of 0.467 ml.min^{-1}. After all the washing steps, it was found that about 2.5% BSA (with respect to column the weight) still attached to the column. This ensured that all the active amine sites (accessible to BSA) have been saturated with the BSA.

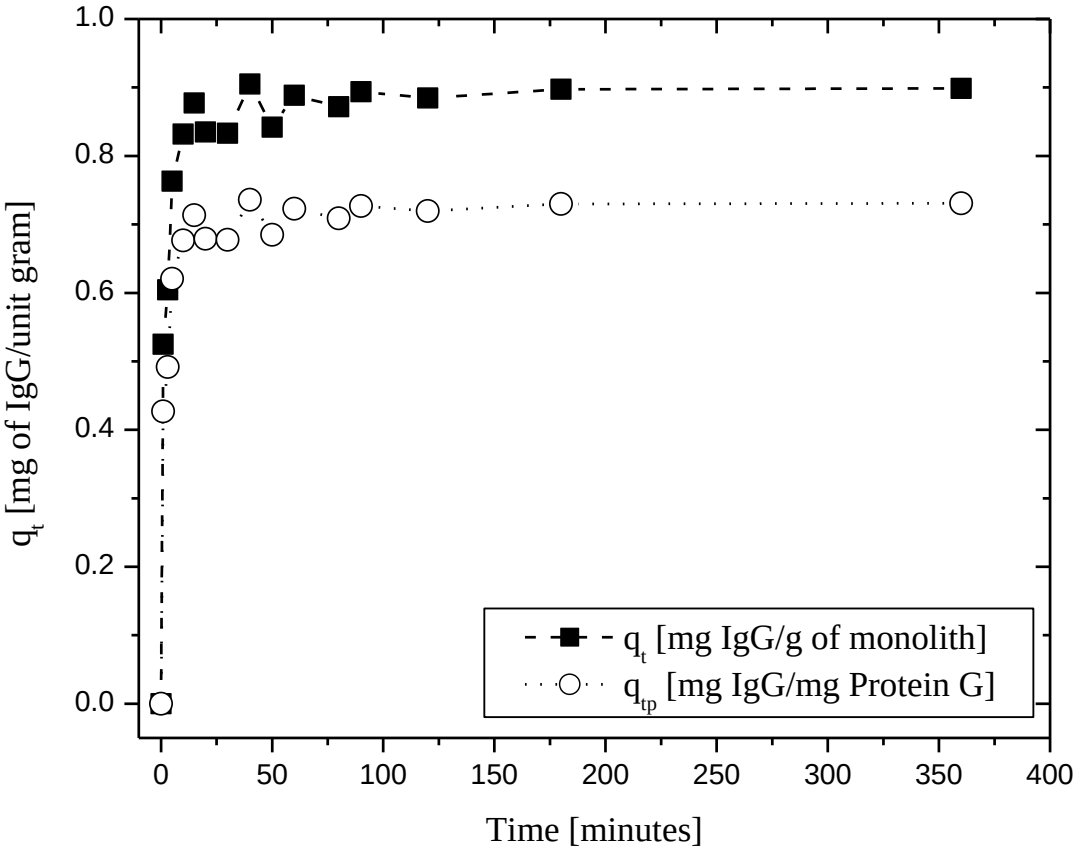

Figure 5.10. Study with Bovine Immunoglobulin G binding in a monolith functionalized with Protein G

Furthermore, a binding experiment was carried out to test the adsorption of bovine IgG onto this Protein G (Protein G concentration: 1 $mg.mL^{-1}$) - attached monolith as shown in Fig 5. 10. IgG at a concentration of 1 $mg.ml^{-1}$ in a 50 mM phosphate buffered saline (PBS, at pH = 7.4). It was found that about 0.89 mg of IgG adsorbed/ g of column (1.53 mg of IgG/cm^3 of monolith) i.e. the binding was 0.731 mg IgG/ mg of Protein G (73.5%). Subsequently, when eluted using a 25 mM citrate buffer (pH = 3.5) about 0.89 mg of IgG were recovered (86%) after 5 hours of elution.

As discussed in a previous work [26] based on these results it is clear that APTES suitably modified the column assuring a stable attachment via covalent bonds to the alumina and similarly stable attachment to BSA and Protein G. However, aggregation has a significant influence on the binding of the protein – further investigation on its influence on function and efficacy might yield better insights into the potential of the column. Furthermore, based on the studies with changes in pH (extreme pH), varying salt concentrations and temperature, it appears that the protein is interacting with the APTES via ionic interactions – this has also been suggested in previous

studies [31]. Finally, a basic experiment using IgG shows that such a column can effectively use for affinity-based purification of immunoglobulins.

5.4 Conclusions

Protein ligand attachment to a previously developed amine functionalized alumina monolithic column was studied in depth in this work, using BSA to anticipate the behavior of Protein G. The interaction between BSA and the amine functionalized column was studied in terms of attachment mechanism and stability. It was found that at lower concentrations there appears to be a strong and possibly reactive attachment of BSA to the column. However, as the concentration of BSA in solution is increased there is a trend of protein aggregation resulting in the appearance of multilayered attachment of the protein to the column – as indicated by fitting the data to the Freundlich isotherm. It was also observed that at lower BSA concentrations the binding followed a first order kinetic model, while at concentrations higher than 1 $mg.mL^{-1}$, the behavior switched to a second order kinetic model, showing an increased amount of binding to the column. Additionally, stability tests indicated that BSA was very stably bound to the column at all concentrations – there was a maximum of 10% (by weight) elution of the attached protein despite treatment with extreme pH and ionic strength elution solutions. The observation regarding aggregation at higher protein concentrations was corroborated by dynamic light scattering tests which show the presence of larger particles when using higher concentrations of BSA and effect of the recirculation through the monolithic column in promoting protein aggregation. These results are required for the design of an optimal process for attachment of the actual ligand (Protein G) at a best possible concentration avoiding wastage. It was found that up to 29% of Protein G could be successfully bound to the column (@solution concentration of 1.0 $mg.mL^{-1}$). A subsequent trial with IgG adsorption on this column revealed that about 73.4% IgG/Protein G was bound to the column and about 86% of this could be successfully eluted using an appropriate buffer. This result indicates that the column has a good potential to be used as an affinity chromatography column.

References

1. António L. Grilo, A. Mantalaris, The Increasingly Human and Profitable Monoclonal Antibody Market, Trends in Biotechnology, Volume 37, Issue 1, 2019, Pages 9-16.

2. R.R. Walters, Affinity chromatography, Anal. Chem. 57 (1985) 1099A-1114A.

3. J.E. Schiel, R. Mallik, S. Soman, K.S. Joseph, D.S. Hage, Applications of silica supports in affinity chromatography, J. Sep. Sci. 29 (2006) 719-737. [PubMed: 16830485]

4. P.O. Larsson, High-performance liquid affinity chromatography, Methods Enzymol. 104 (1984) 212-223. [PubMed: 6371445]

5. P.E. Gustavsson, P.O. Larsson, Handbook of Affinity Chromatography, 2nd Edition. D.S. Hage editor. Vol. Chap 2. Taylor & Francis; New York, 2006

6. P.E. Gustavsson, P.O. Larsson, Monolithic Materials. F. Svec, T.B. Tennikova, Z. Deyl editors. Elsevier; Amsterdam: 2003. p. 121-141.

7. K.K. Tetala, T.A. van Beek, Bioaffinity chromatography on monolithic supports, J. Sep. Sci. 33 (2010) 422-438. [PubMed: 20099259]

8. R. Mallik, D.S. Hage, Affinity monolith chromatography, J. Sep. Sci. 29 (2006) 1686–1704. [PubMed: 16970180]

9. M.J. Yoo, D.S. Hage, Monolithic Chromatography and Its Modern Applications. P.Wang, editor. Vol. Chap. 1. ILM; St. Albans: 2010.

10. E.L. Pfaunmiller, M.L. Paulemond, C.M. Dupper, D.S. Hage, Affinity monolith chromatography: a review of principles and recent analytical applications, Anal. Bioanal. Chem. 405 (2013) 2133-2145. [PubMed: 23187827]

11. M. Kubin, P. Spacek, R. Chromecek, Gel permeation chromatography on porous poly(ethylene glycol methacrylate), Collect. Czech. Chem. Commun. 32 (1967) 3881-3887.

12. T.R. Lynn, D.R. Rushneck, A.R.Cooper, High Resolution-Low Pressure Liquid Chromatography, J. Chromatogr. Sci. 12 (1974) 76-79.

13. F.D. Hileman, R.E. Sievers, G.G Hess, W.D. Ross, In situ preparation and evaluation of open pore polyurethane chromatographic columns, Anal. Chem. 45 (1973) 1126-1130.

14. W.D. Ross, R.T. Jefferson, In situ-formed open-pore polyurethane as chromatography supports, J. Chromatogr. Sci. 8 (1970) 386-389.

15. L.C. Hansen, R.E. Sievers, Highly permeable open-pore polyurethane columns

for liquid chromatography, J. Chromatogr. 99 (1974) 123-133.

16. D. Josic, J. Reusch, K. Loester, O. Baum, W. Reutter, High-performance membrane chromatography of serum and plasma membrane proteins, J. Chromatogr. 590 (1992) 59-76. [PubMed: 1601978]

17. M. Merhar, A. Podgornik, M. Barut, M. Zigon, A. Strancer, Methacrylate monoliths prepared from various hydrophobic and hydrophilic monomers–Structural and chromatographic characteristics, J. Sep. Sci. 26 (2003) 322-330.

18. T.B. Tennikova, B.G. Belenkii, F. Svec, High-performance membrane chromatography. A novel method of protein separation, J. Liq. Chromatogr. 13 (1990) 63-70.

19. T.B. Tennikova, F. Svec, High-performance membrane chromatography: highly efficient separation method for proteins in ion-exchange, hydrophobic interaction and reversed phase modes, J. Chromatogr. 646 (1993) 279-288.

20. S. Hjerten, J.L. Liao, R. Zhang, High-performance liquid chromatography on continuous polymer beds, J. Chromatogr. 473 (1989) 273-275.

21. F. Svec, J.M. Frechet, Continuous rods of macroporous polymer as high-performance liquid chromatography separation media, Anal. Chem. 64 (1992) 820-822.

22. T. Jiang, R. Mallik, D.S. Hage, Affinity Monoliths for Ultrafast Immunoextraction, Anal. Chem. 15 (2005) 2362-2372.

23. R. Mallik, T. Jiang, D.S. Hage, High-Performance Affinity Monolith Chromatography: Development and Evaluation of Human Serum Albumin Columns, Anal. Chem. 76 (2004) 7013-7022. [PubMed: 15571354]

24. E.L. Pfaunmiller, M. Hartmann, C.M. Dupper, S. Soman, D.S. Hage, Optimization of human serum albumin monoliths for chiral separations and high-performance affinity chromatography, J. Chromatogr. A. 126 (2012) 198-207.

25. N. Nayak, N. Vitorino, J. R. Frade, A. V. Kovalevsky, V. D. Alves, J. G. Crespo, C. A. M. Portugal, Design of alumina monoliths by emulsion-gel casting: Understanding the monolith structure from a rheological approach, Mater. Des. 157 (2018) 119-129.

26. N. Nayak, R. Huertas, J.G. Crespo, C.A.M. Portugal, Surface Modification of Alumina Monolithic Columns with 3-Aminopropyltetraethoxysilane (APTES) for Protein Attachment, Sep. Purif. Technol. (2019) 115674.

27. Thermo Fisher Scientific Pierce Protein, Protein Purification Technical Handbook, 2010. doi:http://dx.doi.org/10.1016/S1251-8050(99)80047-0.

28. Y.L. Jeyachandran, J.A. Mielczarski, E. Mielczarski, B. Rai, Efficiency of blocking of non-specific interaction of different proteins by BSA adsorbed on hydrophobic and hydrophilic surfaces, J. Colloid Interface Sci. 341 (2010) 136-142.

29. S. S. Blaszykowski C. Thompson M, Sacrificial BSA to block non-specific adsorption on organosilane adlayers in ultra-high frequency acoustic wave sensing. Surf. Interface Anal. 45 (2013) 1781–1784.

30. Riquelme. M.V., Zhao H. Srinivasaraghavan V. Pruden A., Vikesland P., Agah M, Optimizing blocking of nonspecific bacterial attachment to impedimetric biosensors. Sens. Bio-Sens. Res. 8 (2016) 47–54.

31. E.H. Williams, A.V. Davydov, A. Motayed, S.G. Sundaresan, P. Bocchini, L.J. Richter, G. Stan, K. Steffens, R. Zangmeister, J.A. Schreifels, M.V. Rao. Immobilization of streptavidin on 4H–SiC for biosensor development, Appl. Surf. Sci. 258 (2012) 6056-6063.

32. E. Karlsson, L. Ryden, J. Brewer, Ion exchange chromatography. In Protein Purification: Principles, High-Resolution Methods, and Application; Janson, J. C., Ryden L., Eds.; John Wiley & Sons: New York, 1998; pp145-205

33. Y.S. Ho, G. McKay, Pseudo-second order model for sorption processes, Process Biochem. 34 (1999) 451–465.

34. I. Langmuir, The constitution and fundamental properties of solids and liquids, J. Frank. Inst. 183 (1917) 102-105.

35. H. M. F. Freundlich, Over the adsorption in solution, J. Phys. Chem. 57 (1906) e470.

36. S.N. Taqui, R. Yahya, A. Hassan, N. Nayak, A.A. Syed, Development of sustainable dye adsorption system using nutraceutical industrial fennel seed spent-studies using Congo red dye, Int. J. Phytorem. 19 (2017) 686-694.

37. M.I. Tempkin, V. Pyzhev, Kinetics of ammonia synthesis on promoted iron catalyst. Acta Phys. Chem. URSS 12 (1940) 327-356.

CHAPTER 6

Conclusions

6.1. Outlook

In the present thesis, inorganic monolithic columns were developed using α - alumina as the base material. Emulsion-gel casting was used to produce mechanically stable and highly porous cellular structures with alumina suspension as the continuous phase and eco-friendly lipids as the dispersed phase, which could be a viable alternative to toxic and expensive dispersed phases, e.g. alkanes. It was demonstrated that the structural characteristics of the monoliths could be tuned by selecting suitable lipids (or lipid mixtures), making up the dispersed phase, since they dictate the behaviour of the emulsion-gel along aging (storage period). Changes in the oil droplet distribution along the emulsion storage (72 hours) show considerable effects on their rheological properties e.g., changes in the storage and loss moduli (G' and G") along storage provide important insights about droplet coalescence, flocculation and ripening occurring in the emulsion. Hence, these parameters may be used to understand changes in the emulsion structure with storage and their influence in the final microstructure of the sintered green bodies. The obtained results showed that most of the emulsions underwent a degree of coalescence and flocculation leading to formation of the droplet network and, during sintering, to the formation of multimodal hierarchical porous structures, with average pore sizes in the range of 0.2-3.2 μm and porosity in the range of 30 - 58% depending on the lipid(s) used. Emulsions prepared from pure corn and castor oils, or a mixture with equivalent weight proportions of these, led to monoliths with typical morphologies, i.e. high porosity and multimodal pores well interconnected. Contrastingly, emulsions with margarine led to monoliths with dense structures (low porosities and average pore sizes) and scattered large cavities (defects). Such structural effects may be counter-balanced by adding an oil component which may reduce the stability of the emulsion, such as corn oil. Corn oil was found to prompt intense droplet coalescence along aging, leading to monoliths with a more perceptible hierarchical porous structure, improved porosities and higher average pore sizes. The monoliths produced also show good mechanical properties with compressive strengths in the range of 8 - 50 $N.mm^{-2}$, with the weakest being the samples with castor oil and the strongest the ones with margarine. Furthermore, it was demonstrated that some rheological and morphological properties of the emulsion-gels (i.e. interfacial tension, droplet size, relaxation time and storage modulus) can be correlated with structural descriptors of the final monolith, i.e. the average pore size and porosity.

Subsequently, the potential of a computational fluid dynamics (CFD) modelling approach to simulate fluid behaviour in monolithic porous columns, such as those used in chromatography, was explored. The structure of the porous alumina monolithic column was reconstructed from 3D

scans obtained by non-invasive X-ray µ-tomography. Next, a computational fluid dynamics (CFD) study, which involved simulating the velocity and pressure fields of a fluid (water) flowing through the monolith was performed, followed by simulation of the path of a tracer pulse injection in a randomly selected volume section of the virtually reconstructed monolith. This approach enabled a detailed characterization of structural and hydrodynamic parameters such as streamlines (flow pathways), pore tortuosity and residence time distribution (RTD). The approach used here avoids the need for model-dependent fitting parameters, thus it is an important step towards optimization of processes in which monoliths (or other porous structures) are used.

Now that a prototype alumina monolith was ready, whose hydrodynamic properties were defined, the next step involved making the produced monolith suitable for practical applications. As alumina is an inherently inert material, it required functionalization for further development and application. A modified single step method to functionalize alumina monolithic columns was developed using a sol-gel synthesis with APTES as the silane agent. This method resulted in functionalized alumina monoliths with abundant NH_2 groups well distributed throughout the column. The sol-gel reaction conditions were optimized in terms of catalyst (pH), temperature, humidity, number of APTES coating layers and concentration of precursor (APTES). Basic pH (1M NaOH) was found to positively influence the functionalization process. The optimal conditions for column functionalization were found by using a full factorial experimental design approach combined with the experimental evidence for column etching in aqueous solution. The optimal functionalization conditions were set at 100% humidity and 1 coating layer of 2M APTES solution, which led to monoliths containing 166 µg of NH_2/g monolith.

As stated earlier, the theme of this work was to develop a material with potential to be an applied as an affinity chromatographic medium. In this context, it is important to understand how proteins interact with the developed column. Therefore, the interaction between BSA and the amine functionalized column was studied in terms of attachment mechanism and stability. It was found that at lower concentrations there appears to be a strong and possibly reactive attachment of BSA to the column. However, as the concentration of BSA in solution is increased there is a trend of protein aggregation resulting in the appearance of multi-layered attachment of the protein to the column – as indicated by fitting the data to the Freundlich isotherm. It was also observed that at lower BSA concentrations the binding followed a first order kinetic model, while at concentrations higher than 1 $mg.mL^{-1}$, the behaviour switched to a second order kinetic model, showing an increased amount of binding to the column. However, the stability tests indicated that the BSA was very stably bound to the column at all concentrations – there was a maximum of 10% (by

weight) elution of the attached protein despite treatment with extreme pH and ionic strength. The observation regarding aggregation at higher protein concentrations was corroborated by the dynamic light scattering tests which show the presence of larger particles when using higher concentrations of BSA and effect of the recirculation through the monolithic column in promoting protein aggregation. These results help develop an optimal process for attachment of actual ligand (Protein G) at best possible concentration to avoid wastage. It was found that up to 29% of Protein G could be successfully be bound to the column (@solution concentration of 1.0 mg.mL-1). Subsequent trial with IgG adsorption on this column revealed that about 73.4% IgG/Protein G was bound to the column and about 86% of this could be successfully eluted using an appropriate buffer. This indicates that the column has great potential to be used as an affinity chromatography column.

6.2. Future Work

In this thesis the discussion is primarily focussed on the development of the material which could potentially act as an affinity chromatography medium. The investigation was a deep-dive into the parameters involved in the formation of the monolith, its functionalization - including optimization, and a case study of the application with model proteins (BSA, Protein A/G, Immunoglobulins) – though columns with these proteins are applied in mainstream monoclonal antibody purification. Additionally, applying computational fluid dynamics, the hydrodynamic parameters of the system were also elucidated. Although, this work contributes to the substantial potential of the field of materials science, chemical engineering and more specifically towards chromatography, there are yet unlimited possibilities to apply this system for enhancement of different processes – ranging from heterogeneous catalysis to filtration.

From the materials perspective, considering the fact that Additive Manufacturing (AM) is taking over the world with people producing everything from trinkets to large scale equipment using 3D printing, it is not difficult to imagine that materials used for scientific applications will be produced by 3D-printing. From this viewpoint, the correlations established in this thesis explore the possibility of anticipating the final microstructural features of the monolith based on easily measurable emulsion-gel properties of rheology. The design of monoliths with fine-tuned morphologies is important as it could lead to the production of porous media for varied applications, including chromatography and membrane-based separations. Furthermore, applying the principles of CFD developed herein, several works have proven that it is feasible to produce precisely controlled porous media with minimal apothem of 115 μm. In addition, the ".stl"

(stereolithography) files used to give information about geometry, shape and dimensions of a 3D printed object are the same type of files used in this work to create computational mesh and perform CFD studies. Consequently, the CFD modelling approach presented herein can be directly used to optimize and virtually test the performance of chromatographic materials before being even printed/manufactured, thus leading to production of materials “right at the first time” and according to the “design-for-purpose” approach. It is noteworthy that as the pores in the emulsion-gel method are generated by burning out of oil droplets, lower resolution printers could potentially be applied to create complex structures.

In keeping with the theme of the thesis, which was to develop materials specifically for affinity chromatography, a study on modification of the alumina materials was carried out using silanization. However, given the time and resources, there are methods like physical modification using sputtering or other chemical methods like epoxy coatings, Grignard reagents or even other silanes, which could provide the monolith with different functionalities that could be explored.

Furthering this theme, alternate applications could be developed using the prepared monolith as a base with differently modified pore surfaces to explore catalytic reactions, ion exchange interactions and possibly electrochemical processes as well.

From the perspective of protein separations, in the present thesis the work was limited to a model and well-known protein system – that of Protein A/G, BSA, IgG – to prove the possibility of using the monolith as an affinity stationary phase for separation purposes. Further study into the interaction of these proteins with the column is recommended to understand better the binding between the protein and the column, in terms of the binding energy by using NMR, FTIR and DSC-TGA. Although the base monolith itself is quite economical to produce, the most expensive part of the system is the protein. Synthetically produced mimetic ligands incorporating only the specific binding domains of Protein A/G are already known to be used in affinity chromatography columns and membrane chromatography for the purification of antibodies although, there are almost no reports of them being applied in monolithic columns. Therefore, additional studies with such ligands could improve the process efficiency in terms of higher ligand density and effectiveness and could therefore be applied to produce cheaper and scalable monoliths for this purpose.

Finally, from a much broader social perspective, owing to the simplicity of the emulsion gel casting method and its versatility in terms of materials that it can be applied to, smaller pottery kilns in remote areas could potentially produce advanced materials for applications in economically

backward areas. For example, filtration membranes or columns could be prepared using materials like kaolin clay and cooking oil. This material could have pore sizes in the range of 2 microns, but due to the tortuous nature of the pores, it could act as a sufficiently effective filter to help make potable water in areas where it is difficult to obtain clean water – thus contributing towards societal improvements.

APPENDIX A

Appendix

A1. Design of alumina monoliths by emulsion-gel casting: understanding the monolith structure from a rheological approach

Table A1.1. Rheological properties of the emulsions used to produce the cellular alumina structures

Legend: 'N' is a dimensionless constant related to the power law index (N = (1-n)/2) obtained by fitting the simplified Carreau model to viscosity vs. shear rate profiles. η_0 is the apparent viscosity at zero shear rate (1st Newtonian plateau viscosity) all obtained from the apparent viscosity measurements, tan δ is the tangent of loss angle, G_N^0 is the plateau modulus obtained from the viscoelastic tests.

Dispersed phase	N	n	η_0 [Pa.s]	tan δ	G_N^0 [Pa]
0 hours					
Corn oil	0.55	0.225	963900	0.073	3499.00
Castor oil	0.47	0.265	127100	0.134	1585.00
Margarine	0.38	0.31	18120	0.552	814.40
Corn oil + Castor oil (1:1)	0.62	0.19	236400	0.120	3406.00
Margarine + Corn oil (1:3)	0.58	0.21	30490	0.171	786.60
Margarine + Corn oil (3:1)	0.40	0.3	5030	0.498	163.60
Marg. + Corn oil + Castor oil (1:1:1)	0.23	0.385	3227	0.250	326.00
72 hours					
Corn oil	0.44	0.28	45620	0.182	1745.00
Castor oil	0.59	0.205	47360	1.070	1425.00
Margarine	0.40	0.3	10390	2.052	5.31
Corn oil + Castor oil (1:1)	0.51	0.245	56100	0.232	2506.00
Margarine + Corn oil (1:3)	0.54	0.23	11900	0.289	467.50
Margarine + Corn oil (3:1)	0.39	0.305	10040	0.483	394.70
Marg. + Corn oil + Castor oil (1:1:1)	0.38	0.31	6604	0.335	448.30

Viscosity vs. Shear rate profiles for emulsions made from single lipids (i.e. corn oil, castor oil and margarine) and lipid mixtures were fit to the simplified Carreau model (Equation 1). The model was fit using the Levenberg-marqhardt algorithm using SOLVER tool from Microsoft Excel.

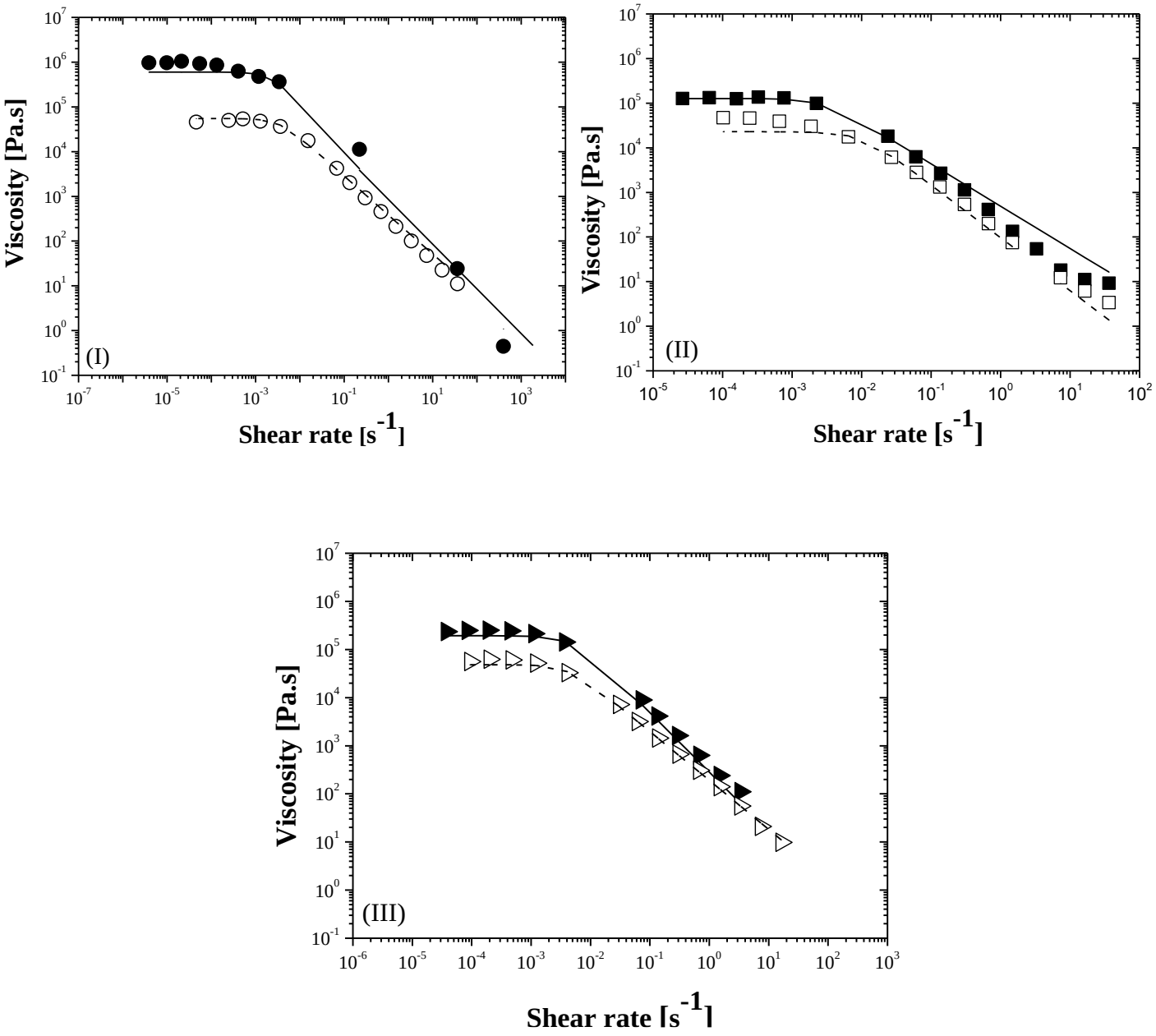

Figure A1.1. Viscosity vs. shear rate profiles for emulsions made with oils

Legend: emulsions are made with I) Corn oil [●,○], II) Castor oil [■,□] and III) Corn oil + Castor oil (1:1) [▶,▷] fit to the simplified Carreau model (dashed lines). Filled and empty symbols stand for emulsions at 0h and 72h storage, respectively.

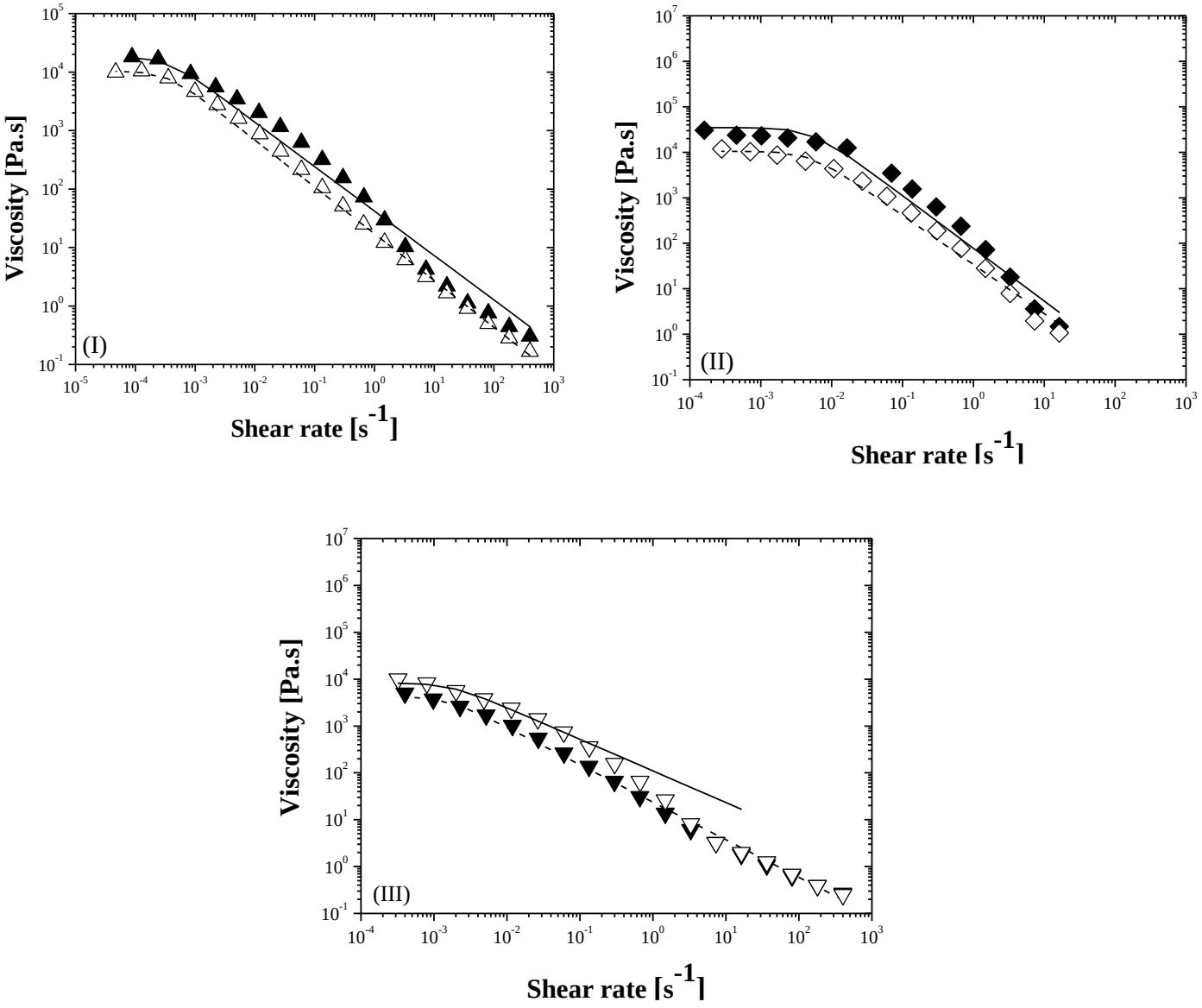

Figure A1.2. Viscosity vs. shear rate profiles for emulsions made with oils

Legend: Emulsions made with I) Margarine [▲,△] II) Margarine + Corn oil (1:3) [◆,◇] and III) Margarine + Corn oil (3:1) [▼,▽] fit to the simplified Carreau model (dashed lines). Filled and empty symbols stand for emulsions at 0h and 72h storage, respectively.

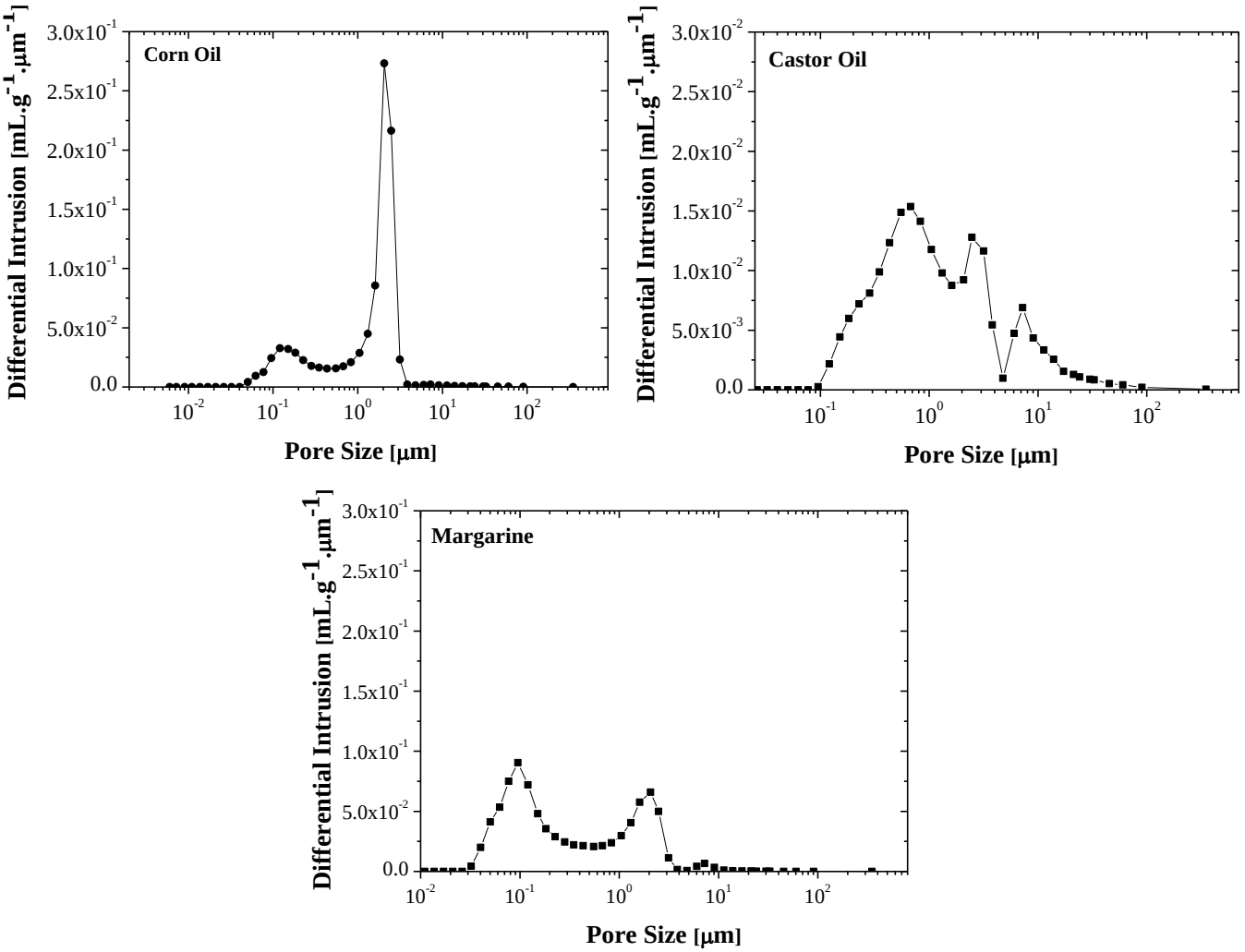

Figure A1.3. Distribution pore size profiles obtained by mercury intrusion porosimetry for monoliths obtained from emulsions prepared with pure A) corn oil, B) castor oil and C) margarine.

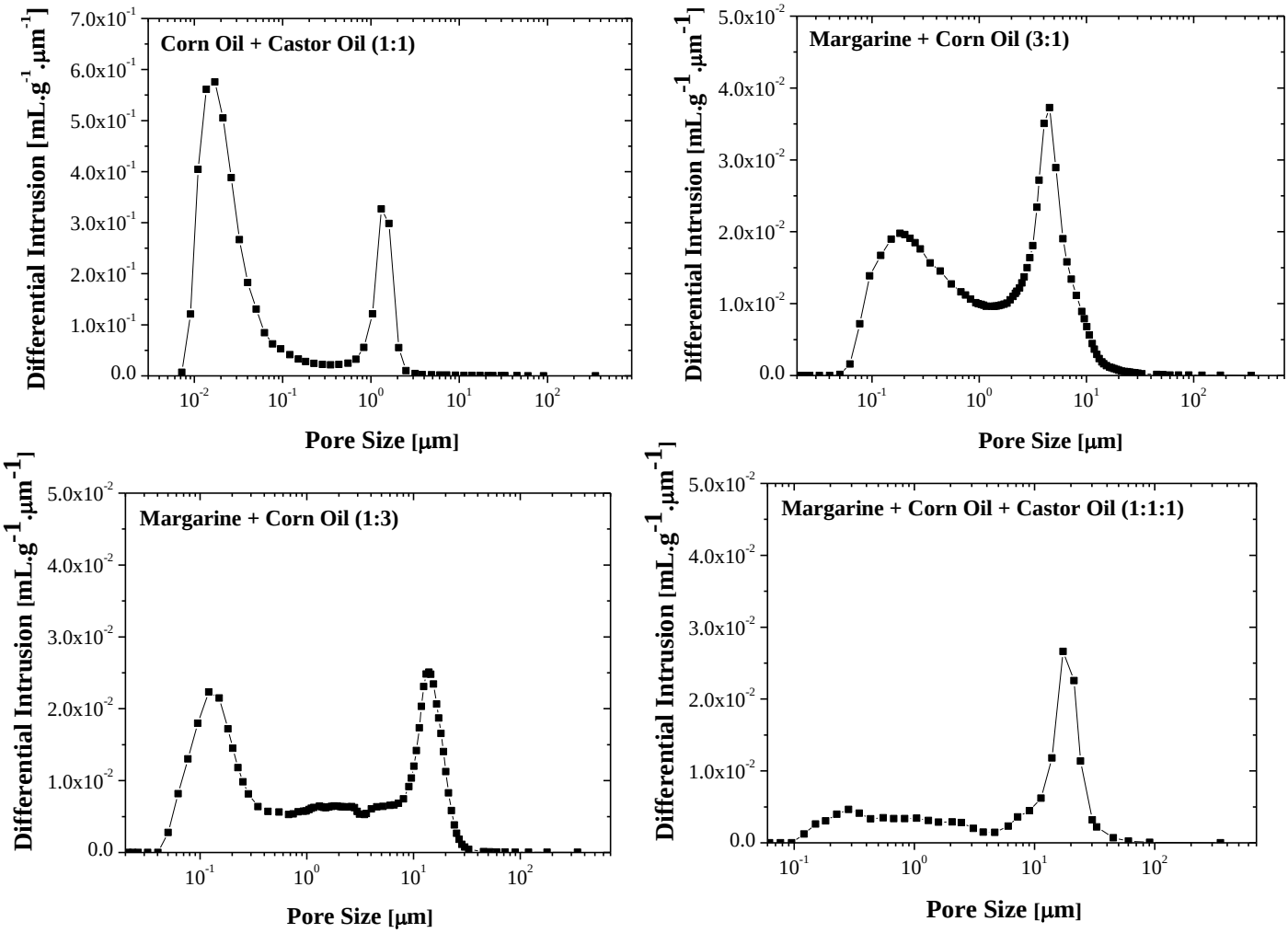

Figure A1.4. Distribution pore size profiles obtained by mercury intrusion porosimetry for monoliths obtained from emulsions prepared with corn oil + castor oil (1:1), margarine + corn oil (1:3), margarine + corn oil (3:1), and margarine + corn oil + castor oil (1:1:1).

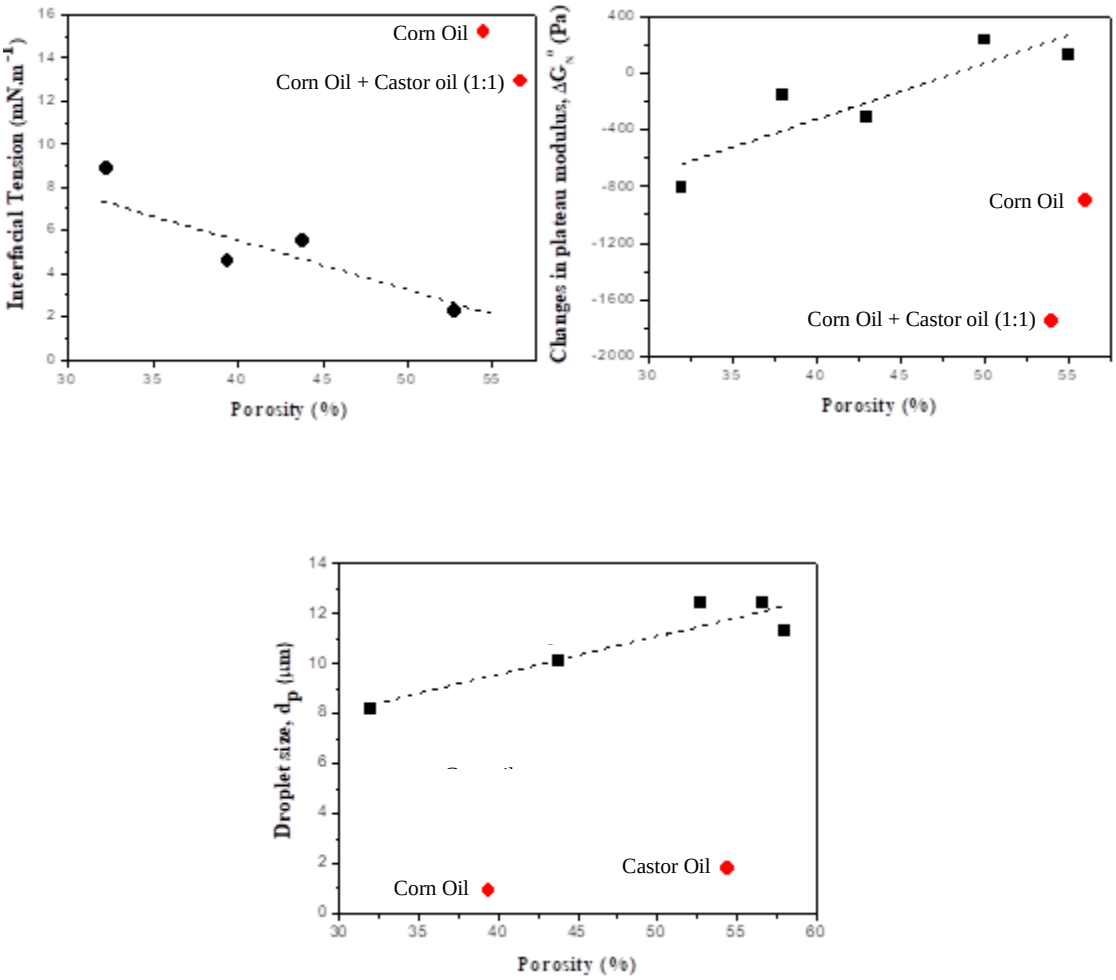

Figure A1.5. Correlation of the morphological and rheological properties of the emulsions I) interfacial tension, II) changes in plateau modulus (ΔG_N^0) along storing and III) droplet size (d_p) with the porosity of the monoliths.

A2. CFD modelling of flow patterns, tortuosity and residence time distribution in monolithic porous columns reconstructed from X-ray tomography data

Preparation of the alumina monolith column

An alumina (Alcoa chimie, CT-3000) suspension was prepared with 50% (by volume) of water and added deflocculant (10% Dolapix). This suspension was used as the continuous phase to prepare an emulsion with corn oil with a fixed phase ratio of oil: water of 3:2. An emulsifier (Sodium dodecyl sulfate, Sigma Aldrich) was added to stabilize the emulsion and additionally, a gelling agent (collagen – Gelatin Oxoid - LP0008) was added to solidify the column. This emulsion was poured into column-shaped molds. Once sufficiently solidified, the columns were taken out of the mold and sintered with an appropriate temperature cycle up to 1550 °C.

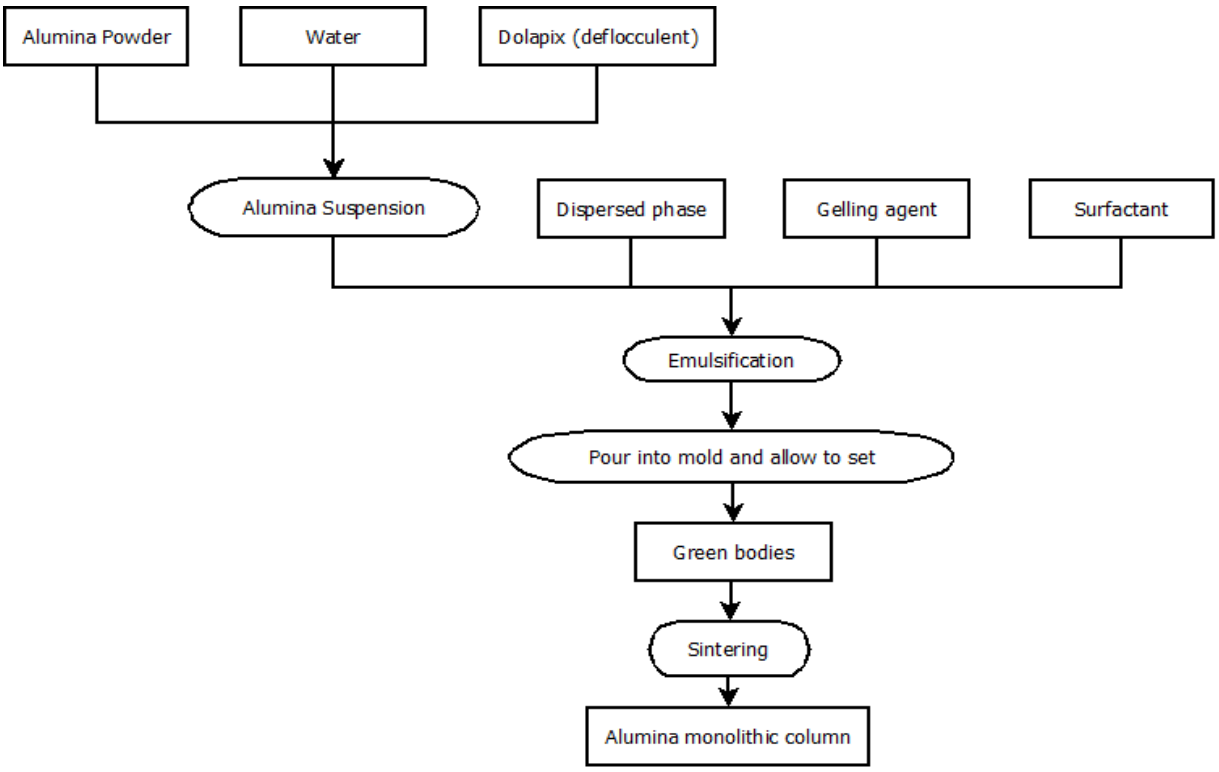

Figure A2.1. Flow chart of the steps followed to prepare alumina monolithic column

Computational fluid dynamics (CFD) results for sub-volume B

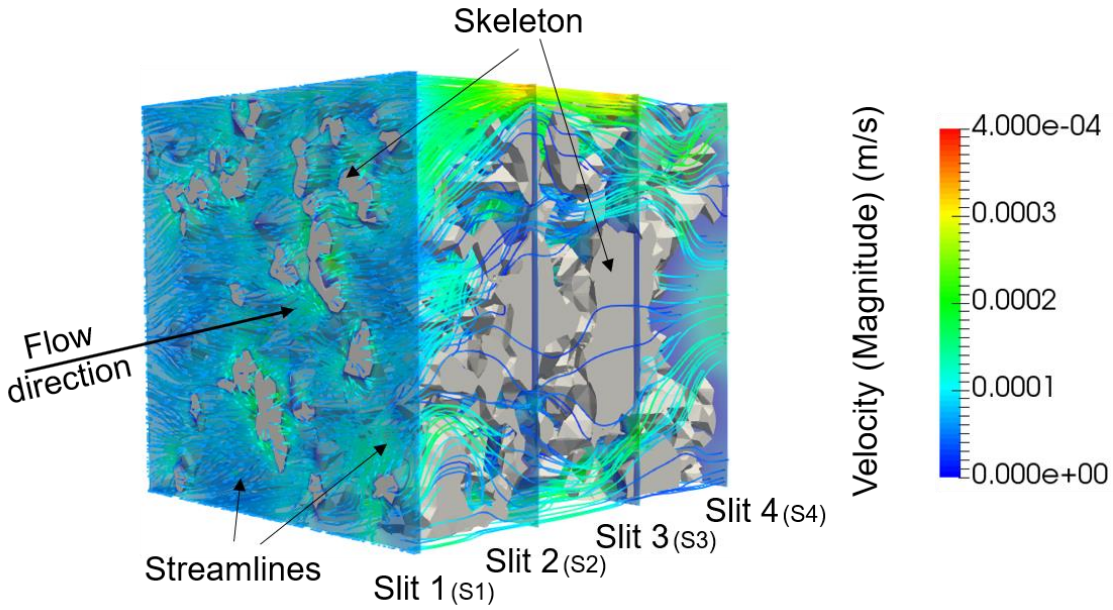

Figure A2.2. Representation of streamlines (fluid pathways) in sub-volume B of the 3D virtually reconstructed monolith

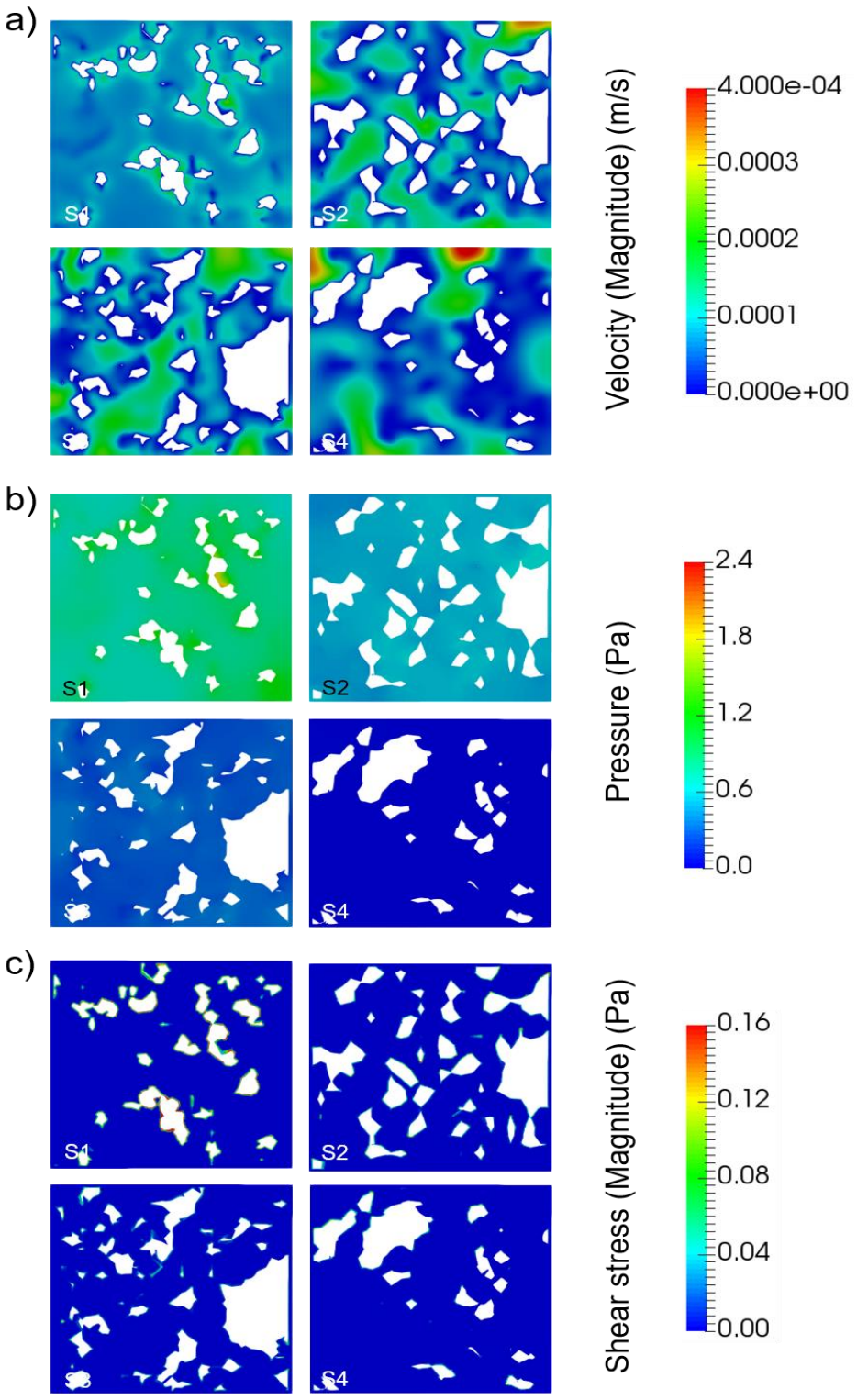

Figure A2.3. CFD results obtained in sub-volume B, showing slits S1, S2, S3 and S4 with information about computed a) velocity, b) pressure and c) shear stress

Legend: The white regions are the skeleton.

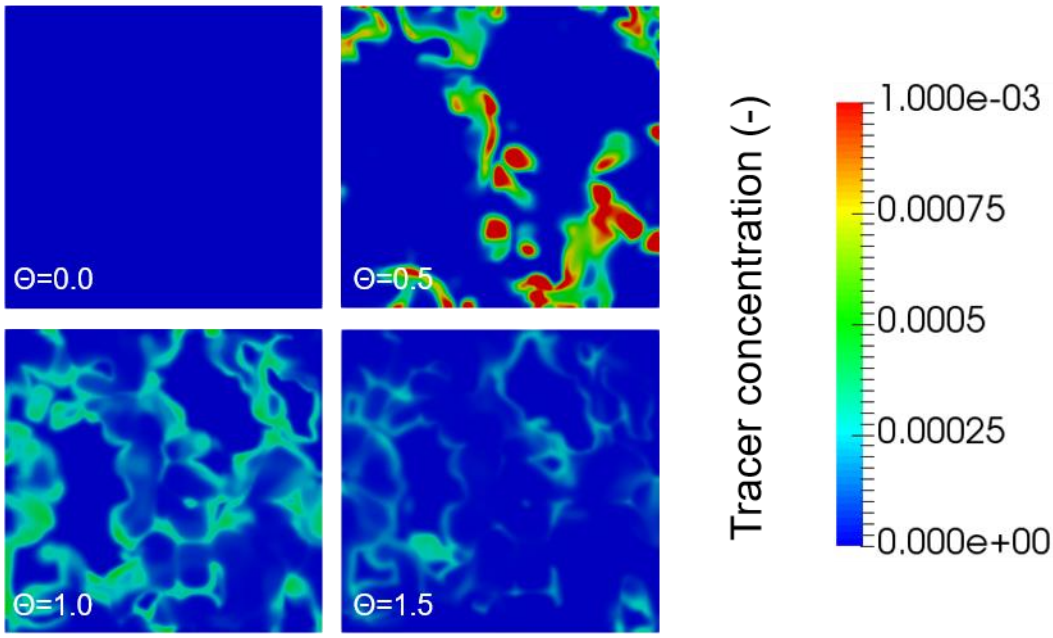

Figure A2.4. Local dimensionless tracer concentration at the outlet of sub-volume B along time (normalized by mean time residence)

A3. Experimental design (full factorial) to optimize the reaction parameters affecting silanization

Table A3.1. Full factorial experimental design for determination of effect of precursor concentration (APTES concentration), relative humidity and number of coatings on the overall quantity of primary amine groups present in the monolithic column

Run order	APTES Concentration [M]	Relative Humidity [%]	Number of Coatings
1	1.5	0	1
2	1.5	0	3
3	1.5	0	5
4	1.5	65	1
5	1.5	65	3
6	1.5	65	5
7	1.5	100	1
8	1.5	100	3
9	1.5	100	5
10	2	0	1
11	2	0	3
12	2	0	5
13	2	65	1
14	2	65	3
15	2	65	5
16	2	100	1

17	2	100	3
18	2	100	5
19	3	0	1
20	3	0	3
21	3	0	5
22	3	65	1
23	3	65	3
24	3	65	5
25	3	100	1
26	3	100	3
27	3	100	5

A4. Solid state NMR experimental results on samples with silanized alumina

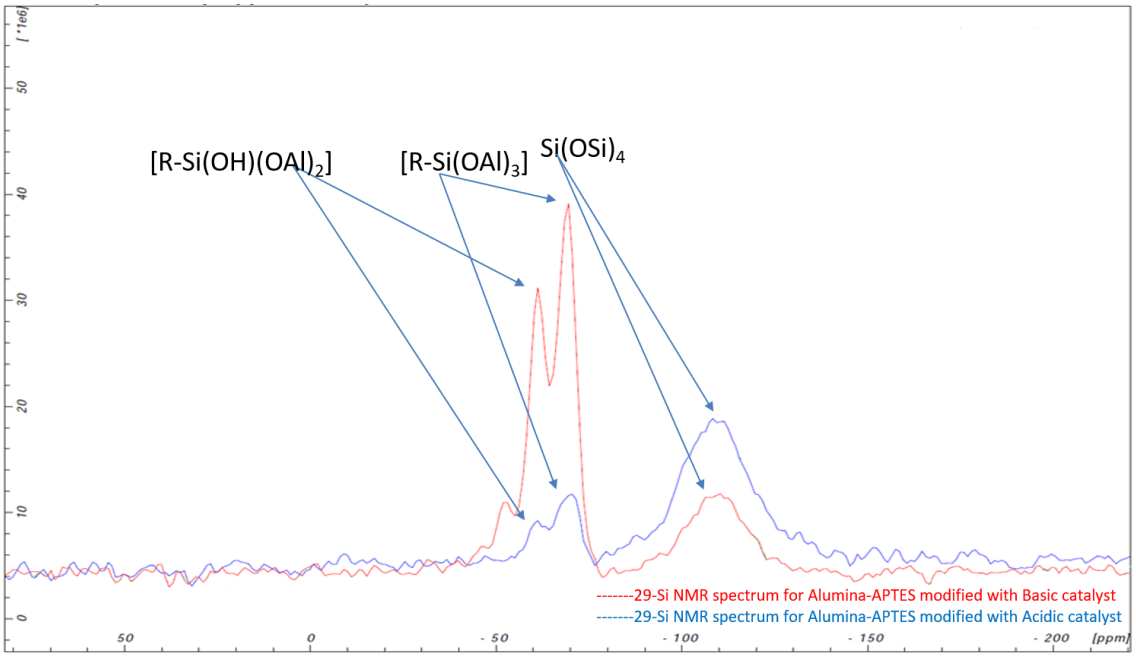

Figure A4.1. NMR spectra for characterization of APTES-coated Alumina sample indicating peaks for silanol groups and possible attachment of silane to alumina

The NMR spectra shown in Figure A4.1. further corroborates the fact that the alumina and silanol groups are indeed bonded attached by a covalent bond. As can be seen in the figure, there are three signals at −53, −61, and −71 ppm, which correspond to three other silicon environments in the functionalized monolayers of [R-Si(OH)$_2$(OAl)], [R-Si(OH)(OAl)$_2$], and R-Si(OAl)$_3$], respectively [ref]. These clearly indicate the presence of silanol-Al covalent bonds, and hence confirmation that highly stable coating has been formed on the alumina surfaces.